

UNIVERSITY OF CALIFORNIA, SAN DIEGO  
Department of Applied Mechanics and Engineering Sciences  
La Jolla, California 92093

---

A MAJOR STUDY OF CONCRETE MASONRY UNDER  
SEISMIC-TYPE LOADING

by

G. A. Hegemier, S. K. Arya, R. O. Nunn, M. E. Miller,  
A. Anvar, G. Krishnamoorthy



January 1978

Report No. UCSD/AMES/TR-77/002

Prepared for the  
NATIONAL SCIENCE FOUNDATION  
Grant NSF ENV 74-14818

For sale by the National Technical Information Service,  
U. S. Department of Commerce, Springfield Virginia, 22161.

A MAJOR STUDY OF CONCRETE MASONRY UNDER  
SEISMIC-TYPE LOADING<sup>1</sup>

by

G. A. Hegemier<sup>2</sup>, S. K. Arya<sup>2</sup>, R. O. Nunn<sup>2</sup>, M. E. Miller<sup>2</sup>,  
A. Anvar<sup>2</sup>, G. Krishnamoorthy<sup>3</sup>

ABSTRACT

This report constitutes an introduction to and a survey of an extensive University of California, San Diego research program on concrete masonry and the seismic response of concrete masonry structures. Objectives, scope, methodology, and utilization are discussed. Selected experimental, analytical, and numerical results are presented.

---

<sup>1</sup> Research was sponsored by the National Science Foundation under Grant NSF ENV 74-14818

<sup>2</sup> Professor, Principal Development Engineer, Graduate Student, Associate Development Engineer, Graduate Student, respectively, Dept. Appl. Mech. & Engr. Sci., Univ. of Calif., San Diego, La Jolla, 92093.

<sup>3</sup> Professor, Dept. of Civil Engr., San Diego State Univ., San Diego, Calif., 92182.

## TABLE OF CONTENTS

		Page
	LIST OF TABLES.....	v
	LIST OF FIGURES.....	vi
1.	INTRODUCTION.....	1
2.	ITEMS UNDER STUDY.....	3
3.	MATERIALS AND FABRICATION.....	4
4.	METHODOLOGY.....	5
5.	UTILIZATION.....	8
6.	DESCRIPTION OF SMALL-SCALE TESTS.....	10
7.	DESCRIPTION OF STATIC AND DYNAMIC PANEL (MACROELEMENT) TESTS.....	12
	7.1 Homogeneous Stress-States.....	12
	7.2 Nonhomogeneous Stress-States.....	19
8.	SELECTED RESULTS - PANELS (MACROELEMENTS) UNDER HOMOGENEOUS STRESS-STATES.....	25
	8.1 Initial Macrocracking Surface.....	25
	8.2 Macrocracking or Failure and Isotropy.....	35
	8.3 Prediction of Initial Macrocracking from Component Data.....	35
	8.4 Influence of Reinforcing Steel on Initial and Post Macrocracking Behavior.....	41
	8.5 Elastic Moduli and Anisotropy.....	47
	8.6 Elastic Moduli and Compressive Strength.....	47
	8.7 Damping and Strain-Rate Effects.....	49

TABLE OF CONTENTS (continued)

	Page
8.8 Influence of Flaws, Compaction, Admixtures.....	53
8.9 Finite Element Predictions (Micromodeling).....	61
9. SELECTED RESULTS - PANELS (MACROELEMENTS) UNDER NONHOMOGENEOUS STRESS-STATES.....	65
9.1 Diagonal Compression.....	65
9.2 Simple Shear Deformations.....	69
9.2.1 Micromodel.....	70
9.2.2 Macromodel.....	78
10. SELECTED RESULTS - SMALL SCALE TESTS.....	79
10.1 Prism Tests.....	79
10.2 Joint Behavior.....	84
11. REMARKS ON ADDITIONAL STUDIES.....	96
12. CLOSURE.....	106
ACKNOWLEDGEMENT.....	108
REFERENCES.....	109

## LIST OF TABLES

Table		Page
1.	Component Properties for Macroelements and prisms.....	28
2.	Tensile Strength Predictions.....	37
3.	Comparison of Reinforced and Unreinforced Panel Homogeneous Failure Stress (psi) $\sigma'_{11} = 0$ .....	43
4.	Ratio of Elastic Modulus to $f'_m$ .....	49
5.	Component Properties for Admixture Tests.....	58
6.	Tensile Failure Strength for Unreinforced Grouted Panels.....	62
7.	Compressive Strength for 4-Course Grouted Prisms.....	62
8.	Diagonal Compression Test Peak Loads (kips).....	68
9.	Shear Wall Prism Data.....	68
10.	Shear Wall Component Data (psi).....	68
11.	Component Properties for Full-Block Prism Tests.....	82
12.	Comparison of Correction Factors for Prism Shape after "Code Factor" Modification.....	83
13.	Connection Test Matrix.....	104

## LIST OF FIGURES

Figure		Page
1 (a)	Methodology of Research Program.....	6
1 (b)	Evolution of Research Program.....	7
2	Stress Transformation.....	13
3	Loading Schematic.....	15
4	Biaxial Fixture.....	16
5	Biaxial Test Frame.....	17
6	Data Acquisition.....	18
7	Diagonal Compression Test.....	20
8	Principal Stress Distribution on the Planes $x_2 = 0$ and $x_1 = 0$ .....	22
9 (a)	Biaxial Frame Modified for Shear Test.....	23
9 (b)	Schematic of the Berkeley Shear Wall Test.....	24
10	Failure Envelope for Zero Head-Joint Normal Stress.....	27
11 (a)	Typical Joint Failure.....	30
11 (b)	Multi-Crack Failure.....	31
12	Biaxial Strength of Concrete.....	32
13	Initial Macrocracking Envelope.....	33
14	Dependence of Panel Tensile Strength on Compressive Stress.....	34
15	Panel Tensile Strength Anisotropy.....	36
16	Grout Flaws at Bed-Joint Plane.....	39
17	Tensile Failure Pattern for $90^\circ$ Layup.....	40

LIST OF FIGURES (continued)

Figure		Page
18	Fixture Details for Reinforced Specimens.....	42
19	0° Unreinforced.....	45
20	0° Reinforced.....	45
21	20° Unreinforced.....	45
22	20° Reinforced.....	45
23	0° Reinforced Stress-Strain Curves.....	46
24	20° Reinforced Stress-Strain Curves.....	46
25	Panel Stiffness Anisotropy.....	48
26	Panel Poisson's Ratio Anisotropy.....	48
27	Typical Panel Compressive Cyclic Data.....	50
28 (a)	Typical Grout-Block Separation.....	54
28 (b)	Grout-Block and Mortar-Block Separation (Oblique Cut).....	55
28 (c)	Grout Bridges and Resulting Failure.....	56
28 (d)	Block-Grout Separation.....	57
28 (e)	Face-Shell Spallation.....	57
29 (a)	Sides of Panels: Puddled; Admixture Puddled; Vibrated; Admixture Vibrated (shown in order from top to bottom).....	59
29 (b)	Tops of Panels: Puddled; Admixture Puddled; Vibrated; Admixture Vibrated (shown in order from top to bottom).....	60
30 (a)	Finite Element Prediction of Failure.....	63
30 (b)	Typical Failure of an Unreinforced Panel.....	64

LIST OF FIGURES (continued)

Figure		Page
31	Typical Diagonal Compression Failure.....	66
32	Shear Wall Finite Element Discretization.....	73
33	Reinforced Shear Wall under Monotonic Loading..	74
34	Unreinforced Shear Wall under Monotonic Loading.....	75
35	Macrocracks in Reinforced Shear Wall under Monotonic Loading.....	76
36	X-Macrocracks in Reinforced Shear Wall under Cyclic Loading.....	76
37	Reinforced Shear Wall under Cyclic Loading.....	77
38	Failure Envelopes for Reinforced Shear Wall under Cyclic Loading.....	77
39	Correlation of Prism Strength and Geometry.....	81
40	Comparison of UngROUTED Wall and Couplet Strengths.....	85
41 (a)	Joint-Test Specimen.....	86
41 (b)	UCSD Cyclic Joint-Test Fixture.....	87
41 (c)	UCSD Joint-Test Setup.....	88
41 (d)	UCSD Cyclic Joint-Test Fixture and Specimen....	89
42	Behavior of Bed Joints under Precompression....	90
43	Strain-Rate Dependence.....	91
44	Joint under Cyclic Loading.....	92
45	Dependence of Joint Maximum Shear Stress on Normal Stress.....	93
46	Finite Element Simulation of Joint Behavior.....	95

LIST OF FIGURES (continued)

Figure		Page
47	Function of Connections in Shear Wall Structure..	97
48	Connection Detail of Precast Floor Slab and Interior Wall, Detail 1.....	98
49	Connection Detail of Precast Floor Slab and Interior Wall, Detail 2.....	99
50	Connection Detail of Cast-in-Place Floor Slab and Interior Wall, Detail 3.....	101
51	Connection Detail of Prestressed Concrete Planks and Interior Wall, Detail 4.....	102
52	Connection Test Setup.....	103



## 1. INTRODUCTION

Examination of recent surveys<sup>(1,2)</sup> relevant to the mechanics of concrete masonry systems reveals that, although a measurable amount of research on concrete masonry has been conducted over the past forty to fifty years, there has been little correlation among the various studies conducted by governmental, university, and promotional research organizations. Each study has, of economic necessity and/or impatience, been constrained within narrow bounds and primarily to specific structural configurations rather than to fundamental material research. In addition, most studies have not been sustained for a time interval sufficient to generate results of wide utility and integrity. As a consequence, a virtual vacuum exists concerning the material properties of concrete masonry, and the behavior of typical connections used in concrete masonry structures.

In the absence of reliable data, subjective judgement must be substituted for rational design and analysis. The ramifications of such a substitution are obvious and clearly undesirable from the standpoint of all parties involved - the public, the masonry industry, and the structural engineering community.

In response to the need for fundamental information, an extensive experimental, analytical, and numerical research program was initiated at the San Diego campus of the University of California. The objective of this program is the development of a basis for a rational earthquake response and damage analysis of concrete masonry structures. The study is sponsored by the National Science Foundation under project RANN (Research Appplied to National Needs). Contributions have also been received from the masonry industry.

It is noted that a companion program, covering a number of masonry materials in addition to concrete masonry, exists at the Berkeley

campus of the University of California. A valuable interchange of information between these programs has been effected, as will become evident later.

With respect to the San Diego program, the experimental effort is intended to define material behavior, and the behavior of typical connections used in concrete masonry structures. The analytical phase involves the translation of observed experimental data into viable mathematical models. The numerical effort concerns the conversion of mathematical models into numerical form and the construction of digital computer programs to simulate structural response and damage accumulation resulting from earthquake ground motion.

The approach selected to achieve the project objectives involves a sequence of increasingly complex levels of concurrent experimentation, analysis, and numerical simulation. This sequence begins with elementary experiments on the basic constituents of concrete masonry and their interactions, e. g., by fracture and slip across interfaces. It proceeds to homogeneous and nonhomogeneous biaxial tests of full-scale panels under both monotonic and cyclic load histories. The above is complemented by tests on typical connections. The sequence culminates with case studies of major structural elements and/or buildings. The ability to extrapolate from conceptually simple laboratory-scale experiments to a wide variety of structural configurations, including simulation of full-scale building response to earthquake ground motion, is one of the most significant aspects of the project.

In what follows, selected portions of the material properties segment of the aforementioned program are presented and discussed. Comprehensive and detailed discussion of all phases of the program can be found in the reports listed herein.

## 2. ITEMS UNDER STUDY

The basic experimental items under study concern planar material behavior and are related to the formulation of constitutive relations for concrete masonry in both linear and nonlinear ranges of deformation.

Included are:

- . Strength and damage accumulation under combined plane-stress states
- . Stiffness parameters
- . Energy absorption and damping

In each of the above areas, studies will determine the influence of:

- . Anisotropy
- . Strain-rate
- . Reinforcing steel volume and configuration
- . Grout compaction
- . Grout admixtures
- . Flaws
- . Constituent properties on assembly properties
- . Scale effects
- . Cyclic load histories

### 3. MATERIALS AND FABRICATION

Two nominal masonry types are currently under study: 1) "normal strength" - type N normal weight hollow core concrete block (ASTM C90), type S mortar (ASTM C270), 2000 psi coarse (pump mix, 8-10 inch slump) grout (ASTM C476); 2) "high strength" - light weight hollow core concrete block ( $f'_c \geq 3750$  psi), type M mortar (ASTM C270), 3750 psi coarse (pump mix, 8-10 inch slump) grout (ASTM C476). Precise details concerning constituent properties are provided in conjunction with discussions of each test series.

Most specimens consist of fully grouted masonry (8-foot lifts on full-scale specimens) with running bond and face-shell thickness mortar bedding. Both closed and open-end units are utilized, although focus is currently on the former. Standard 8-inch high, 8-inch wide block geometries<sup>(1)</sup> are used.

It is emphasized that all specimen fabrication is conducted by professional masons using conventional field practice. In particular, no effort has been made to achieve optimum "laboratory" conditions. All specimens are field cured.

#### 4. METHODOLOGY

The program partitions naturally into two main categories:

1) small-scale or microelement tests and micromodeling involving specimens of several unit (block) dimensions, and 2) large-scale or macroelement tests and macromodeling involving specimens of sufficient size to mirror full-scale masonry; the planar dimensions of the latter are approximately one order of magnitude larger than the largest micro-dimension (block size).

The objective of the small-scale tests and the associated micromodeling is to synthesize the behavior of masonry assemblies or macroelements from simple but universal experiments - experiments that can be conducted in a standard laboratory.

The large-scale or macroelement tests constitute a necessary check on the micromodeling process and, perhaps more important, constitute the starting point for the construction of a continuum or macro-model of concrete masonry. The latter, it is anticipated, may be used to efficiently synthesize the behavior of complex structures, in combination with appropriate connection data<sup>(3)</sup>, through the use of explicit analytical and numerical techniques. The numerical method in use is the finite element method (designated as FEM in Fig. 1 (a)). The overall methodology and evolution of the program is depicted in Figs. 1 (a, b).

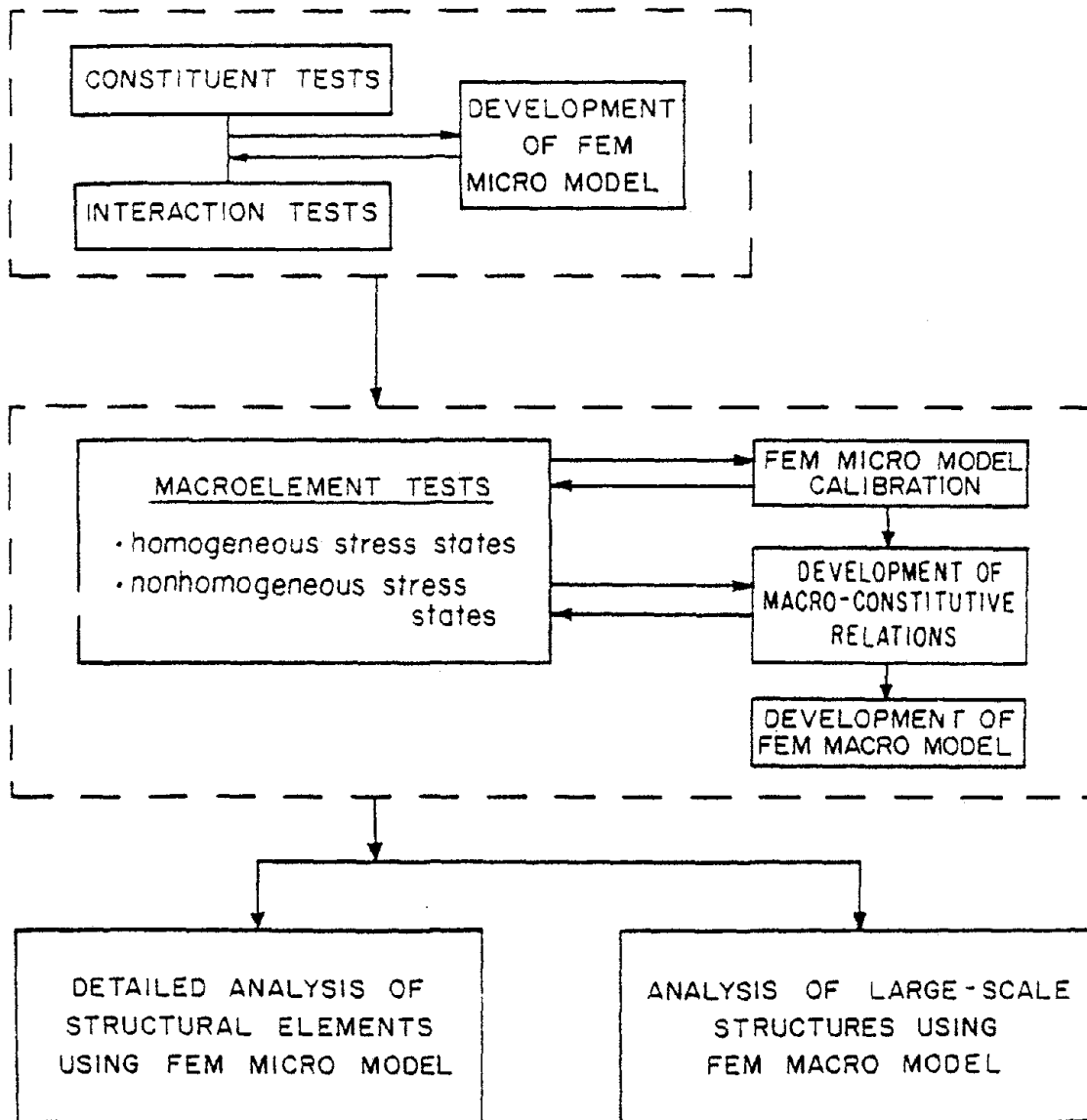


Fig. 1 (a) Methodology of Research Program

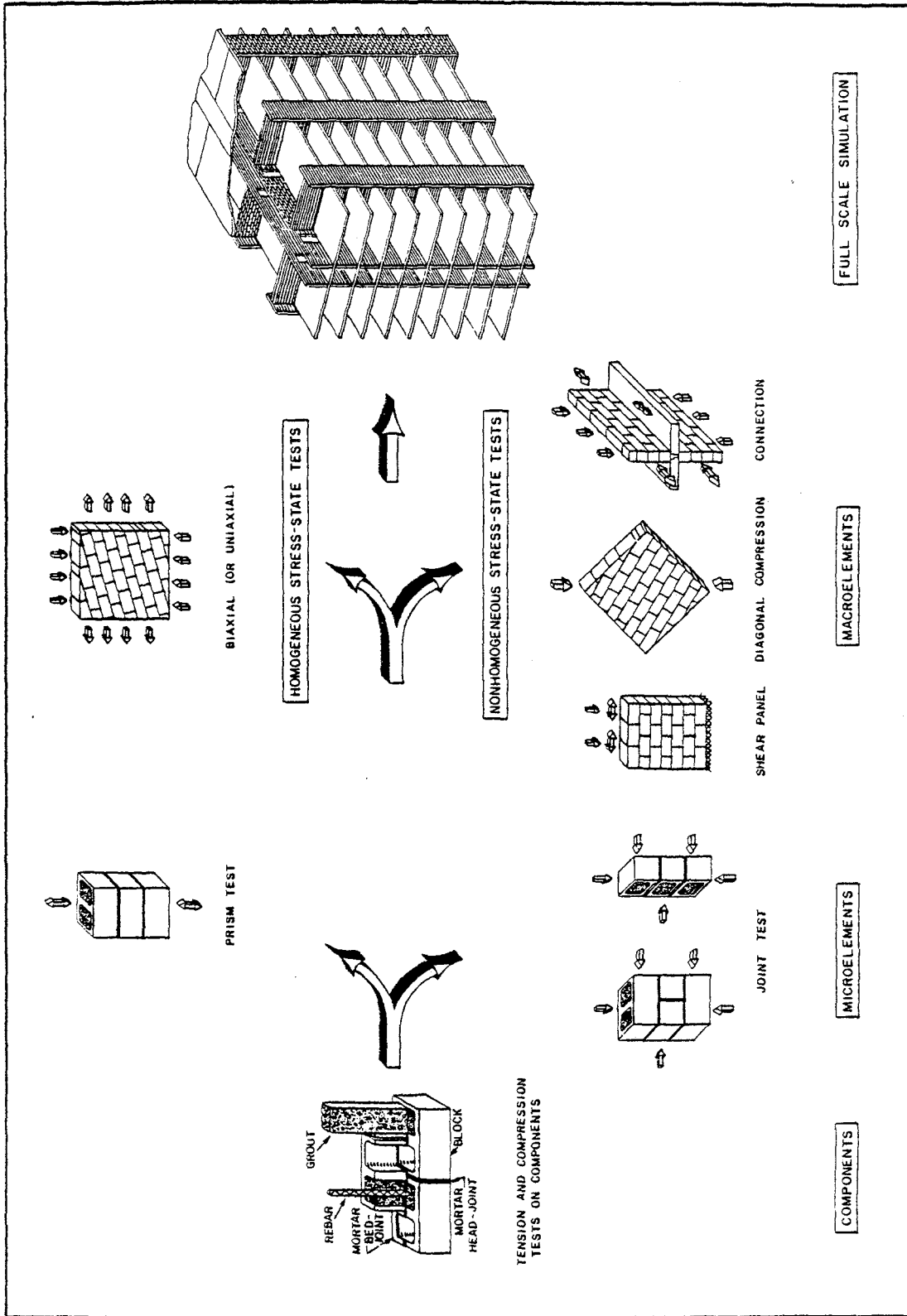


Fig. 1 (b) Evolution of Research Program

## 5. UTILIZATION

Information from this research program may be extracted from different areas and at various levels of sophistication. Some experiments will provide a valuable guide for improved masonry through modified or standardized fabrication techniques. Others will provide a necessary data base for the designer and/or analyst. A numerical program will allow case studies by researchers and detailed analysis by the cognizant engineer. Distillation of data from experiments and case studies should provide a rational basis for meaningful building code modifications.

Some specific examples are perhaps in order at this point. First, in the process of attempting to understand how component properties affect assemblage properties in the laboratory, the validity of certain "standard" tests for stiffness and strength parameters have been questioned. A case in point is the prism test. When this situation occurs modifications in either the test or the interpretation of test data are suggested in an effort to arrive at a better estimate of material properties.

Second, the morphology associated with macroelement or assembly tests have revealed flaws and material variability. Such variability adversely influences material modeling; thus, it is natural to seek fabrication methods which minimize the above. However, fabrication techniques which minimize flaws and variability can also significantly improve the structural integrity of concrete masonry. A case in point here concerns grout compaction using vibration versus puddling; the former yields a superior material at little or no increase in cost.

Third, the basic material parameters that describe material stiffness and strength occur as a natural by-product of each macroelement test. Such data is necessary if one is to conduct even a rudimentary structural analysis.

Fourth, if a successful micromodel of concrete masonry can be developed, one can then commence to study, in an orderly manner, the behavior of structural components such as shear walls, piers, spandrels, columns, etc. That is, one would be able to replace costly experiments involving a vast array of different geometrical configurations of masonry and steel, as well as different boundary conditions, by direct numerical simulations. The application of such simulations could involve analysis, generation of analysis data, or component design. The latter might, as is currently done in the automotive, ship, and aerospace industries, be conducted on an interactive basis. During the creative process, the designer, using a light pen, could modify drawings on the screen of an interactive graphics display system to determine the best design geometry. This could vastly speed the process of analyzing and reconciling the design and performance of a structural component.

In addition to the above, a successful micromodel might be used to generate the data necessary to complete a macromodel. In contrast to the micromodel, any macromodel will be phenomenological. Thus, the constants in such a model must be evaluated. This is usually accomplished experimentally (macroelement tests); however, the same objective can be achieved by numerical simulation using the micromodel.

Fifth, it is not intended that the micromodel be used to analyze a full structure. This is the function of the less detailed, but more efficient macromodel. However, both models require verification at the macro-level. The necessary experiments provide results of immediate use for certain structural configurations and for limited applications.

Finally, the application of the macromodel, together with the finite element method in a numerical program, will allow case studies of typical structural designs. Such studies should provide a wealth of information concerning inelastic response to seismic motion, and should set the stage for rational building code modifications or additions.

## 6. DESCRIPTION OF SMALL-SCALE TESTS

Testing and modeling on the micro-scale commences at the constituent level and requires a knowledge of constituent, constituent-interface, and small assembly behavior under various stress states.

Test data includes elastic moduli, compressive strength, and tensile strength of block, grout, and mortar. Information on unit absorption, and design mixes for each component is also obtained.

Joints are of considerable interest. Joints or interfaces in concrete masonry assemblies constitute both planes of weakness and a major source of damping. Failures frequently initiate in joints, and subsequent deformation and energy absorption may occur by relative slip across joint planes. Joint types selected for study include: 1) ungrouted bed joints; 2) grouted bed joints with and without steel; 3) head joints; 4) combination of head and bed joints; and 5) block-grout interfaces. Mortar geometry includes both full and face-shell bedding. Test specimens in the joint series consist primarily of triplets (three blocks, two interfaces). Six-inch cores are utilized for block-grout interface tests. Joint planes are subjected to constant levels of normal stress and quasi-static monotonic, quasi-static cyclic, or dynamic cyclic shear stress. In each test the initial and post-fracture shear stress vs. normal stress envelopes, and deformation histories, are determined.

In addition to the above, a variety of prism (small assembly) tests have been performed. These are designed to provide basic information on: 1) the influence of the number of courses on compressive strength and associated problems regarding load-platen restraint; 2) the influence of flaws, compaction, and admixtures on compressive and tensile strengths; 3) the correlation of compressive and tensile strengths; 4) correlation of

block, grout, and mortar strengths to prism strengths; 5) stiffness parameters and uniaxial stress-strain behavior (these include Young's modulus in tension, Young's modulus in compression, ratios of moduli to strengths).

## 7. DESCRIPTION OF STATIC AND DYNAMIC BIAXIAL PANEL (MACROELEMENT) TESTS

### 7.1 Homogeneous Stress-States

These tests, which represent a critical step in the continuum modeling process, are unique in that the panels (macroelements) are laid in running bond, but are saw-cut such that the bonds run at oblique incidence or layup to the edges of the finished panel. The rationale: any combination of homogeneous shear and normal stresses on the critical bed and head joint planes can be induced by application of direct (principal) stresses (compression or tension) to panel edges, and the selection of a proper layup angle. The ability to apply direct tensile stresses which exceed the tensile strength of the assembly, and direct compressive stresses with negligible induced shear, follows from the use of a unique polysulfide bonding agent with a low shear modulus ( $\approx 150$  psi) between the specimen and the load distribution fixtures. In the case of uniform load application to each panel edge, the resulting panel stress distribution is globally homogeneous, and hence statically determinate. Thus, in contrast to conventional test methods<sup>(2)</sup>, the determination of material properties is not prejudiced by boundary constraints; further, in contrast to indirect methods<sup>(1)</sup>, extraction of biaxial failure data does not necessitate a conjecture of isotropic, linear elastic material behavior prior to macro-cracking.

Figure 2 illustrates the basic concept of oblique layup testing. If the  $x_1, x_2$  - axes are principal stress directions, then the stress resultants\*  $N'_{11}, N'_{22}, N'_{12}$  associated with axes  $x'_1, x'_2$  along the bed and head joint directions are related to the principal stress resultants  $N_{11}, N_{22}$  through

---

\*Stress resultants are related to stress by  $\sigma_{ij} = N_{ij}/t$ , where  $t$  is the panel thickness.

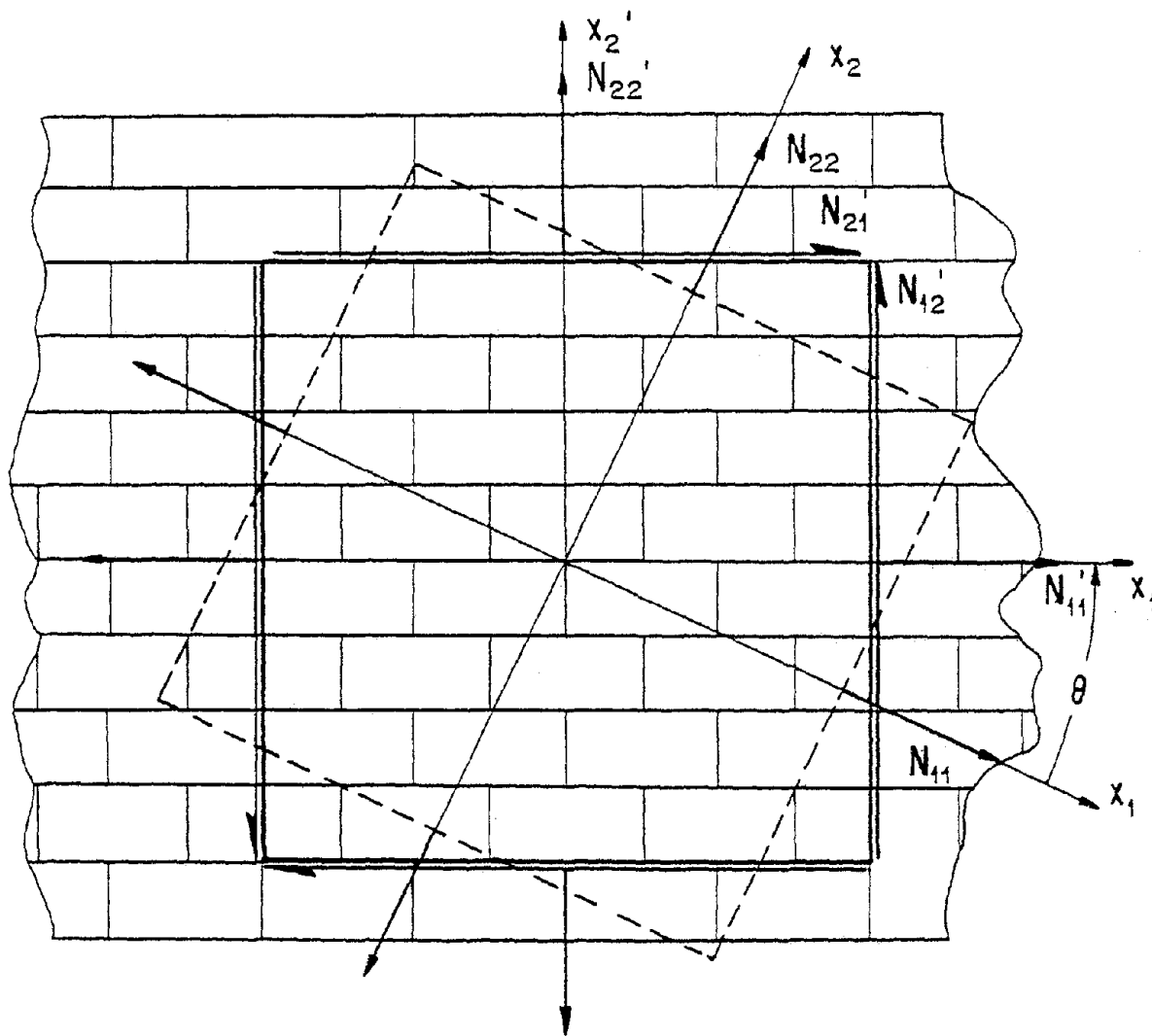


Fig. 2 Stress Transformation

$$N'_{11}, N'_{22} = \frac{N_{11} + N_{22}}{2} \pm \frac{N_{11} - N_{22}}{2} \cos 2\theta \quad ,$$

$$N'_{12} = \frac{N_{22} - N_{11}}{2} \sin 2\theta \quad . \quad (1)$$

Equations (1) imply that any homogeneous stress state ( $N'_{11}$ ,  $N'_{22}$ ,  $N'_{12}$ ) in a panel with surfaces oriented parallel to the head and bed joints can be obtained by selecting an appropriate layup angle  $\theta$  and direct stress resultants  $N_{11}$ ,  $N_{22}$ . In particular, given a desired stress state ( $N'_{11}$ ,  $N'_{22}$ ,  $N'_{12}$ ), the combination ( $N_{11}$ ,  $N_{22}$ ,  $\theta$ ) is selected according to

$$\tan 2\theta = \frac{-2N'_{12}}{N'_{11} - N'_{22}} \quad ,$$

$$N_{11}, N_{22} = \frac{N'_{11} + N'_{22}}{2} \pm \frac{N'_{11} - N'_{22}}{2} \cos 2\theta \mp N'_{12} \sin 2\theta \quad . (2)$$

The panels in the homogeneous stress-state test series are 64-by-64 inch in planar dimension, and are precision cut from 8-by-8 foot fully grouted unreinforced or reinforced concrete masonry walls. Cutting is accomplished by use of a dynamically balanced, 30-inch-diameter, diamond-edge saw on an air-driven turbine attached to fixed rails.

A schematic of the biaxial test procedure is shown in Fig. 3. The actual setup is illustrated in Fig. 4. The load conditions include quasi-static monotonic, quasi-static cyclic, and dynamic cyclic (.05 to 5Hz). The system is capable of load, displacement, or combined load-displacement control. This is accomplished with a mini-computer-controlled, closed-loop-hydraulic-servo system utilizing four active actuators on each panel side connected to load distribution fixtures. This test system is housed in a massive dual test frame, Fig. 5. A high-speed digital data acquisition system (14 bits absolute value plus sign, 300 samples/sec/channel or 12,000 samples/sec. total), Fig. 6, monitors 40 channels of

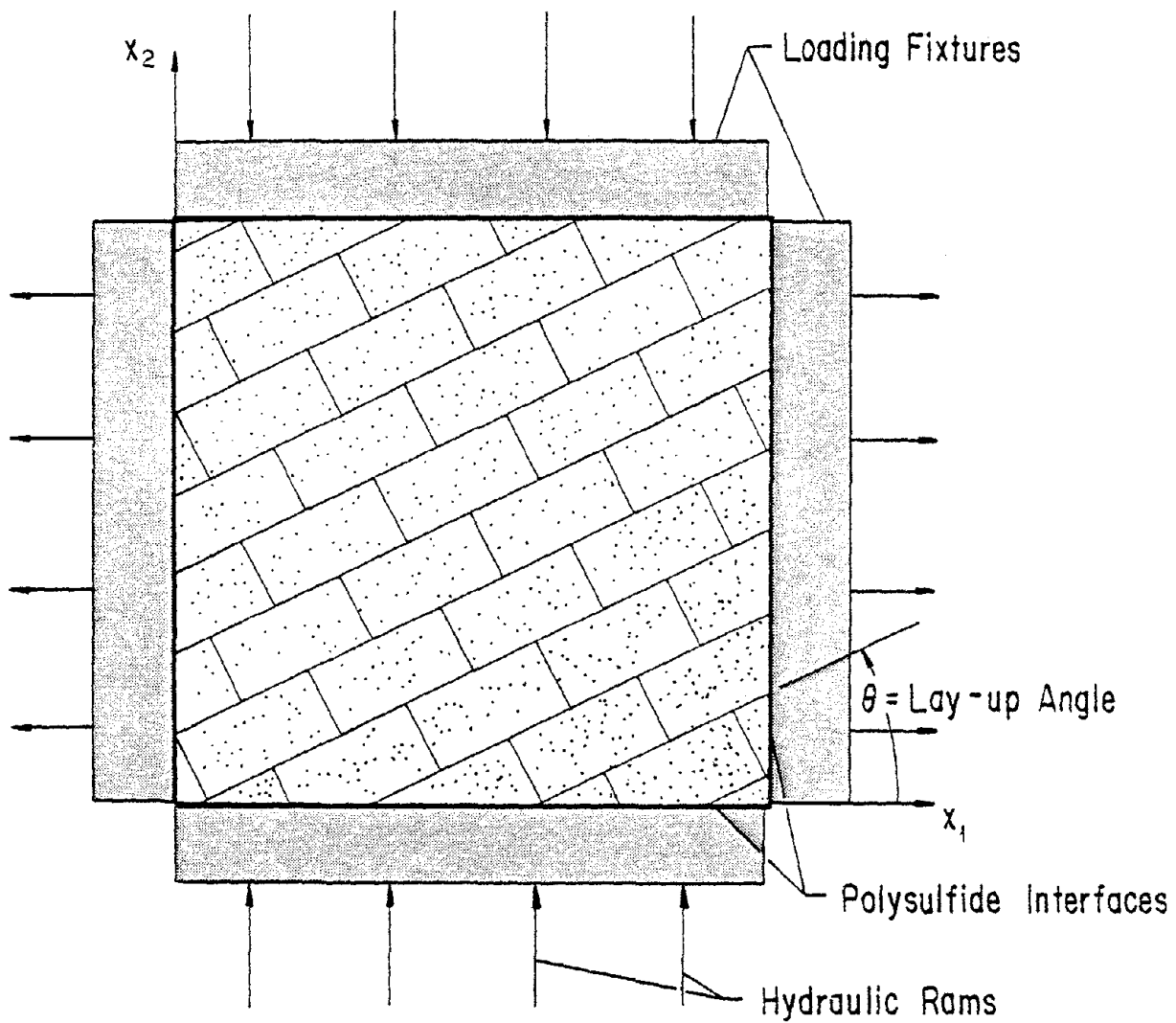


Fig. 3 Loading Schematic

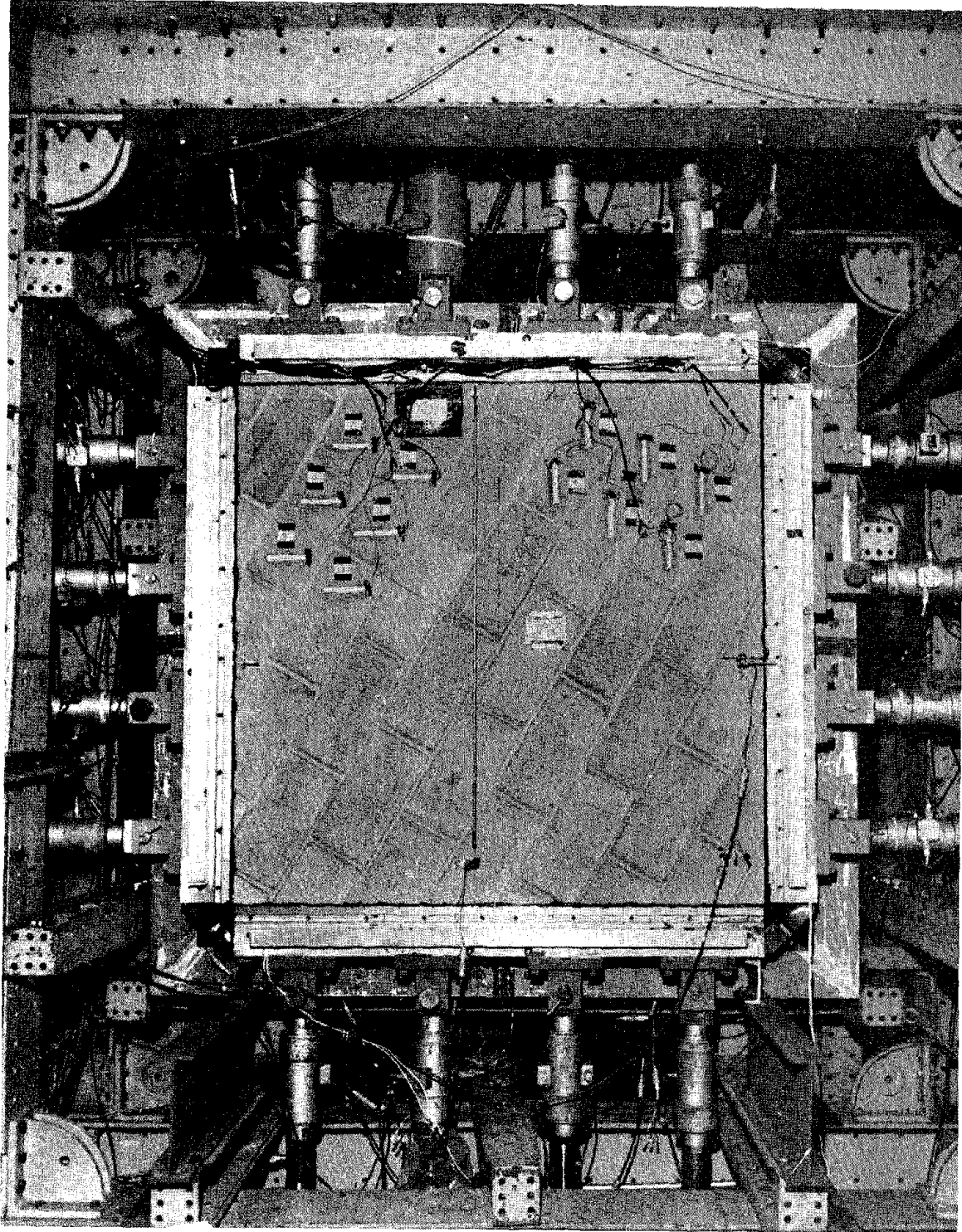


Fig. 4 Biaxial Fixture

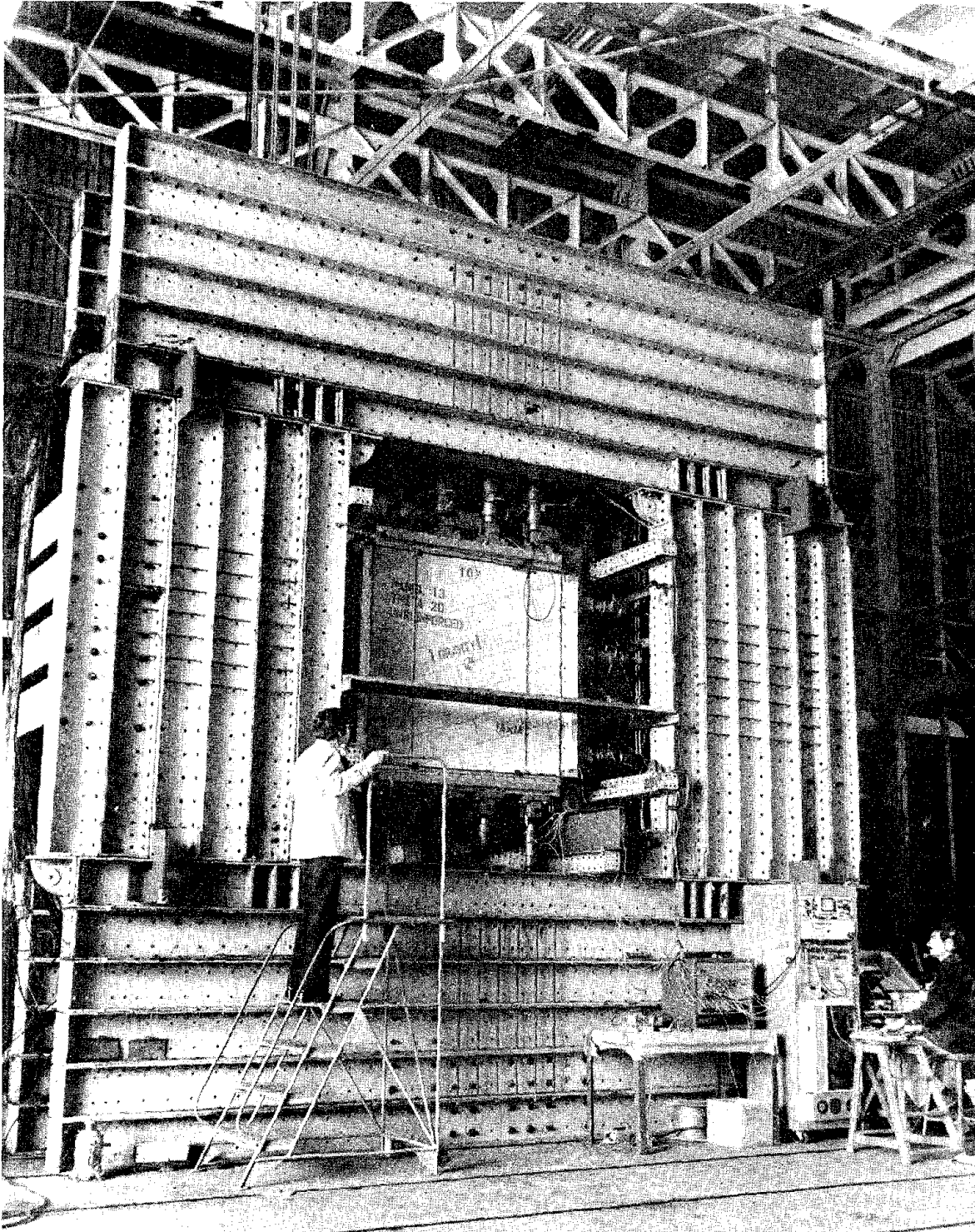


Fig. 5 Biaxial Test Frame

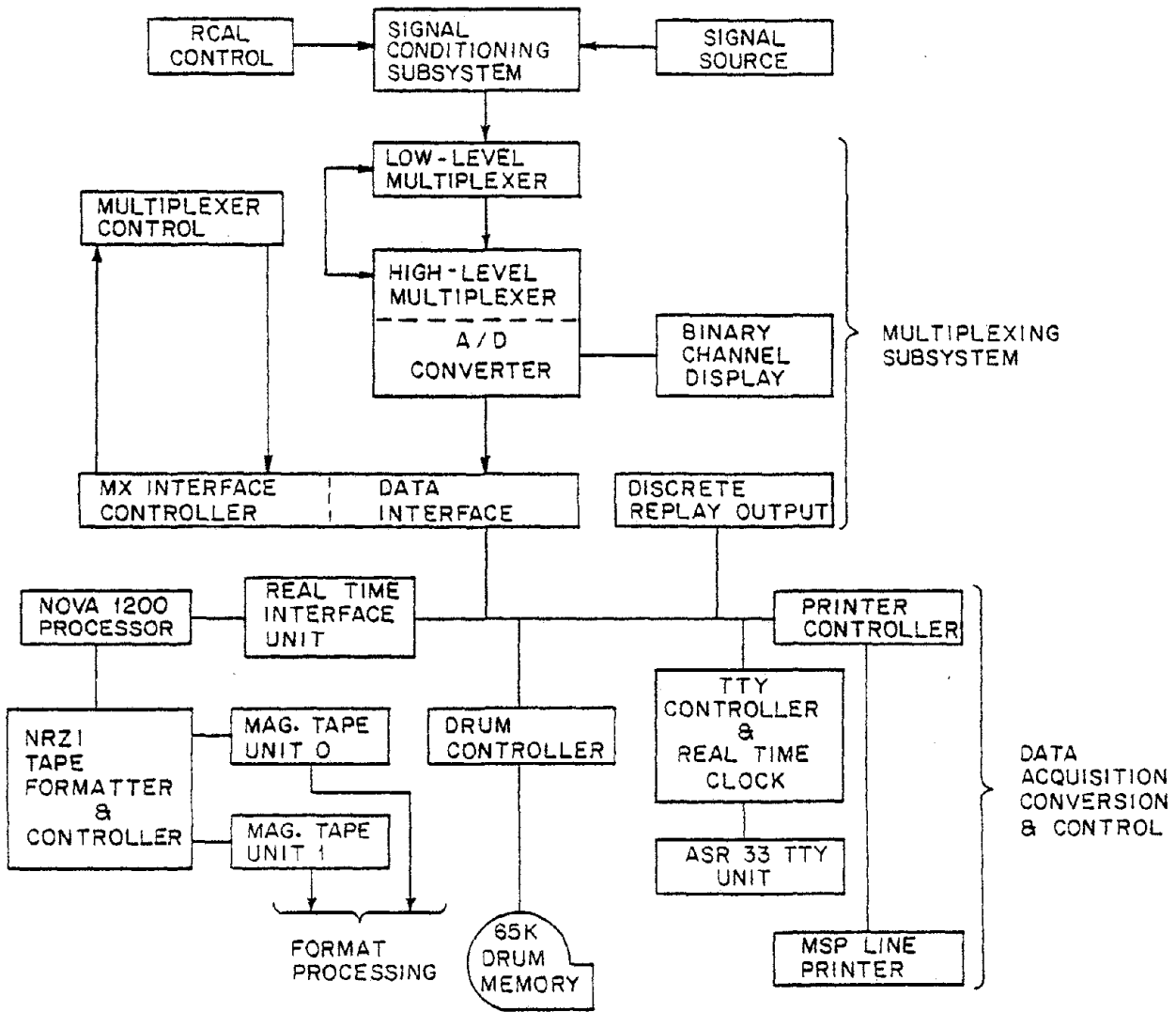


Fig. 6 Data Acquisition

signals from load-cells, linear variable differential transformers (LVDT's), and strain gages.

Rheological aspects of singular interest include: 1) elastic properties; 2) degree of anisotropy of elastic properties; 3) damping or stress-strain hysteresis in the "elastic" regime; 4) strain-rate sensitivity of item 3 in the .05 to 5Hz range; 5) initial "yield" or macrofracture surface in stress-space; 6) degree of anisotropy of item 5; 7) ultimate strength; 8) influence of load history on the degradation of stiffness and ultimate strength; 9) hysteresis in the highly nonlinear range; 10) role of reinforcing steel geometry and volume in the control of macrocracking; and 11) flaw sensitivity.

## 7.2 Nonhomogeneous Stress-States

These tests constitute an advanced step in the micromodeling process and a first evaluation of the limits of applicability of the homogeneous stress-state data and/or an associated continuum model. Two basic test-types are utilized: 1) diagonal compression and 2) simple shear deformation.

The diagonal compression test is designed to evaluate the predictive accuracy of the failure (initial macrocracking) theory, developed from homogeneous stress-state data, in a nonhomogeneous stress field. Theoretically, the use of homogeneous stress-state data is based upon an assumption that the dominant characteristic length associated with variations in the stress field is "large" in comparison to the largest masonry micro-dimensions - 8 to 16 inches (the block size). From a practical standpoint, it is expected that such data may be utilized when "large" is only several microdimensions.

The diagonal compression test is illustrated schematically in Fig. 7.

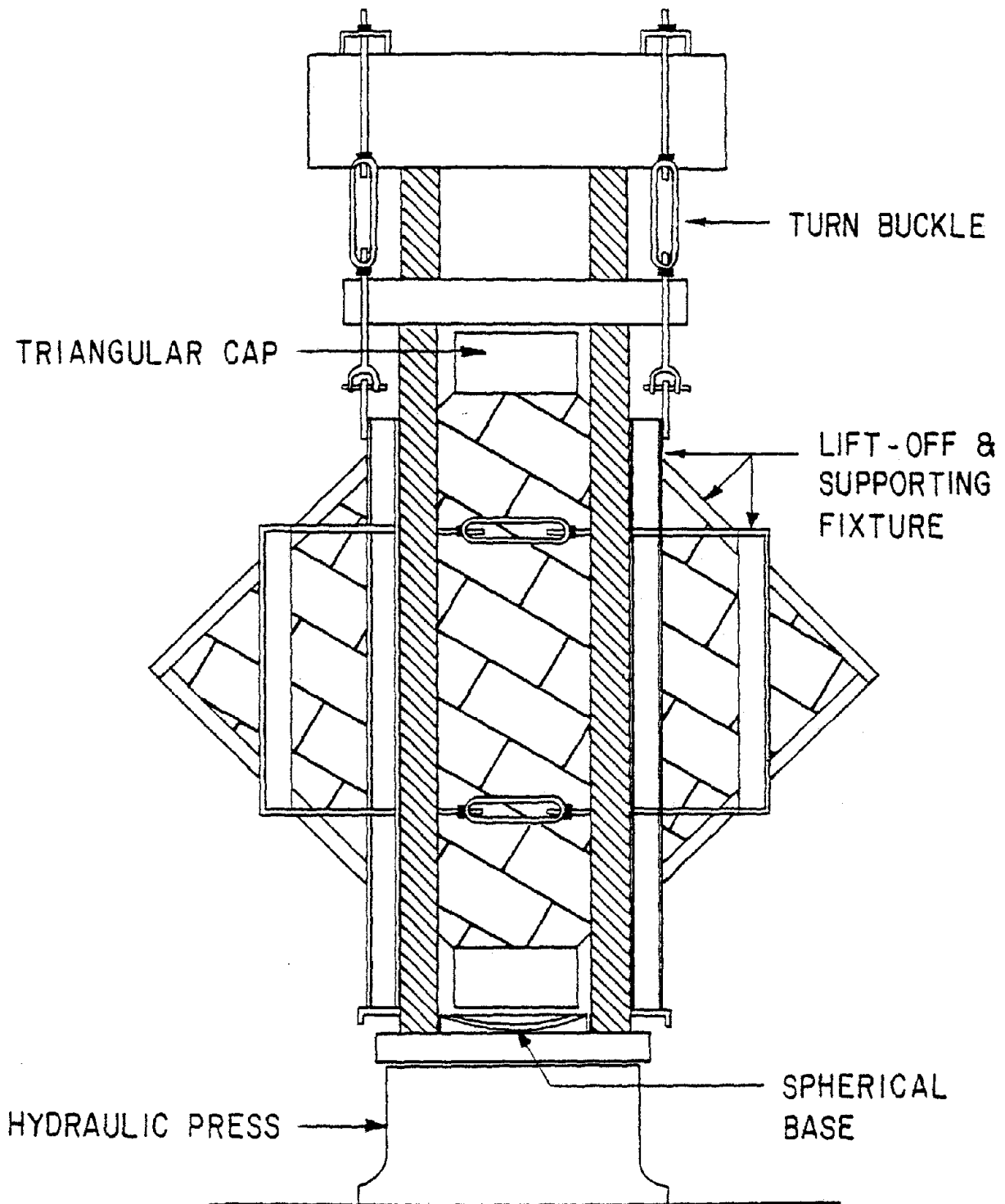


Fig. 7 Diagonal Compression Test

Under concentrated diagonal compressive loads, the central region of the test specimen is subjected to a biaxial stress-state, Fig. 8, which is reasonably uniform over a centered area of diameter equal to approximately 20-25 percent of the diagonal. For the 64 by 64-inch specimen utilized, this diameter is roughly 1 to  $1\frac{1}{2}$  times the largest microdimension. Hence, there is a severe test of the limits of applicability of the homogeneous data. The mode of comparison is measured vs. predicted failure loads,  $P_d$ ; the latter is based upon the initial macrofracture surface as determined from the homogeneous tests. Data from an array of LVDT's, strain gages, and a load cell is obtained with the aid of the high speed digital data acquisition system mentioned previously.

The "simple shear deformation" test is a shear-wall test wherein the top and bottom planes of the specimen are constrained to remain essentially parallel. This test-type serves to calibrate all modeling in a region of primary interest. The rheological items of interest here are similar to those listed in the discussion of homogeneous stress states.

The biaxial test system described previously is capable (with modifications as shown in Fig. 9 (a)) of producing simple shear deformation under ideal conditions as far as control is concerned; however, in view of an existing shear wall test program at U. C. Berkeley, it was decided to attempt to extract the necessary data for this case from this program. The Berkeley test setup is illustrated schematically in Fig. 9 (b). It is a structural test and was not specifically designed for the purpose of furnishing fundamental material - behavioral information. The complexity of this test necessitated a considerable effort on the part of the U. C. San Diego research team with respect to the installation of a vast array of probes, data acquisition (the high speed U. C. San Diego digital data acquisition system was used), and extensive data reduction (conducted at U. C. San Diego).

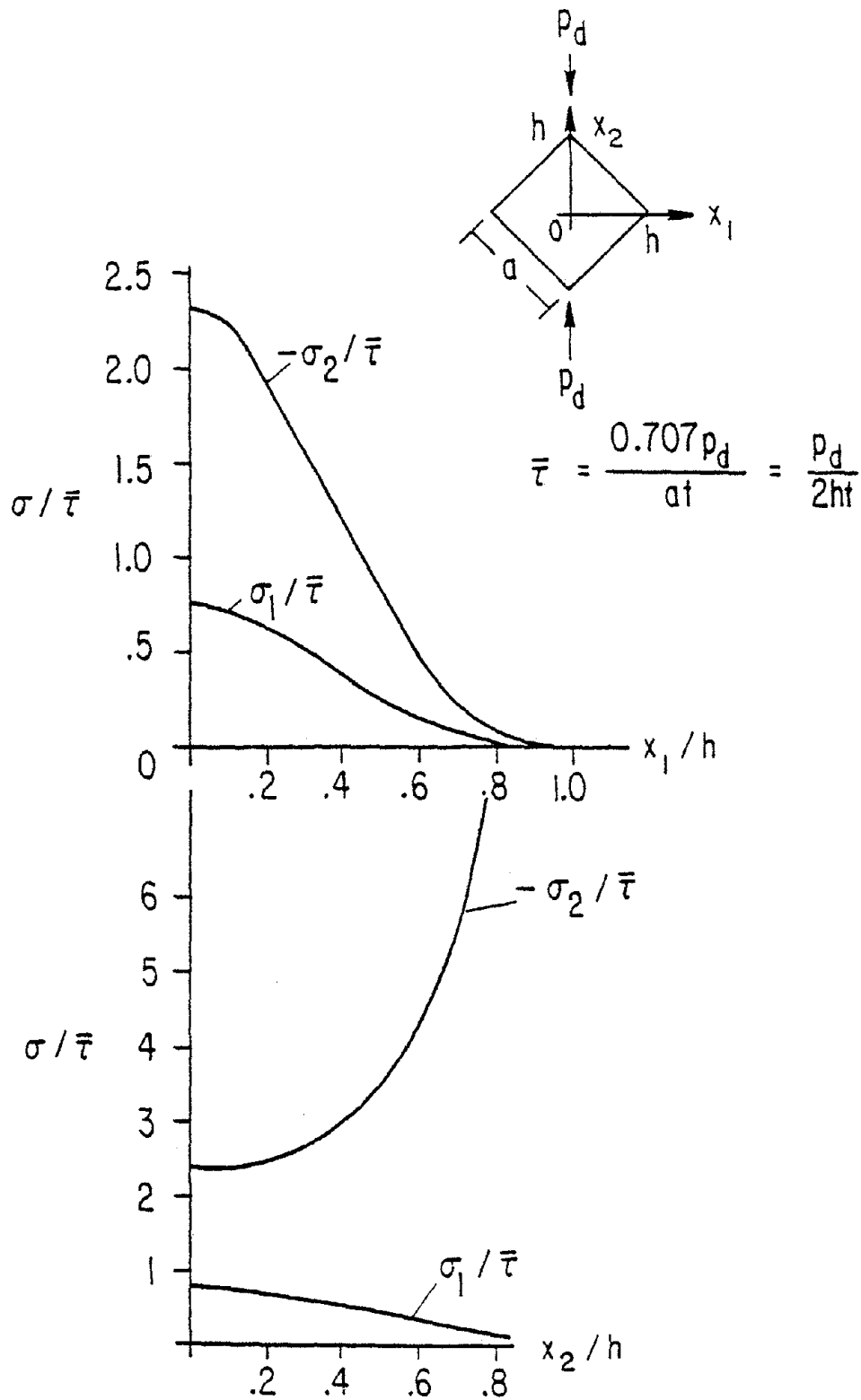


Fig. 8 Principal Stress Distribution on the Planes  $x_2 = 0$  and  $x_1 = 0$

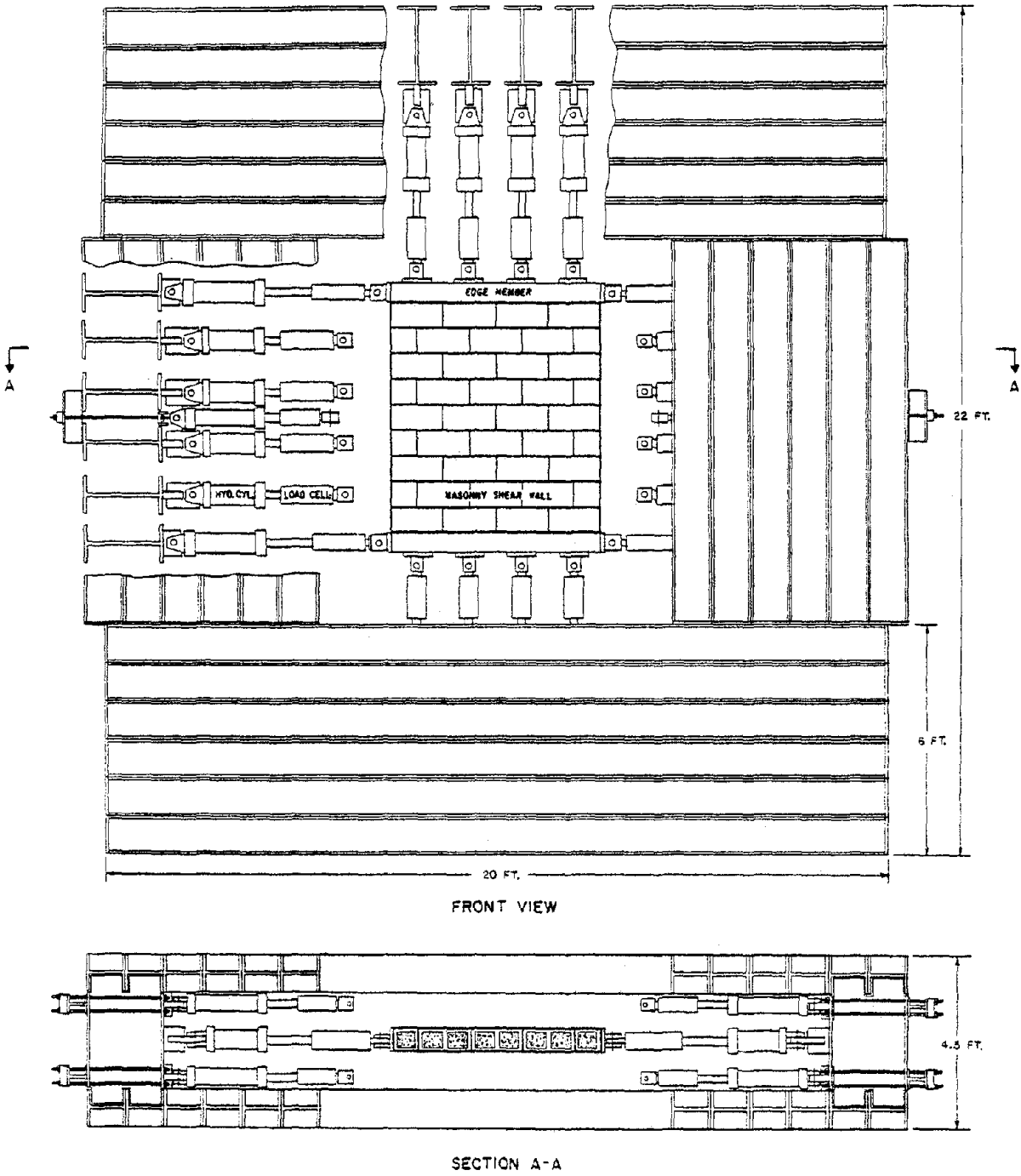


Fig. 9 (a) Biaxial Frame Modified for Shear Test

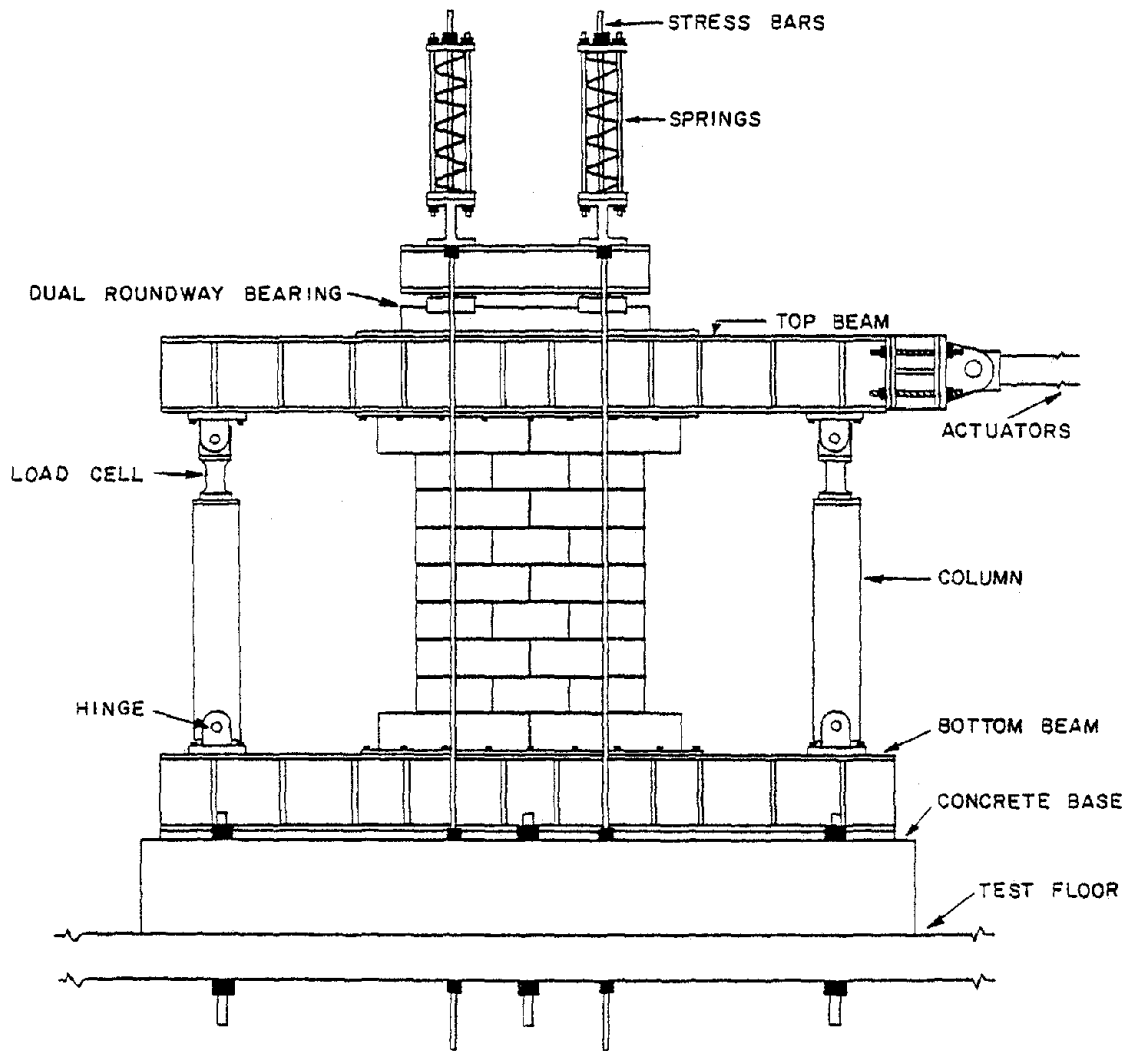


Fig. 9 (b) Schematic of the Berkeley Shear Wall Test

## 8. SELECTED RESULTS - PANELS (MACROELEMENTS) UNDER HOMOGENEOUS STRESS-STATES

A complete description of the biaxial tests<sup>(4, 5, 6)</sup> is beyond the scope of this report. For simplicity, attention is focused below on sample results obtained to date under this program. Brief discussions are presented concerning the homogeneous stress-state tests and the following associated items: 1) the initial macrocracking surface; 2) macrocracking or failure and isotropy; 3) prediction of the initial macrocracking surface from component data; 4) influence of reinforcing steel on initial and post-macrocracking behavior; 5) elastic moduli and anisotropy; 6) elastic moduli and strength; 7) damping and strain-rate effects in the linear range; 8) the influence of flaws, compaction and admixtures on strength; and 9) finite element prediction of failure.

### 8.1 Initial Macrocracking Surface

From both design and analysis standpoints, this represents one of the most important aspects of material behavior. For unreinforced specimens, the initial macrocracking surface in stress space is the set of stress points at which failure occurs. For reinforced specimens, and under normal reinforcing volumes, the initial macrocracking surface represents the set of stress points at which major cracking occurs together with a primary load transfer from masonry to steel; the latter is usually accompanied by a substantial drop in stress under monotonically increasing strain, reflecting the reduction in the load carrying capacity of the specimen over a certain interval.

Complete mapping of the initial macrocracking surface in the stress space ( $N'_{11}$ ,  $N'_{22}$ ,  $N'_{12}$ ), or the principal stress vs.  $\theta$ -space ( $N_{11}$ ,  $N_{22}$ ,  $\theta$ ), is a major undertaking. This problem is, however, alleviated

by two factors: 1) extensive calculations concerning shear walls and other complex structures reveal that, in most applications, the normal stress on head joint planes is small when compared with normal and shear stresses on bed joint planes, i. e. ,

$$N'_{11} \ll N'_{22} \quad , \quad N'_{12} \quad (3)$$

and 2) experimental data reveals a weak dependence of strength on the layup angle  $\theta$ , i. e. , the masonry under consideration is approximately isotropic - a point to be discussed later.

A typical intersection of the initial macrocracking surface with the plane  $N'_{11} = 0$  is illustrated in Fig. 10 for fully grouted\* specimens, the component properties of which are given in Table 1 for one specimen set ("batch 6"). The rays in this figure represent the layup angles and the corresponding proportional loading which results from the condition  $N'_{11} = 0$  in equations (1) and (2); this furnishes the proportional loading relation

$$N_{11} = - N_{22} \tan^2 \theta \quad . \quad (4)$$

Data points, which represent statistical means of repeated tests, are denoted by circles and triangles for unreinforced specimens and open squares for reinforced specimens. Stresses shown are based upon net cross-sectional areas. Steel volumes utilized in the reinforced masonry are discussed in a subsequent section. The data indicates, as should be expected, that the initial macrocracking surface is not appreciably influenced by reinforcement for practical ranges of steel volumes.

For unreinforced specimens, two basic failure modes were observed. In the tension zone (see Fig. 10), and in the compression zone for

---

\* All panels discussed in this report are fully grouted.

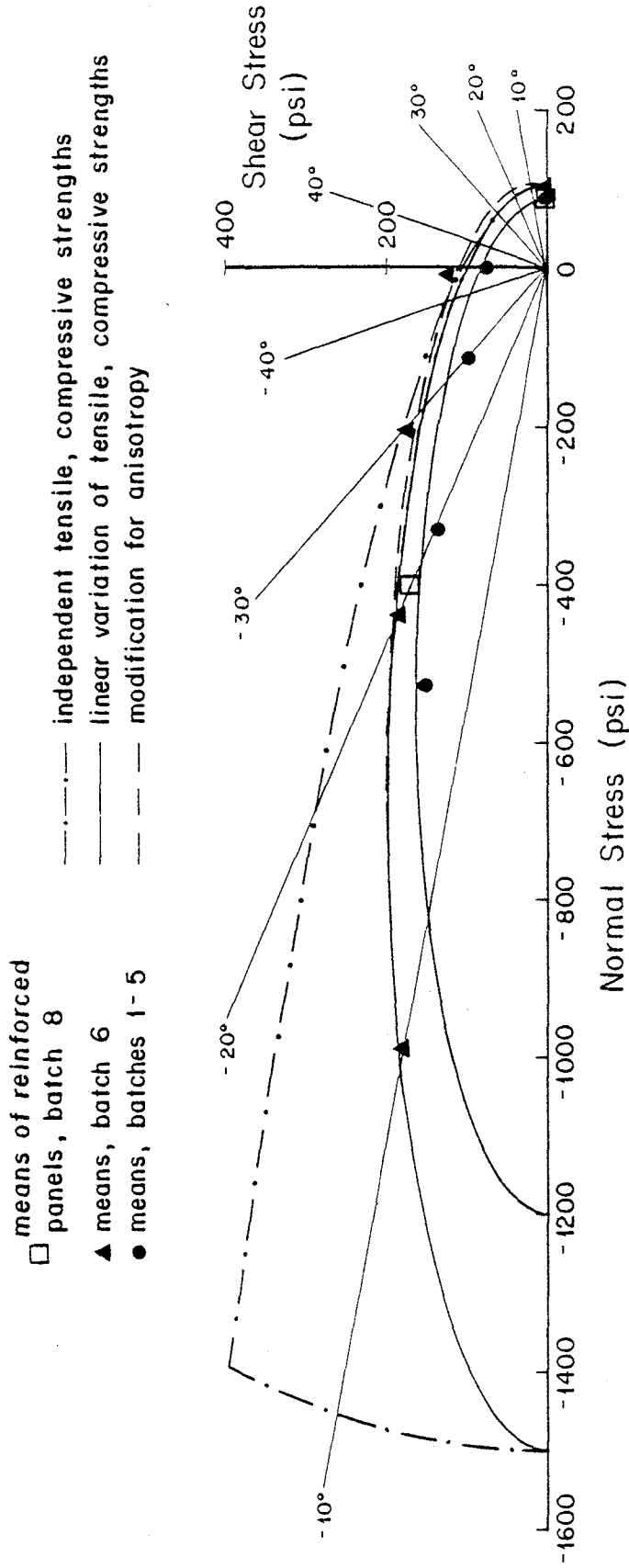


Fig. 10 Failure Envelope for Zero Head Joint Normal Stress

Table 1. Component Properties for Macroelements and Prisms

	Block <sup>†</sup>	Mortar	Grout <sup>‡</sup>
Compressive Strength (ksi)	3.97	2.42	4.03
	2.97	2.86	3.53
	3.27	2.39	3.51
	2.95	2.66	3.79
	3.41	2.83	4.15
	3.16	2.03	3.69
	3.00	1.77	3.69
	3.68		4.32
			4.35
			3.98
		4.17	
		3.25	
mean	3.30	2.42	3.87
std. dev.	.37	.41	.35
Tensile Strength (psi)	310	229	247
	291	253	253
	373	162	324
	294		
	297		240
	363		
	377		
mean	329	215	266
std. dev.	40	47	39
Young's Modulus, Compression (psi)	2.5 × 10 <sup>6</sup> (2.2 - 2.8)		2.6 × 10 <sup>6</sup> (2.5 - 2.7)

<sup>†</sup>Block: Type N, ASTM C90 Block; test coupons approx. 4.0" x 6.5" cut from face shells.

<sup>‡</sup>Grout: Coarse grout, ASTM C476 (6-sack grout).

$|\theta| > 15$  deg., a brittle failure with a single crack was frequently observed, as illustrated in Fig. 11 (a) ( $\theta = -45$  deg.). In the compression zone for  $|\theta| < 15$  deg., failure consisted of multiple cracks, as shown in Fig. 11 (b) for  $\theta = -10$  deg. For reinforced specimens, multiple cracking was most frequently observed (this point will be discussed subsequently).

The curves in Fig. 10 represent several macroscopic, analytical failure models considered to date. The dotted curve, shown for "batch 6", is based upon the premise that failure occurs when a principal stress reaches either the tensile strength or the compressive strength associated with a uniaxial, 0 deg. layup, test. The solid curves result from the premise that the failure envelope in principal stress-space is linear in the tension-compression zone, as illustrated in Fig. 12 for plain concrete under biaxial stress states. The resulting model is seen to provide a more accurate description of material behavior. The solid curves in Fig. 10 correspond to estimated (from prism tests) compressive strengths, and measured (from 0 deg. layup panels) uniaxial tensile strengths for two groups of specimens. Note that only two tests are necessary for construction of this failure model: 1) the uniaxial tensile strength and 2) the uniaxial compressive strength. The dashed curve in Fig. 10 represents a modification of the solid curve for "batch 6", to account for anisotropy; this was accomplished by allowing the uniaxial tensile strength to vary with  $\theta$ ; this variation is discussed below. As can be observed, the correction is small. For such cases, the initial macrocracking model depicted by Fig. 13 is proposed (the compression-compression quadrant will be treated later). The premise of linearity of the failure envelope in the tension-compression zone of principal stress space is substantiated by biaxial data, Fig. 14, on unreinforced macroelements.

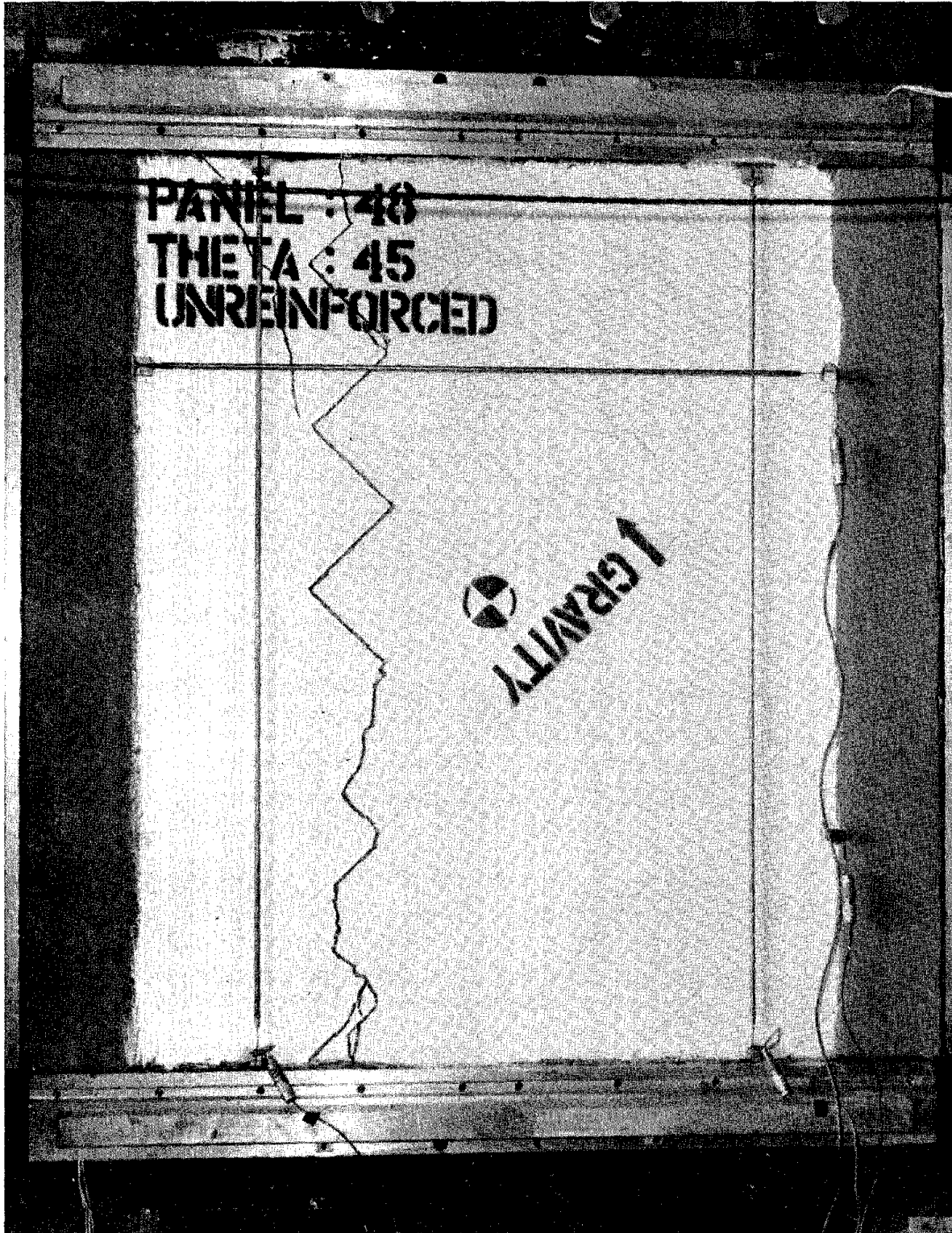


Fig. 11 (a) Typical Joint Failure

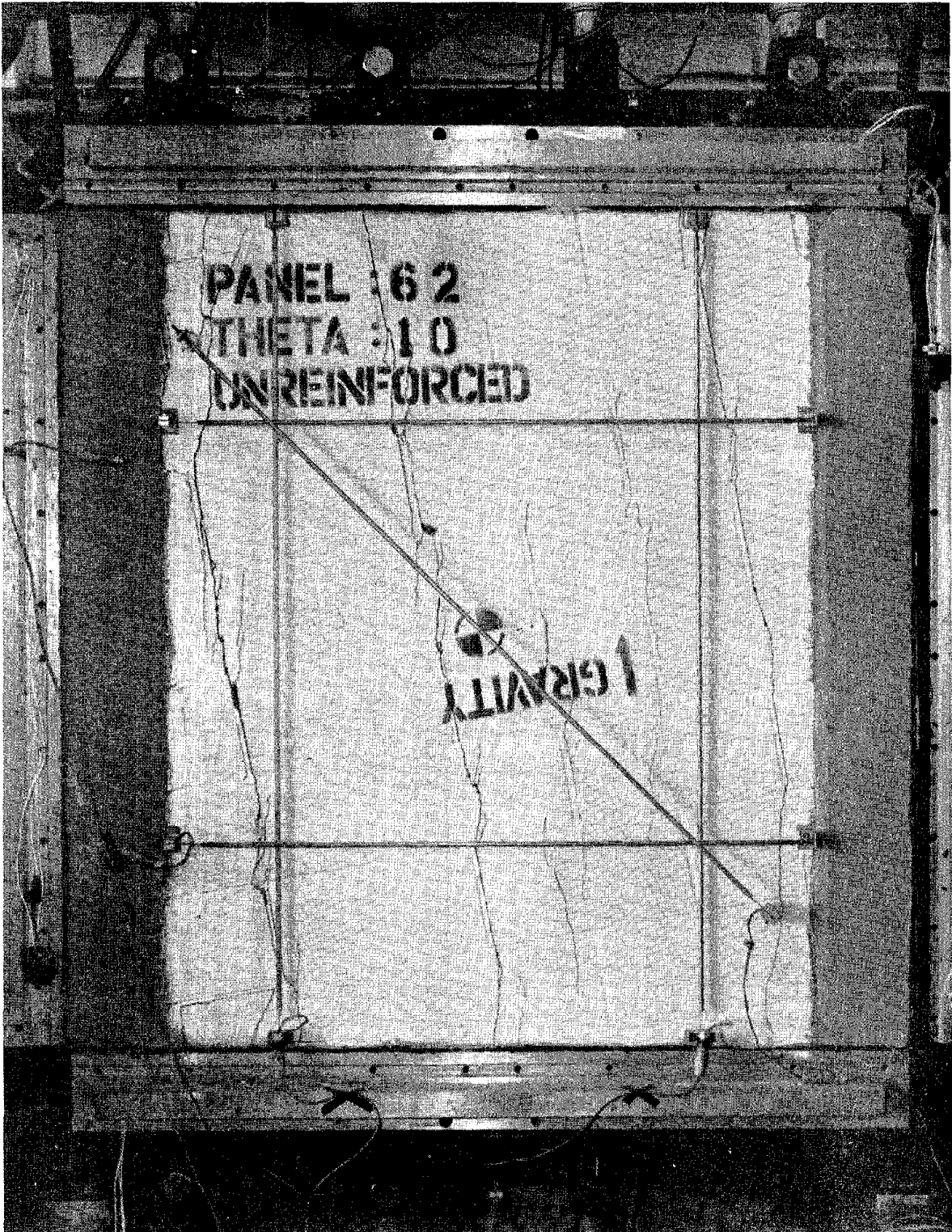


Fig. 11 (b) Multi-Crack Failure

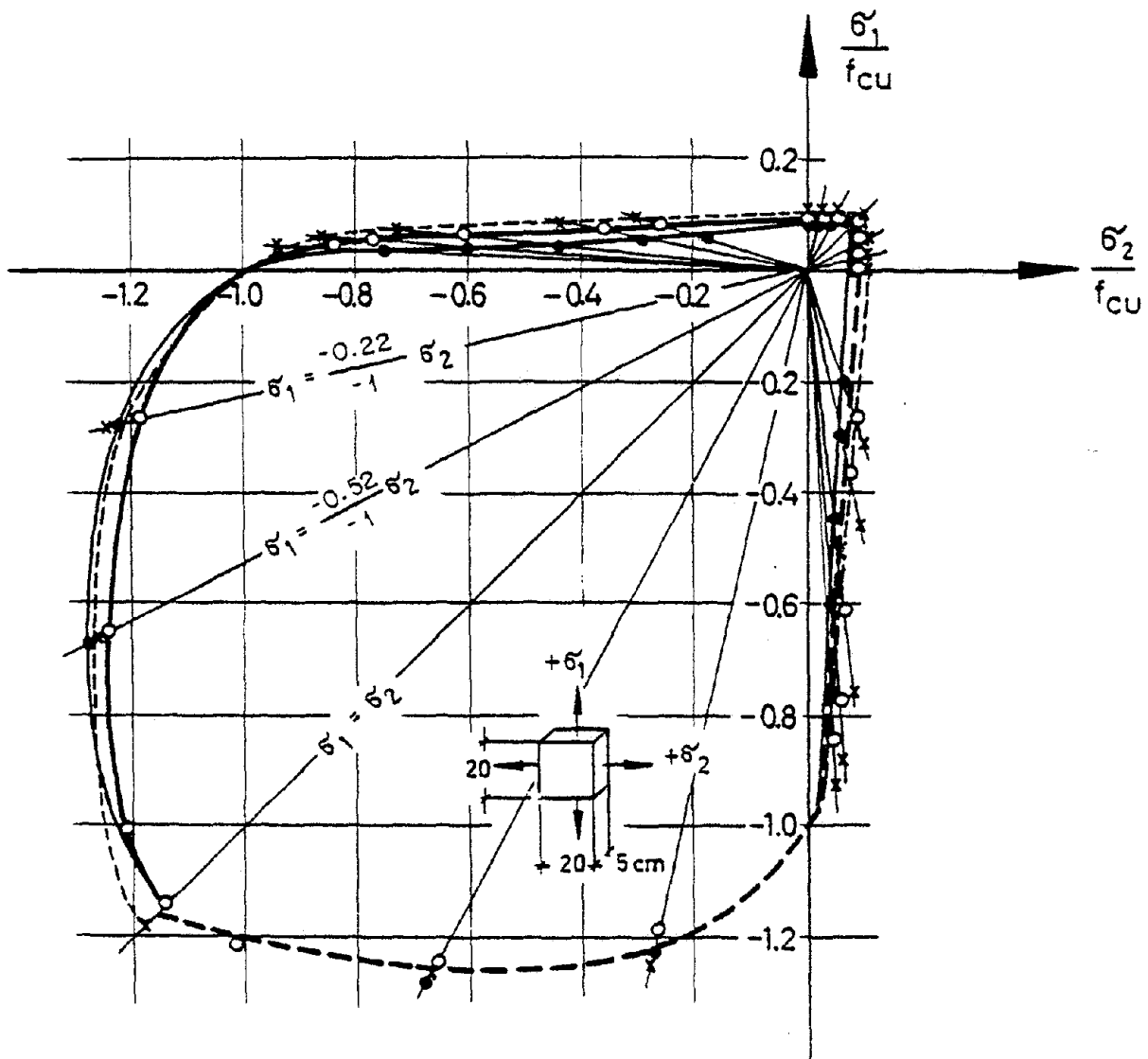


Fig. 12 Biaxial Strength of Concrete

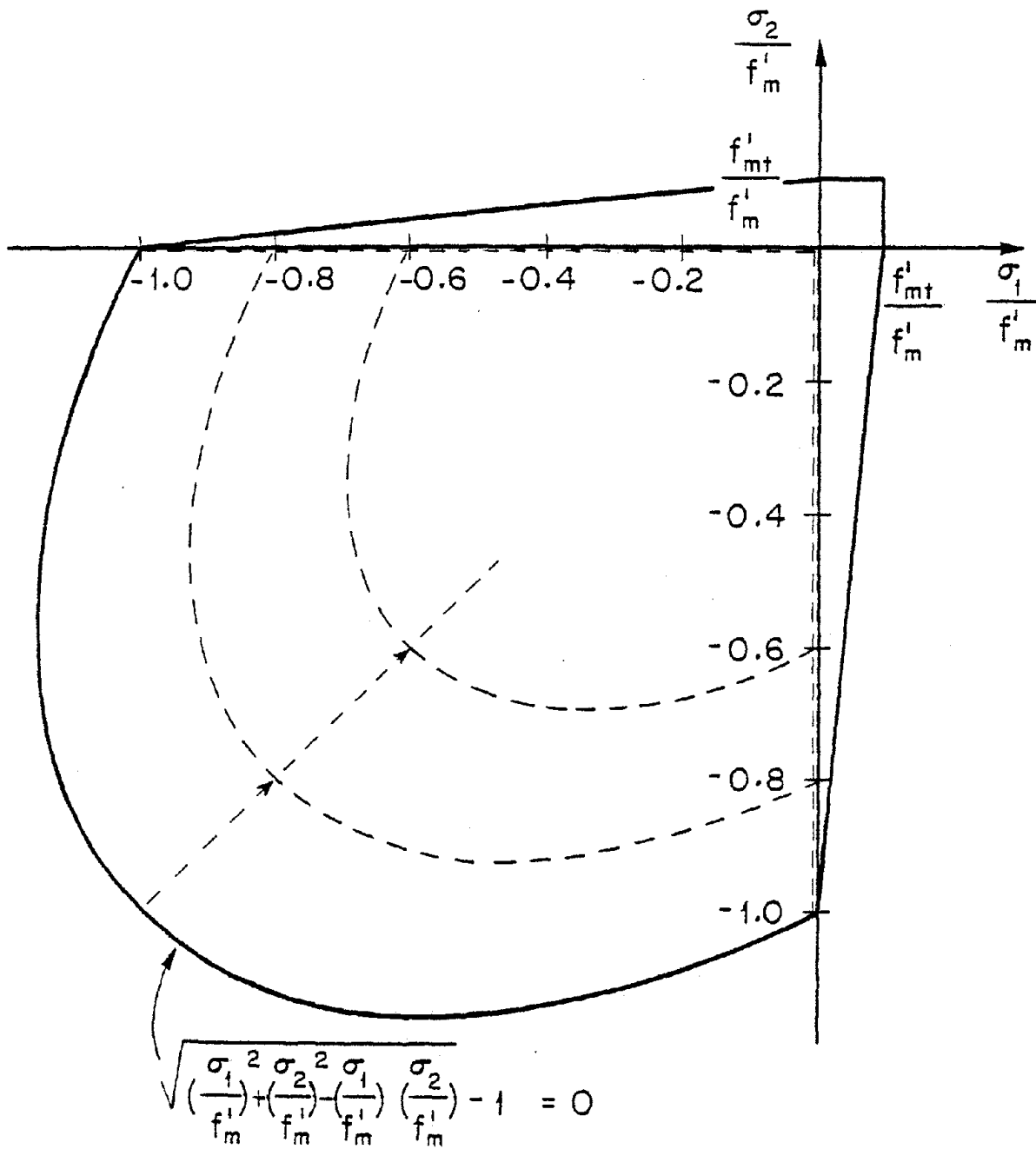


Fig. 13 Initial Macrocracking Envelope

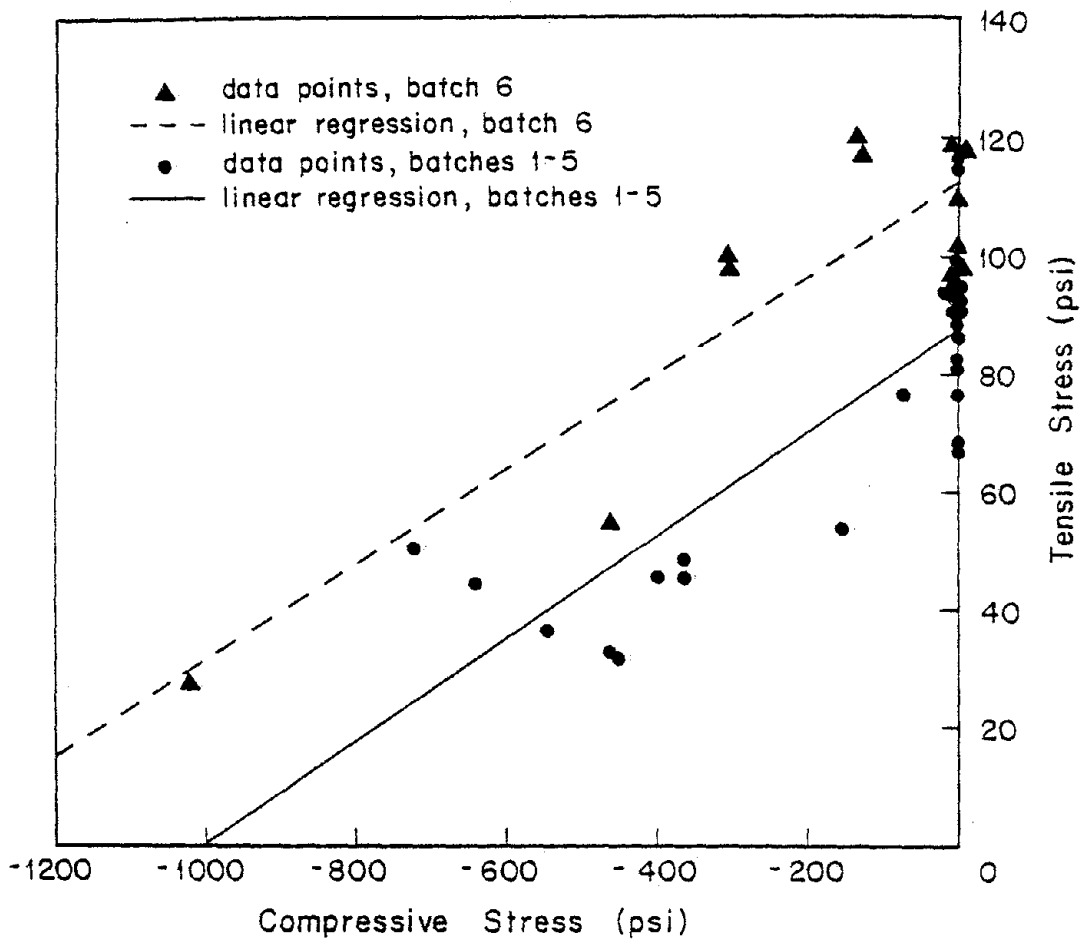


Fig. 14 Dependence of Panel Tensile Strength on Compressive Stress

## 8.2 Macrocracking or Failure and Isotropy

Data on fully grouted unreinforced macroelement tensile failure indicates a slight increase in strength for layup angles near 45 deg., as shown in Fig. 15, but the premise of material isotropy can be seen to hold within normal data-scatter for brittle materials of the type under consideration. For a layup angle of 0 deg., tension is applied to the bed joints. Each curve in Fig. 15 represents a fit to the data of a second degree polynomial.

It should be noted that material anisotropy for a macroelement is a direct function of block and grout strengths. The strength combinations under study, by accident, led to an essentially isotropic material. The latter can be destroyed by a nonjudicious selection of block and grout strengths. Estimation of material anisotropy from component properties is discussed below.

## 8.3 Prediction of Initial Macrocracking from Component Data

From both design and analysis viewpoints, it is highly desirable that one be able to predict macroelement properties from component properties and geometries. Extensive testing has revealed that this is indeed possible. The degree of success and the complexity of the model involved, however, is a strong function of the number (distribution) and type of flaws in the masonry. Several examples concerning the initial macrocracking surface are given below to illustrate this point.

Consider once again the initial macrocracking theories represented by the solid or dashed curves of Fig. 10. Recall that the solid curves require material isotropy and two data points: the uniaxial tensile strength and the uniaxial compressive strength. Correction for anisotropy (dashed curve) requires an estimate of the variation of uniaxial tensile strength

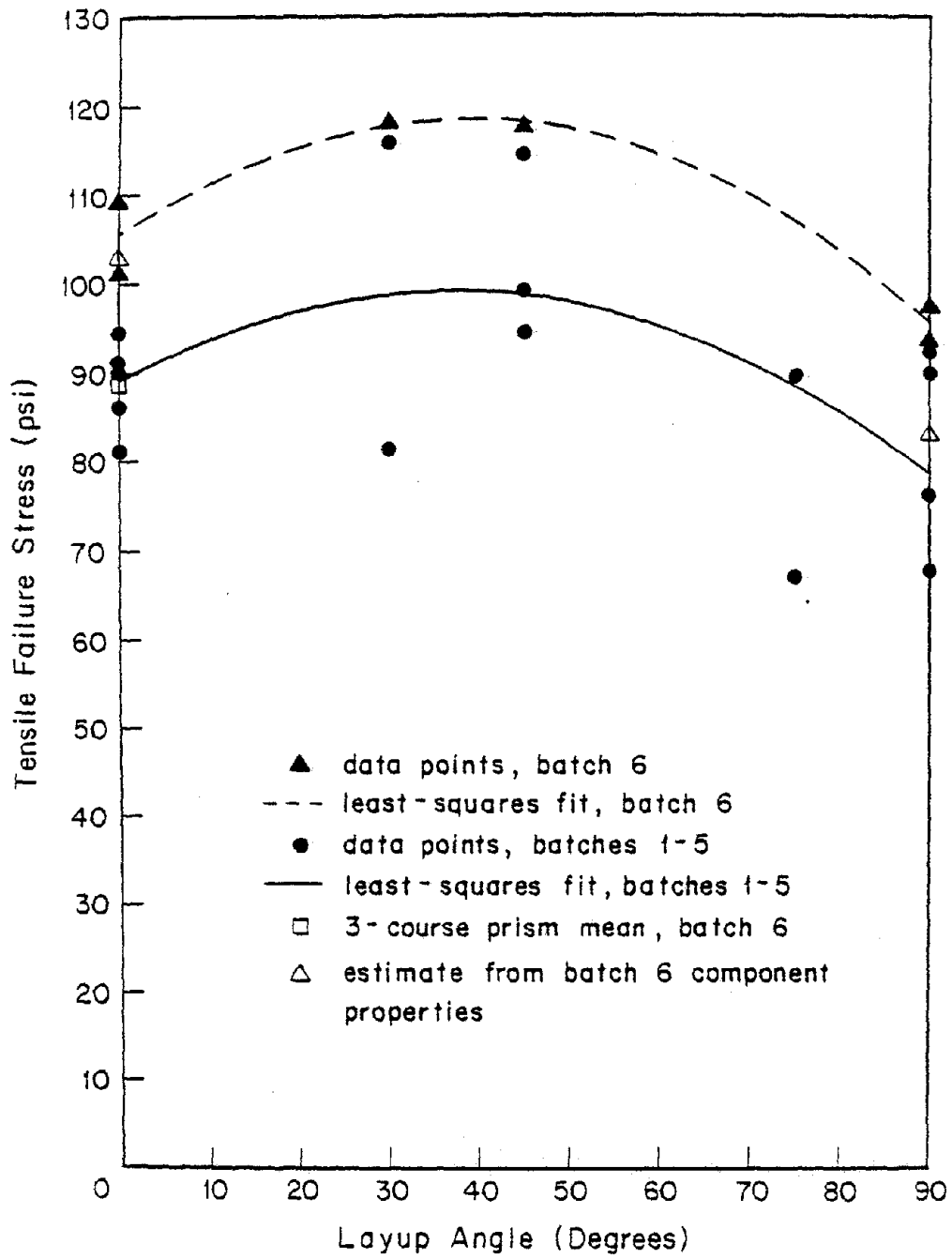


Fig. 15 Panel Tensile Strength Anisotropy

with the layup angle  $\theta$ .

Let us consider the problem of predicting the necessary tensile strengths associated with the above models. For this purpose reference is made to Fig. 15 and the open triangles. The open triangle for "batch 6" at 0 deg. layup is based upon the premise that (in the absence of bond beams), the 0 deg. tensile strength is determined solely by the grout tensile strength and area; little or no tensile strength is attributed to the mortar bond - a fact which has been substantiated by joint tests. The resulting strength estimate is seen to be excellent. The reason? The "batch 6" specimens contained relatively few flaws in comparison to "batches 1 to 5"; this is reflected by a smaller data scatter for "batch 6" in Figs. 14, 15. What happens then if extensive flaws exist? The answer may be found in the data of another test series represented by Table 2. The specimens marked "STD" had extensive flaws while those denoted "STD VIB" had relatively few flaws. Based upon the grout core/panel area ratio, the correlation between component and panel 0 deg. tensile

Table 2. Tensile Strength Predictions\*

	STD	STD VIBR
$\frac{\text{Grout Area}}{\text{Panel Area}}$	0.54	0.54
$\frac{\text{Grout Tensile Strength}}{\text{Panel Tensile Strength}}$	0.34	0.50
$\frac{\text{Prism Tensile Strength}}{\text{Panel Tensile Strength}}$	1.06	.99

\* Entries represent means of multiple tests.

strength is observed to be excellent for the STD VIB specimens and poor for the STD specimens.

The bridge from component data to masonry strength in the presence of significant flaws necessitates a statistical analysis in conjunction with a considerable number of tests. Although this topic is extremely important, it is beyond the scope of this discussion. An explicit, dramatic if the flaw type and distribution is known, is worth noting at this point, however. Upon examination of the failure surface associated with a direct tensile test of a puddled prism with no admixture, the cross-hatched area of Fig. 16 was deduced to be free from flaws, i. e., the remaining area represented a flaw in which no bond existed across the plane of failure. The ratio of the area of flaw-free grout to the total grout area was .67. Based upon this ratio and the measured grout strength, the tensile strength of the prism was predicted within a few percent accuracy. Thus, there can be no doubt that flaws significantly influence strength.

The strength of a 90 deg. layup specimen in uniaxial tension is primarily a function of block strength. A typical failure pattern is illustrated in Fig. 17. The head joints contribute little to overall strength of a macroelement, and inspection of failed specimens revealed that most grout cores separated cleanly from the webs. Addition of the area of web that adhered to the grout core to the area of the face shells provides the estimate of macroelement strength at 90 deg. layup, shown as the open triangle in Fig. 15. The estimate is seen to be reasonable, and should not be significantly influenced by flaws. Block strength here was determined by direct tensile testing of coupons sawcut from full-blocks.

The prediction of macroelement compressive strength from component properties is not straightforward and this subject is currently

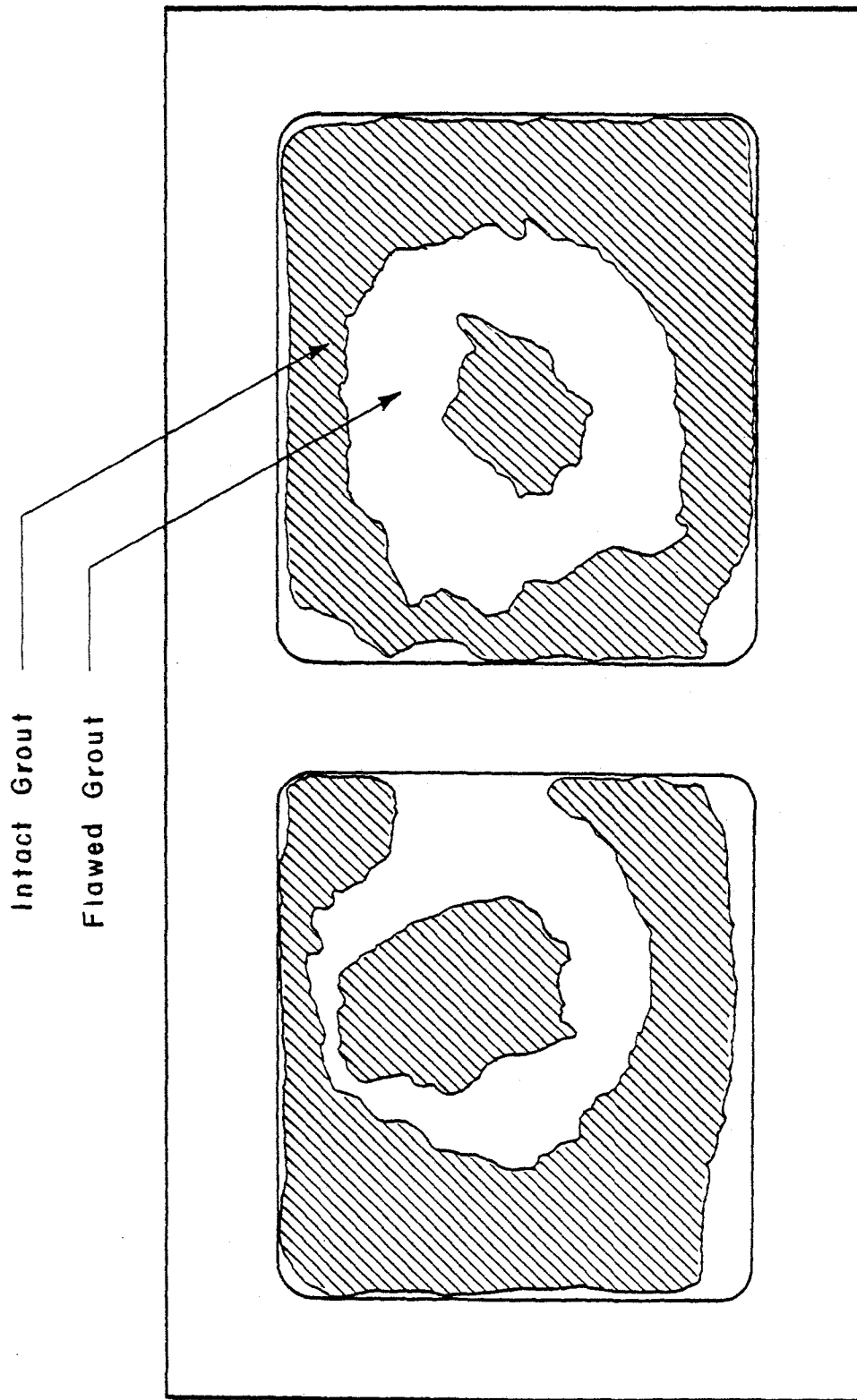


Fig. 16 Grout Flaws at Bed-Joint Plane

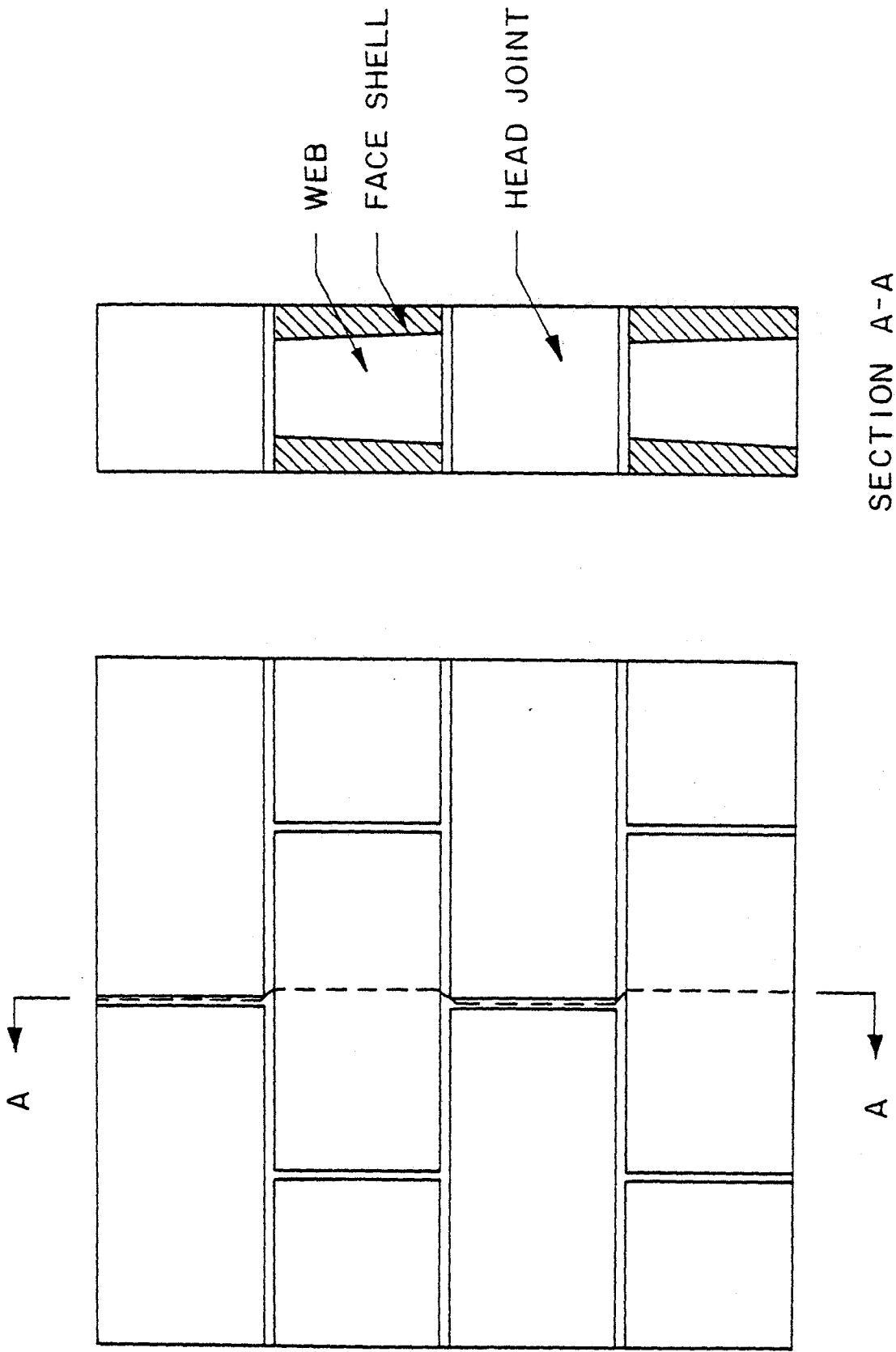


Fig. 17 Tensile Failure Pattern for 90° Lapup

under study.

Finally, the problem associated with flaw influence on 0 deg. uniaxial tensile or compressive strengths can be alleviated considerably by careful use of prism tests. In the case of tensile strength, three course prisms, fabricated and cured in the field using techniques that mirror (as close as is feasible) those of full-scale masonry have been found to provide good to excellent correlation with macroelement data; examples are included in Table 2 and Fig. 15 (the open square). The use of prism tests for compressive strength requires extreme care; discussion of this subject is contained in a later section.

#### 8.4 Influence of Reinforcing Steel on Initial and Post Macrocracking Behavior

The influence of reinforcing steel on the extent of macrocracking, and on the nonlinear post-macrocracking stress-strain response, is of major concern in our studies. Current reinforced specimens are fully grouted with two number five bars (grade 60) at approximately 32 inches on center - both vertically and horizontally. The steel area in each direction is  $0.6 \text{ in}^2$ , whereas the net cross-sectional panel area is  $488 \text{ in}^2$ ; this gives a steel/masonry area ratio of .00126 in each direction, which exceeds minimum UBC requirements.

Tests of reinforced specimens required a more complex fixture design than that associated with unreinforced tests (see Fig. 3); a schematic for a typical 20 deg. layup is shown in Fig. 18. Note that the steel is welded to a steel plate on the "tensile" edge of the biaxial test; the plate is, in turn, hard bonded to the load distribution fixture; a soft bond is utilized on the "compression" edge. Specimen fixtures were designed to provide a uniform (tensile) strain field in both steel and masonry prior to macrocracking. Displacement (or strain) control was employed on the

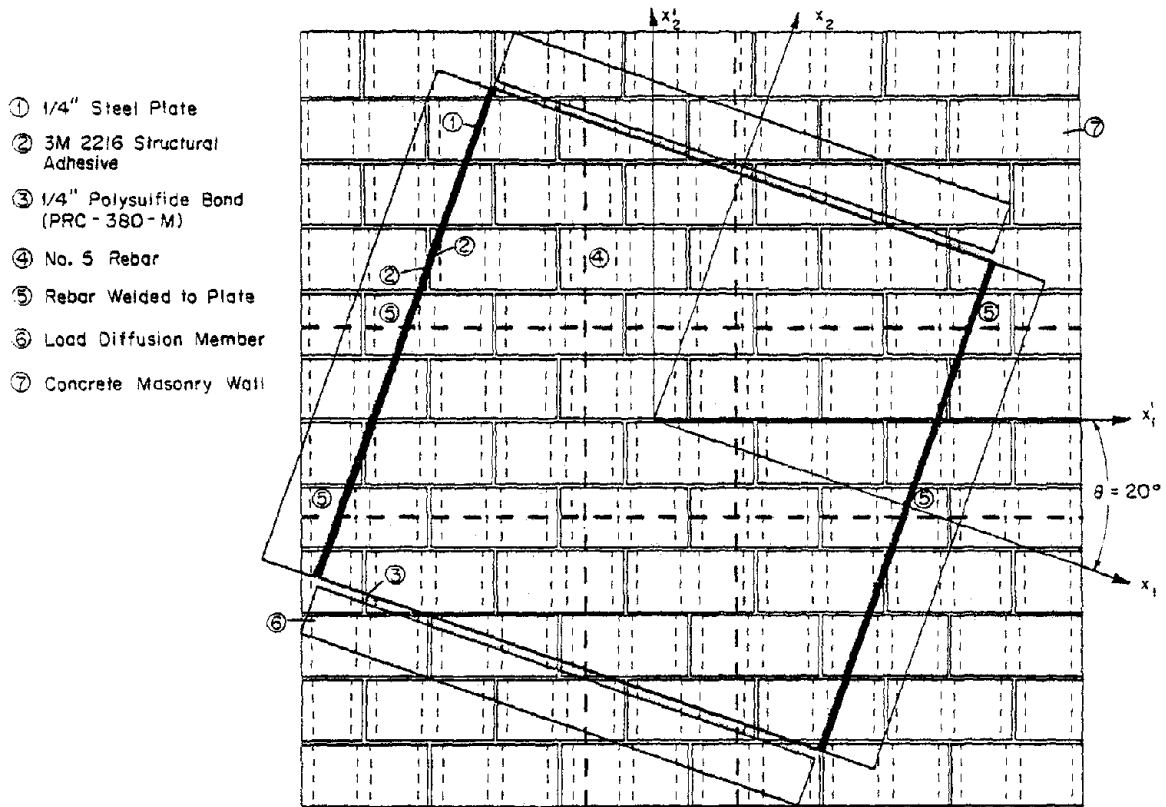


Fig. 18 Fixture Details for Reinforced Specimens

"tensile" edge via the use of LVDT's; loads on the "compressive" edge were adjusted for proportional loading by measurement of average tensile loads using load cells and appropriately modifying the signals to the compressive actuators (servo valves).

Several important aspects of the reinforced tests are noted here. First, as was previously indicated, the initial macrocracking stress surface is not significantly influenced by steel/masonry area ratios of .00126 or less. Thus, failure envelopes, Fig. 10, as determined from unreinforced tests should predict the onset of major cracking. A typical comparison of unreinforced results is given in Table 3.

Table 3. Comparison of Fully Grouted Reinforced and Unreinforced Panel Homogeneous Failure Stresses (psi) for  $\sigma'_{11} = 0$

$\theta$ (deg.)	Unreinforced		Reinforced	
	$\sigma'_{12}$	$\sigma'_{22}$	$\sigma'_{12}$	$\sigma'_{22}$
0	0	77.5	0	88.3
	0	66.4	0	99.1
avg.	0	72.0	0	89.7
20	130	-310	162	-382
	144	-343	175	-419
avg.	137	-327	169	-401

Second, while the above steel/masonry area ratios do not significantly influence the onset of cracking, they most certainly have a dramatic influence on crack distribution and on the individual crack size (opening).

Whereas single cracks were observed in unreinforced specimens for  $|\theta| > 15$  deg., multiple or distributed cracks were observed in all reinforced tests. Comparative examples of reinforced vs. unreinforced fracture modes may be found in Figs. 19-22. The domain of cracking was found to increase with an increase in the magnitude of the principal compressive stress, i. e., as  $|\theta|$  decreased in the proportional loading tests.

Third, steel/masonry area ratios of the order of .00126 or less are not sufficient to prevent an unstable branch of the stress-strain curve associated with the principal stress direction perpendicular to the crack(s) plane(s). Typical such curves are shown for 0 deg. and 20 deg. specimens in Figs. 23 (a, b) and 24 (a, b) respectively, for both monotonically increasing and cyclic (tensile) strains. The associated macroelement tensile stress drop is observed to be dramatic for the uniaxial case (0 deg.) and the materials used; the magnitude of this drop, given the above steel area, will increase with an increase in grout tensile strength. The magnitude of the drop is less for specimens in the 15 to 20 deg. range since the compressive principal stress lowers the tensile principal stress at initial macrocracking (see Fig. 14). The strain interval over which the slope of the stress strain curve is negative (approximately .01 percent) represents a decrease in load carrying capability of the element. This reduction is attributed to 1) a load transfer from masonry to steel and 2) the fact that the steel area is not sufficient to maintain the original load without considerable extension.

Fourth, upon continued monotonic straining of the specimens, re-loading is observed, the slope of which is less than that of the masonry but larger than that of the steel alone. This slope is monotonically decreasing. The stress level of initial macrofracture may or may not be reached again depending upon the steel area, the steel yield stress, and the biaxial stress-state at initial macrofracture.

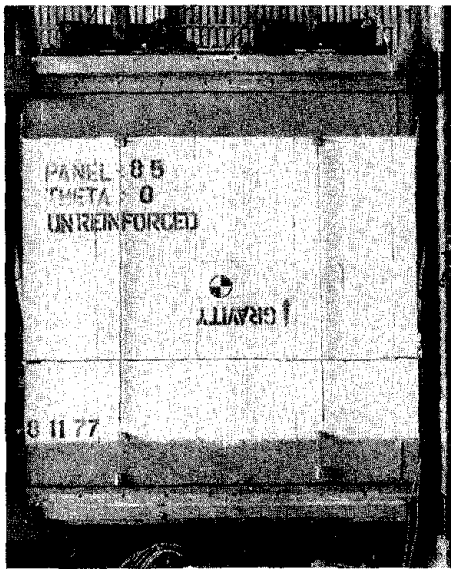


Fig. 19 0° Unreinforced

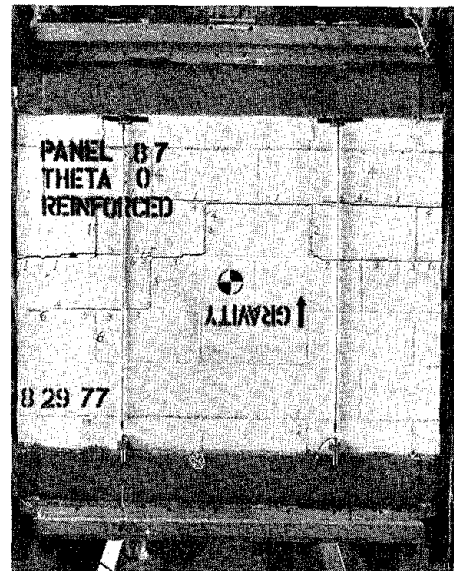


Fig. 20 0° Reinforced

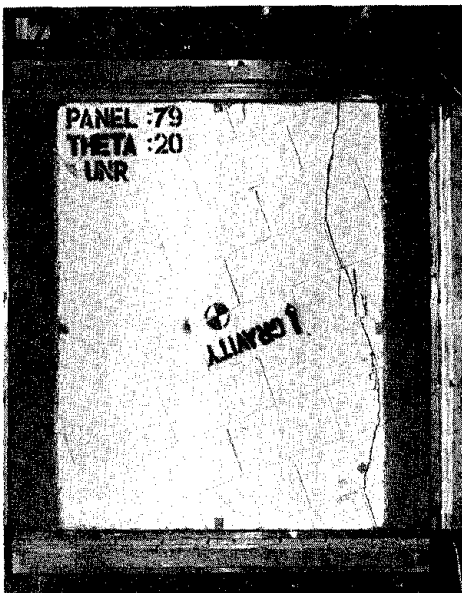


Fig. 21 20° Unreinforced

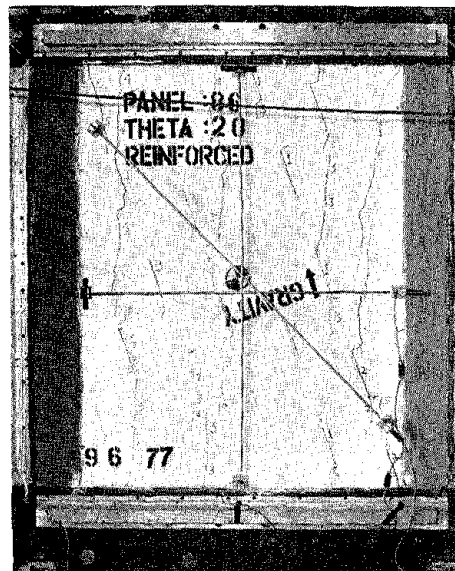
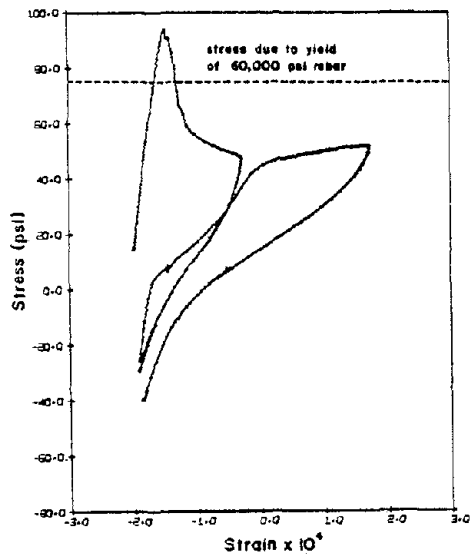
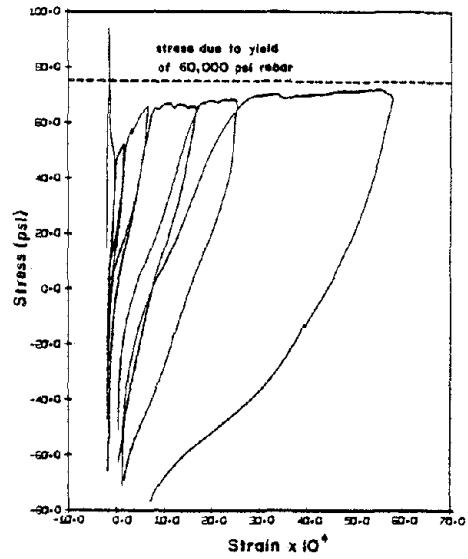


Fig. 22 20° Reinforced

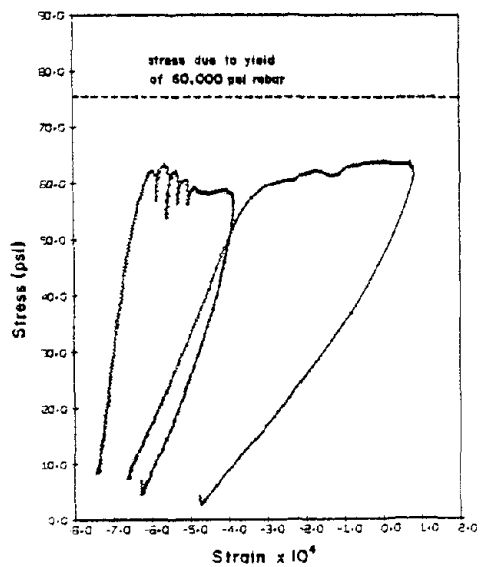


(a)

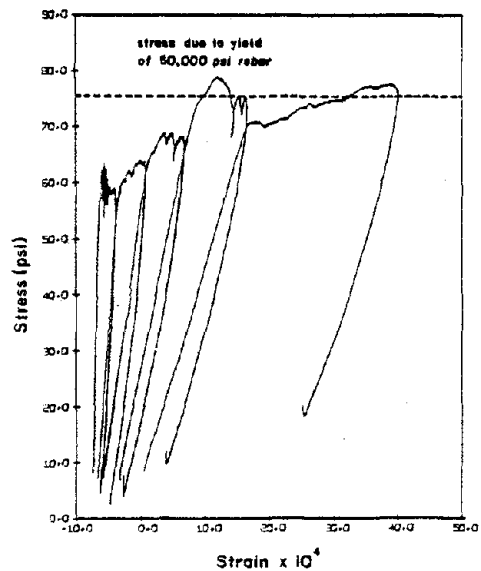


(b)

Fig. 23 0° Reinforced Stress-Strain Curves



(a)



(b)

Fig. 24 20° Reinforced Stress-Strain Curves

Finally, upon cyclic straining from zero to a tensile strain, stiffness degradation can be observed, Figs. 23 (a,b), 24 (a,b). The degradation is accompanied by an increase in crack density and crack domain for each cycle.

### 8.5 Elastic Moduli and Anisotropy

Data on stiffness parameters is essential to both design and analysis of concrete masonry systems. Several important items in this area concern the elastic moduli at low stress levels, the degree of anisotropy of the above, and the ratio of Young's modulus to  $f'_m$  (compressive strength).

Typical variations of Young's modulus and Poisson's ratio with  $\theta$  for the material discussed above are illustrated in Figs. 25, 26. This data was obtained by uniaxial compression tests in the range 0-300 psi. A linear regression analysis of the data reveals a trend in which both moduli decrease from  $\theta = 0$  deg. (compression across bed joint planes) to  $\theta = 90$  deg. (compression across head joint planes). Since most specimens provide two data points (by reversing the roles of the principal stresses), one may observe this trend in the absence of data scatter by following the same specimen number in Fig. 25. Compare, for example,  $\theta = 15$  deg. with  $\theta = 75$  deg. for specimens 19, 20, or 25 in Fig. 25, or compare  $\theta = 30$  deg. with  $\theta = 60$  deg. for specimen 32. Note that, while the data exhibits anisotropy, the materials under discussion may be approximated as isotropic within the data scatter observed.

### 8.6 Elastic Moduli and Compressive Strength

Typical data (means of multiple tests) concerning the ratio of Young's modulus to  $f'_m$  is shown in Table 4. The elastic modulus was

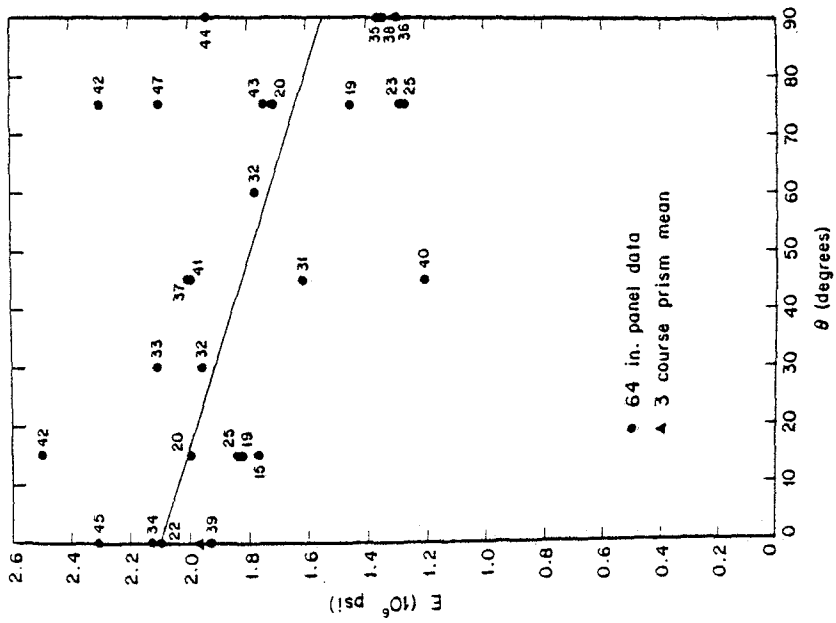


Fig. 25 Panel Stiffness Anisotropy

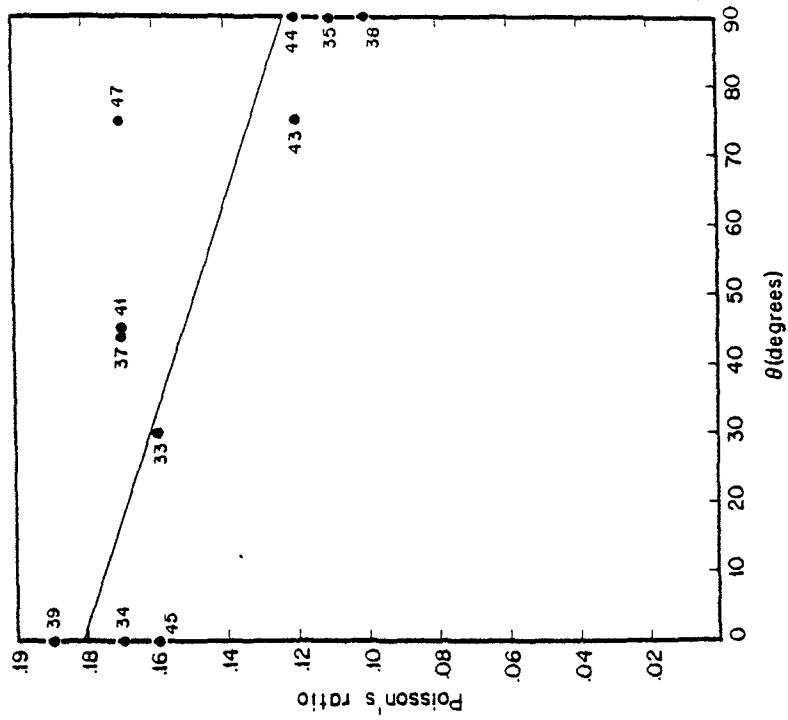


Fig. 26 Panel Poisson's Ratio Anisotropy

computed from panel data in the 20 to 145 psi compressive stress range, and is in good agreement with data from five course prisms in a similar stress regime. The values of  $f'_m$  employed were obtained from five course prisms laid in stack bond. The ratio of elastic modulus to  $f'_m$  is in good agreement with the UBC (Table No. 24-H, 1976 version; special inspection column) in which the number 1000 is assumed.

Table 4. Ratio of Elastic Modulus to  $f'_m$

	STD	STD VIB	ADM	ADM VIB
<u>Elastic Modulus</u> $f'_m$	1129	1081	1192	1028
Standard Deviation	241	102	126	93

### 8.7 Damping and Strain-Rate Effects

Figure 27 shows typical compressive cyclic stress-strain data (same specimen) ranging from a slight prestress to approximately 150 psi for five strain rates from .05 Hz to 2.0 Hz. Each figure depicts two cycles. Several extremely important observations regarding material behavior can be extracted from this data, which is typical.

First, the data clearly exhibits little or no strain-rate dependence over frequencies extending from essentially quasi-static to typical expected mode frequencies for full-scale structures. Both slopes and hysteresis loops remain invariant with frequency in the above range.

Second, the hysteresis loops provide a measure of energy absorption or damping in the "linear elastic" regime. The fact that the areas of

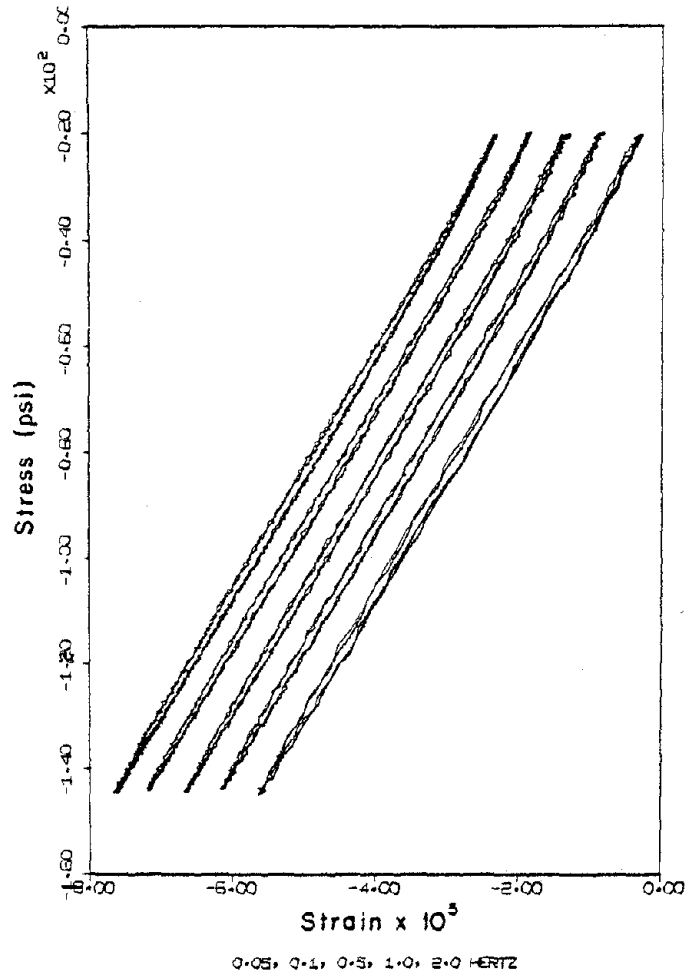


Fig. 27 Typical Panel Compressive Cyclic Data

these loops are not a function of frequency implies that material damping should not be modeled as viscous damping.

The implications of the above observations may be considerable. For example, the current response spectrum<sup>(7)</sup> approach to the seismic design of buildings is based upon the premise that the damping involved is of the viscous type. If the damping associated with a complete structure is primarily the result of material behavior, then this premise is suspect in view of our findings. This potential problem is compounded by the fact that the response spectrum is highly sensitive to the damping assumed.

One may argue here that the first mode (or the first few modes) of a building performs as a narrow-band filter, and hence that one may approximate the structural damping mechanism as viscous wherein the damping factor is determined from data (logarithmic decrement) in the neighborhood of the modal frequency of interest. This approximation may suffice if conducted properly. Unfortunately, it does not appear that this has been the case in practice.

Consider, for example, the percent critical damping factors claimed in some masonry promotional literature<sup>(8)</sup>. Values ranging from 8 to 10 percent have been proposed for some masonry materials. Such information has evolved from the measurement of the rate of decay (logarithmic decrement) of material response to a transient blow from a hammer (in-plane), a steel-ball-pendulum impact<sup>(8)</sup> (out-of-plane), etc. Two things are wrong here. First, the response frequencies associated with such tests are too high - by several orders of magnitude in some cases; this results in artificially high damping coefficients (damping is certain to be frequency dependent for sufficiently large frequencies). Second, and more important, the concept of critical damping has been incorrectly used. The latter is based upon the response of a single degree of freedom oscillator; the percent critical damping calculation necessitates

a knowledge of the mass and frequency of this oscillator. If the oscillator is to be associated, e. g., with the first mode of vibration of a building, then the effective mass and frequency must correspond to this mode. That is, the percent critical damping is a function of the assumed mass and the modal frequency.

It is of interest to estimate how far off the above mentioned 8 to 10 percent critical damping factors are - based upon the assumption that such numbers originate from the concrete masonry and not from connections or non-structural elements. Consider Fig. 27. If the damping is sufficiently small, the transient response to an initial value problem will be nearly harmonic. Suppose, as the data indicates, that material damping is independent of frequency. As in the case for viscous damping, the rate of decay curve is exponential and the decrement is a constant. The decrement for a macroelement can be calculated from Fig. 27 by measuring the areas representing hysteresis and strain energy, and by computing the loss of strain energy per cycle. If this quantity does not depend on stress amplitude, then the decrement for a macroelement is the same as the decrement for a full-scale structure composed of the same material, i. e., the energies of the subcomponents can be summed to yield the energies of the structure. Thus, one may now speak of a structural mode of vibration. The results? Critical damping factors of less than 2 percent are observed when the measured decrement is applied to an "equivalent" viscous model. Thus, if 8-10 percent critical damping factors are to be employed in practice for concrete masonry structures, such high values must be the result of connection behavior, or some other aspect of the structure.

The foregoing discussion concerned low stress amplitudes, e. g., material response in the essentially linearly elastic range. Energy absorption and strain-rate dependence in the high stress range is also under study, but will not be discussed herein.

## 8.8 Influence of Flaws, Compaction, Admixtures

Specimen sawcutting has afforded an unusual opportunity to observe flaws in concrete masonry. Such cuts provide more information than cores, although cores are also taken in our test program.

To date over ninety panels have been tested. The vast majority of these specimens have exhibited flaws in the form of grout-block separation, mortar-block separation, voids, and shrinkage cracks forming grout bridges. Figure 28(a) shows typical grout-block separation. Figure 28(b) exhibits both grout-block and mortar-block separation as well as grout bridges. Figure 28(c) dramatically illustrates these flaws and the fact that they can prematurely trigger failure.

Block-grout separation occurs frequently in the field, Figs. 28(d, e), following seismic excitation; it is considered to be a serious problem. This matter is under investigation from several viewpoints. These include a study of mold release agents that are sometimes used in the manufacture of concrete block and which may adversely influence the bond, and a study of expansive grout admixtures.

In an effort to understand, and to mitigate the grout shrinkage problem, several grouting techniques have been explored. These, together with identification for subsequent discussion, include: 1) puddled grout (marked STD); 2) vibrated grout (marked STD VIB); 3) puddled grout with an admixture (Suconem GA or Grout Aid; marked ADM); and vibrated grout with an admixture (Grout Aid; marked ADM VIBR). The component properties for these tests are given in Table 5.

Figures 29 (a, b) illustrate the influence of each technique on full-scale panels sawcut from 8 by 8-foot fully grouted walls. It can be observed that vibration compaction yields a specimen superior to puddling with or without the admixture.

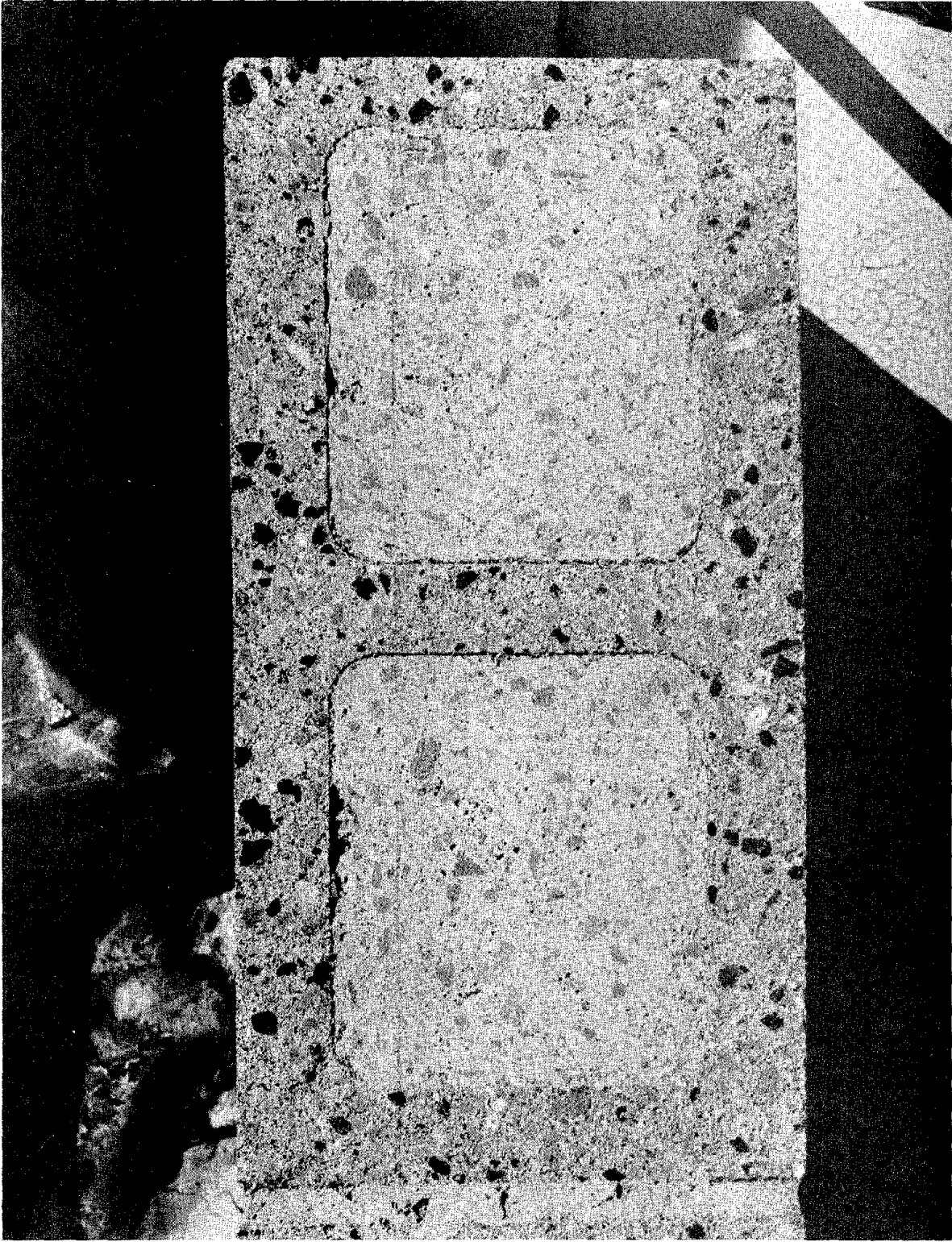


Fig. 28 (a) Typical Grout-Block Separation



Fig. 28 (b) Grout-Block and Mortar-Block Separation (Oblique Cut)

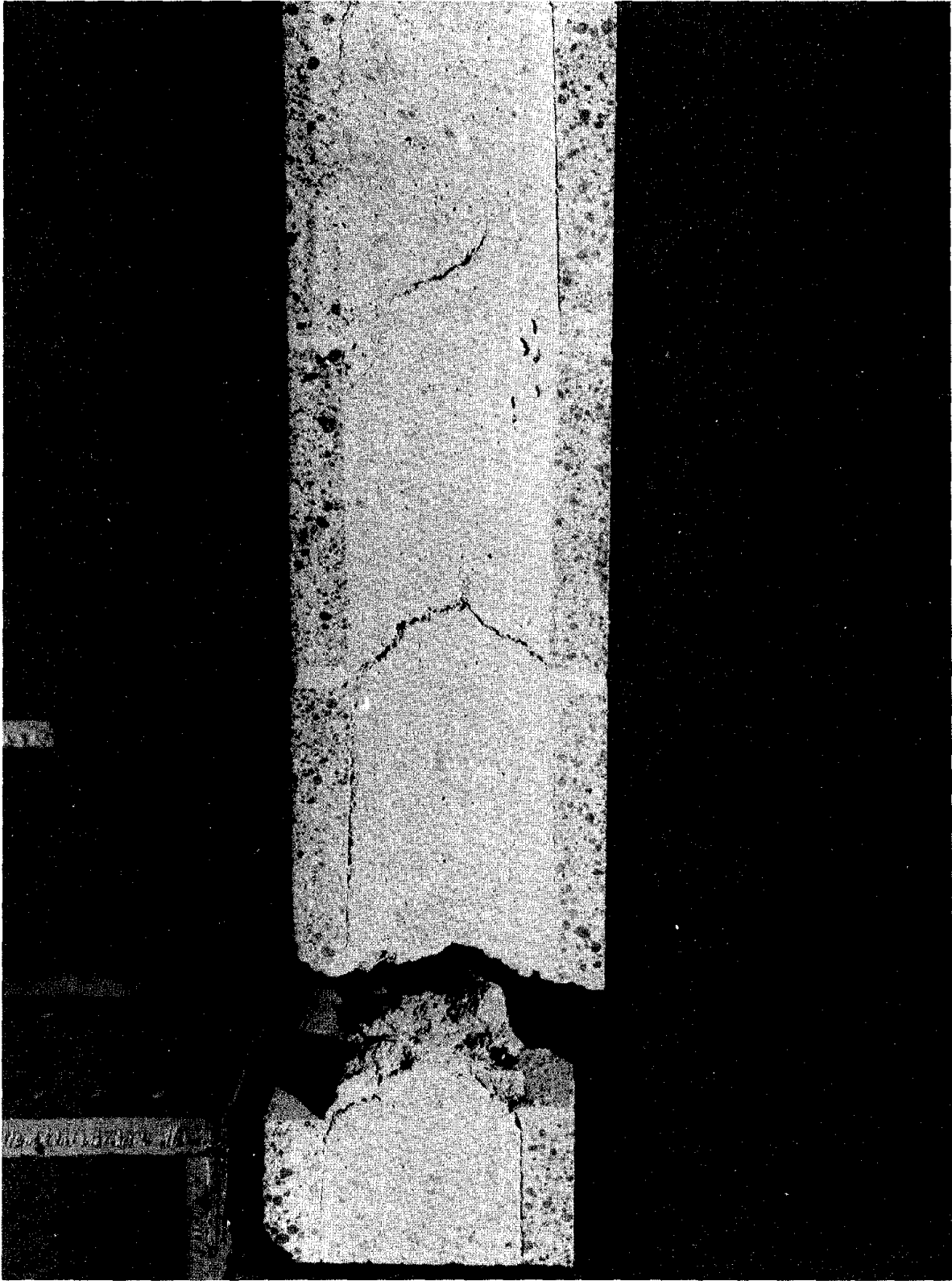


Fig. 28 (c) Grout Bridges and Resulting Failure

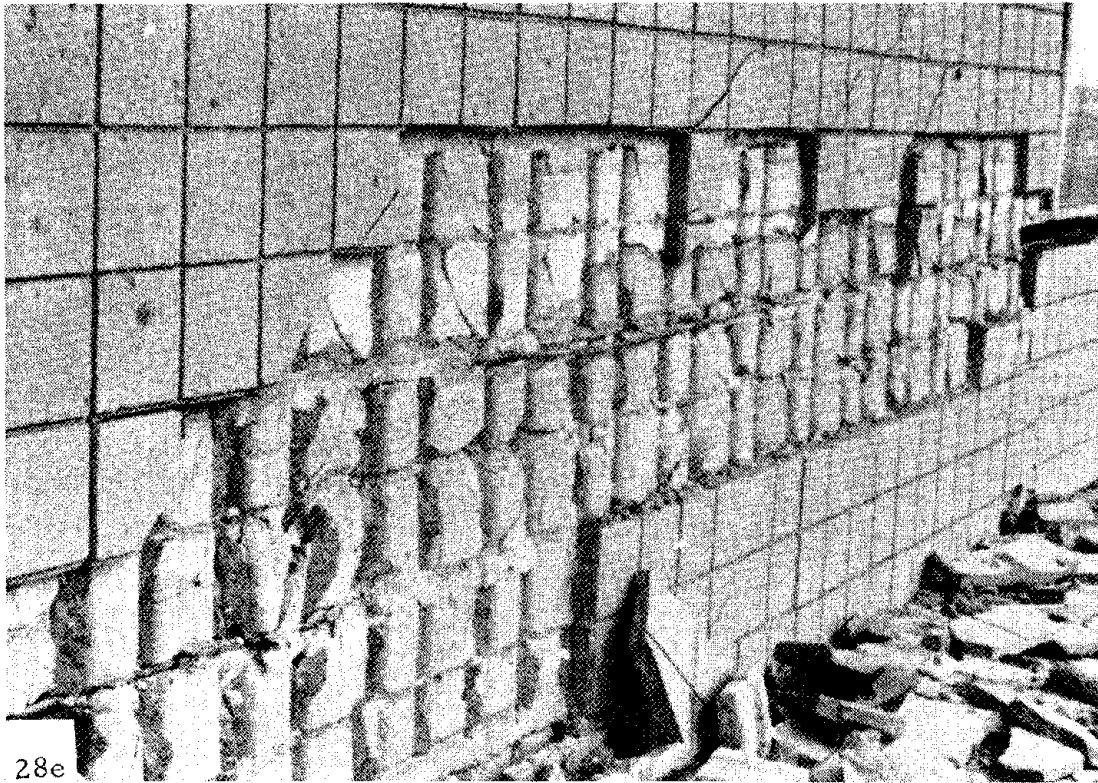


Fig. 28 (d) Block-Grout Separation

Fig. 23 (e) Face-Shell Spallation

Table 5. Component Properties for Admixture Tests

	Block <sup>†</sup>	Mortar	Grout <sup>‡</sup>	
			STD	ADM
Compressive Strength (ksi)	3.55	2.40	2.90	3.49
	3.12	2.24	2.28	2.46
	3.35	1.96	2.53	3.49
	3.54	1.89	2.43	4.03
	3.63	1.50	2.33	2.42
	3.80	2.52		
	3.66	1.41		
	3.98			
mean	3.58	1.99	2.49	3.18
std. dev.	.26	.43	.25	.71
Tensile Strength (psi)	432	201	219	284
	420	27	250	283
	331	37	223	283
	314	111	228	390
	368	3		397
		142		
		177		
		167		
mean	373	108	230	327
std. dev.	52	76	14	60
Young's Modulus, Compression (psi)	$2.5 \times 10^6$ (2.2-2.8)		$2.6 \times 10^6$ (2.5-2.7)	
Young's Modulus, Tension (psi)			$2.3 \times 10^6$ (2.1-2.5)	
Poisson's Ratio	.16 (.14-.18)			.16

<sup>†</sup> Block: Type N, ASTM C90 Block; test coupon approx. 4.0" x 6.5" cut from face shells.

<sup>‡</sup> Grout: Coarse grout, ASTM C476 (6-sack grout).

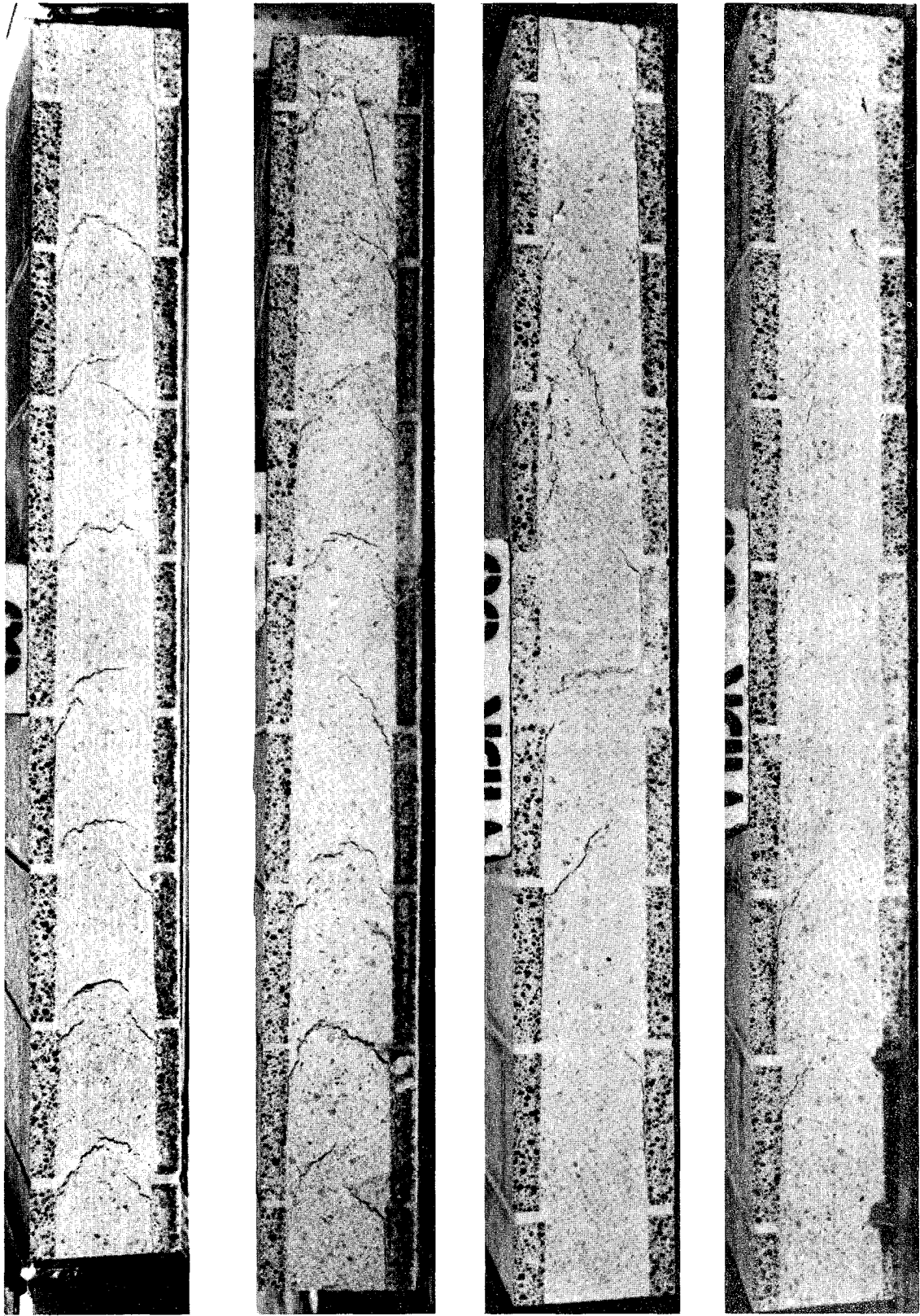


Fig. 29 (a) Sides of Panels: Puddled; Admixture Puddled; Vibrated; Admixture Vibrated (shown in order from top to bottom)

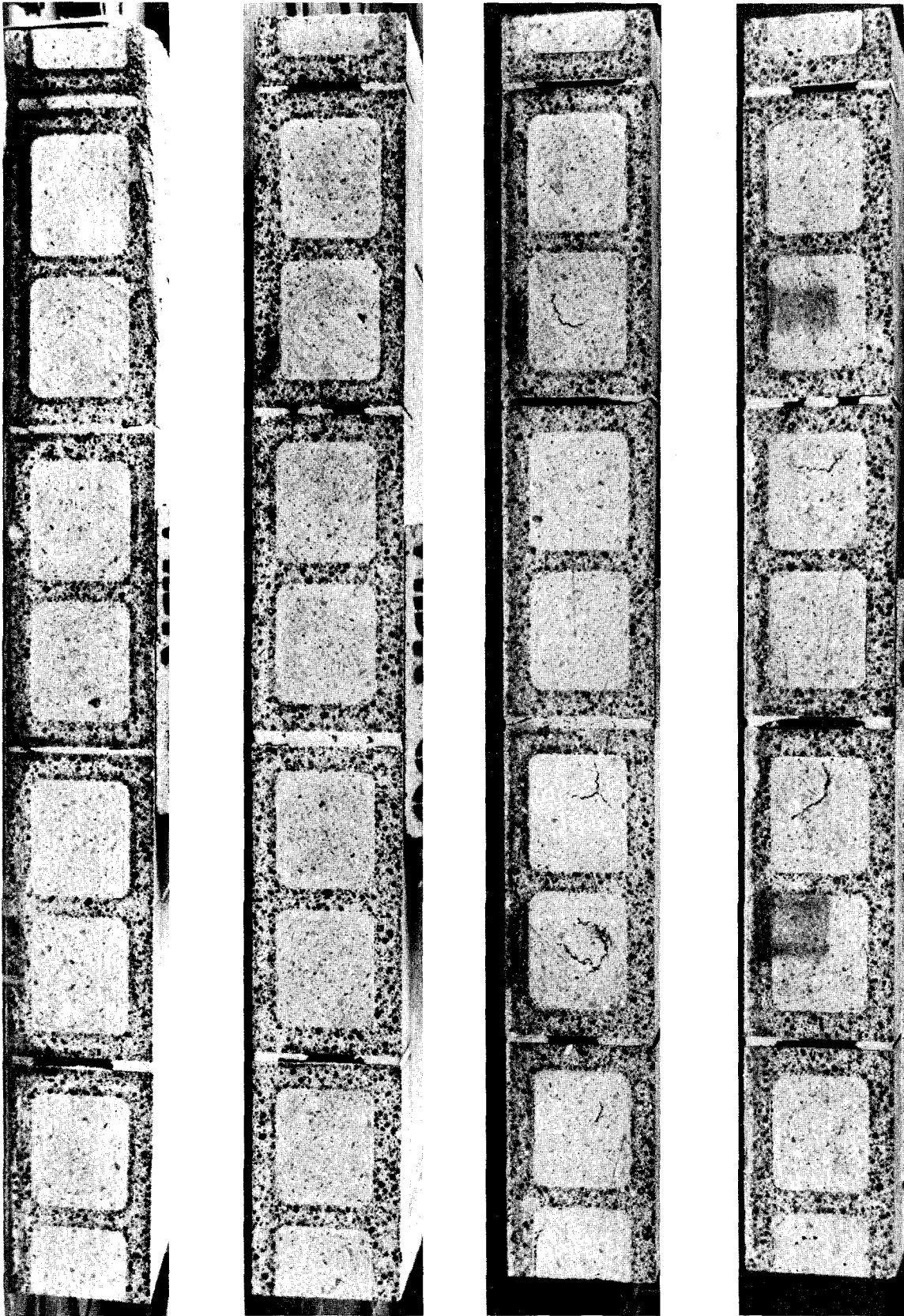


Fig. 29 (b) Tops of Panels: Puddled; Admixture Puddled; Vibrated; Admixture Vibrated (shown in order from top to bottom)

The influence of grout vibration compaction on masonry strength is remarkable. Tables 6 and 7 reveal that vibrated specimens provide a substantial strength increase over puddled specimens - again, with or without the admixture. The admixture studied had little or no influence on tensile strength, but provided a moderate increase on compressive strength.

On the basis of our tests, it is recommended that grouted masonry be compacted by vibration rather than by puddling.

### 8.9 Finite Element Predictions (Micromodeling)

It was noted previously that a relatively elementary analytical model will suffice to predict initial macrocracking. In more complex situations involving nonhomogeneous stress fields with large stress gradients and complex deformation fields, a more detailed analysis may be necessary. It is for this reason that the micromodeling is being pursued in parallel with the development of a continuum theory of concrete masonry. Finite element simulation of panel behavior has been performed to assess the accuracy of current micromodeling concepts. For this purpose the panel assembly is discretized into a system of plane stress finite elements. The masonry joints are represented by a newly developed interface method<sup>(9)</sup>. Interface properties are determined from joint tests discussed in a subsequent section. A typical fracture pattern for a 45 deg. uniaxial case (unreinforced) is shown in Fig. 30 (a). The results of analyses performed to date, which were obtained by using an out-of-core version of NONSAP, show excellent correlation with experimental data; for example, the ultimate strength of the model shown in Fig. 30 (a) was approximately 77 psi, compared to 80 psi obtained experimentally. Agreement with respect to failure mode was also excellent as is indicated by Fig. 30 (b).

Table 6. Tensile Failure Strength for Unreinforced Grouted Panels

	STD	STD VIBR	ADM	ADM VIBR
Failure Stress $f'_{mt}$ (psi)	90.0	129.5	67.1	125.2
	79.7	96.7	111.9	119.5
	99.1	118.3	97.1	101.8
mean	89.6	114.8	92.0	115.5
std. dev.	9.7	16.7	22.8	12.2

Table 7. Compressive Strength for 4-Course Grouted Prisms

	STD	STD VIBR	ADM	ADM VIBR
Failure Stress $f'_m$ (psi)	2140	2123	1685	2359
	1702	2140	1735	2584
	2079	2241	1574	2595
	2072		1735	2746
	1928		1634	2544
mean	1984	2171	1673	2566
std. dev.	212	142	96	173

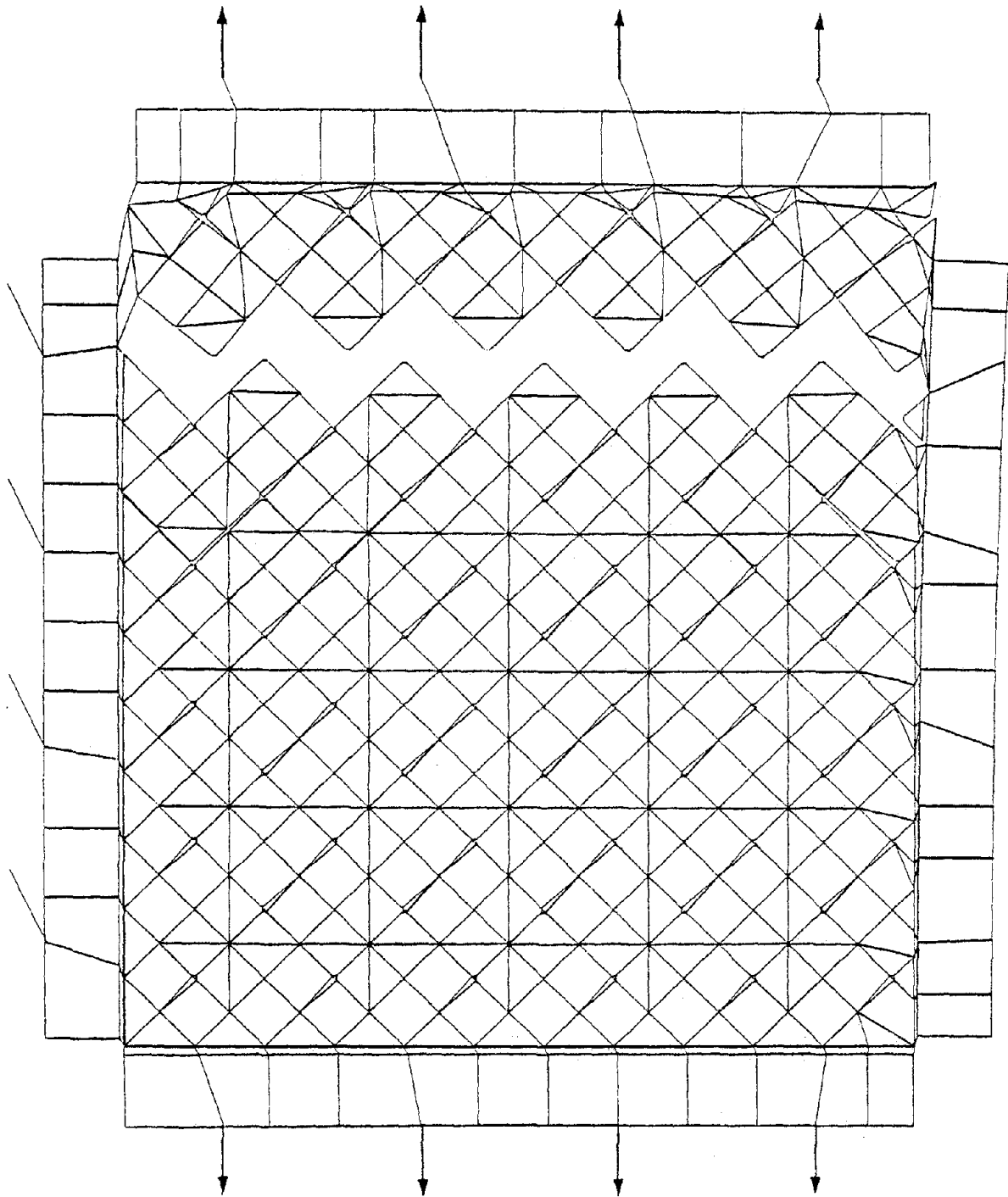


Fig. 30 (a) Finite Element Prediction of Failure

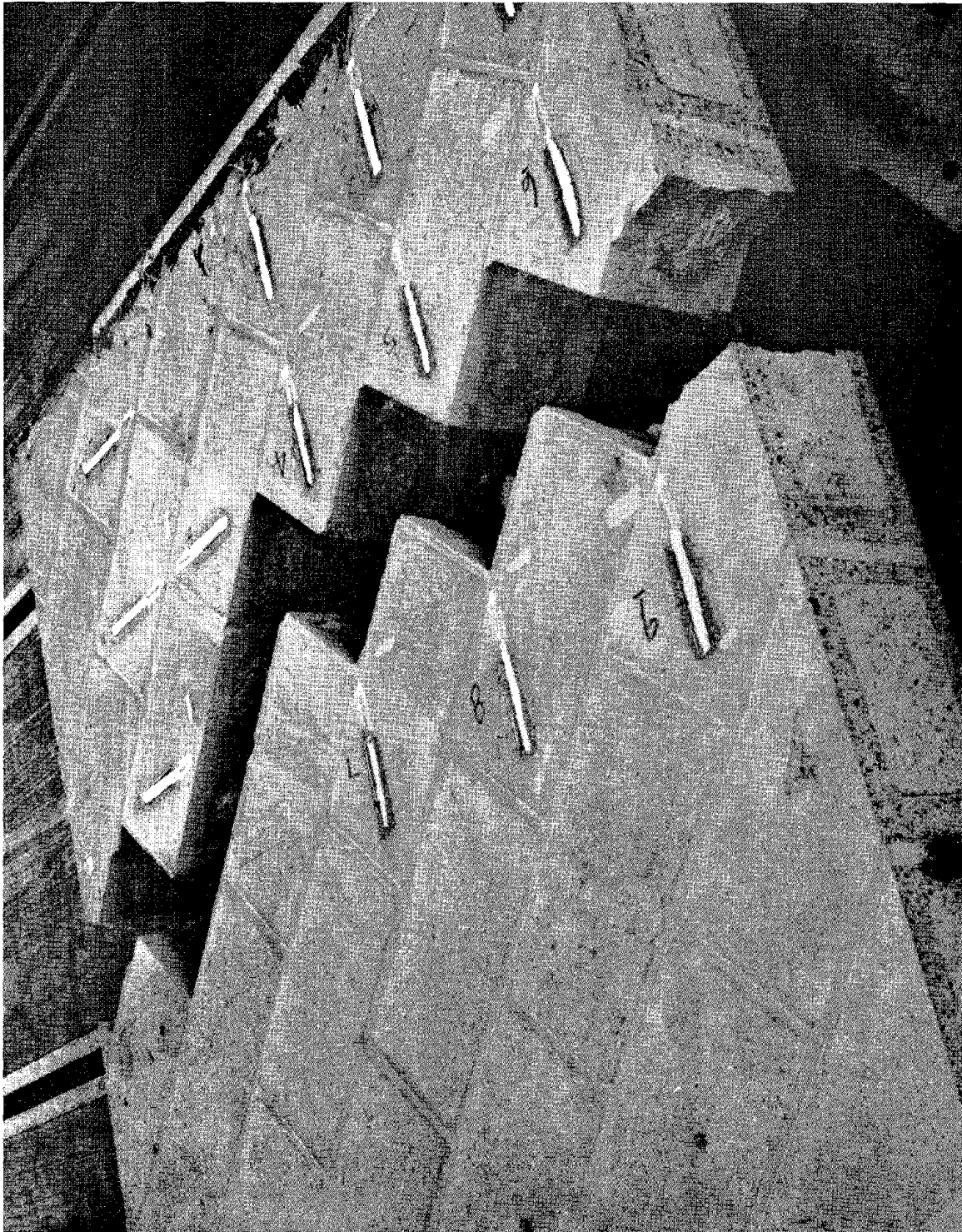


Fig. 30 (b) Typical Failure of An Unreinforced Panel

## 9. SELECTED RESULTS - PANELS (MACROELEMENTS ) UNDER NONHOMOGENEOUS STRESS STATES

Brief discussions of several salient results and important features of the nonhomogeneous stress state test-series are presented below. Primary emphasis is placed on the use of data from the homogeneous stress-state tests to predict 1) the failure load associated with the diagonal compression tests and 2) the nonlinear response of shear walls under both monotonic and cyclic loading.

### 9.1 Diagonal Compression

The diagonal compression test is conducted on square, 64 by 64-inch, unreinforced but fully grouted masonry specimens, to which compressive loads are applied at two opposite corners (see Figs. 7, 8). The loads are applied through steel caps which extend along the panel edges approximately 10 inches from the corners. A layer of hydrocal is employed between the caps and the panel. The displacement of the cap is increased until fracture occurs. A typical failed specimen is shown in Fig. 31.

The diagonal compression test closely approximates a plane stress boundary value problem for which an analytical solution is available<sup>(1)</sup> (see Fig. 8) for the stress field. Here the loads are taken as point loads and the material is assumed to be homogeneous, isotropic, and linearly elastic; the resulting stress field is independent of the material elastic constants. Examination of this solution reveals that fracture will occur at the panel center. The analytically predicted principal stresses at this point are

$$\sigma_1 = 733.6 \bar{\tau} \quad , \quad \sigma_2 = - 2380 \bar{\tau} \quad , \quad \bar{\tau} = 0.707 P_d / at \quad (5)$$

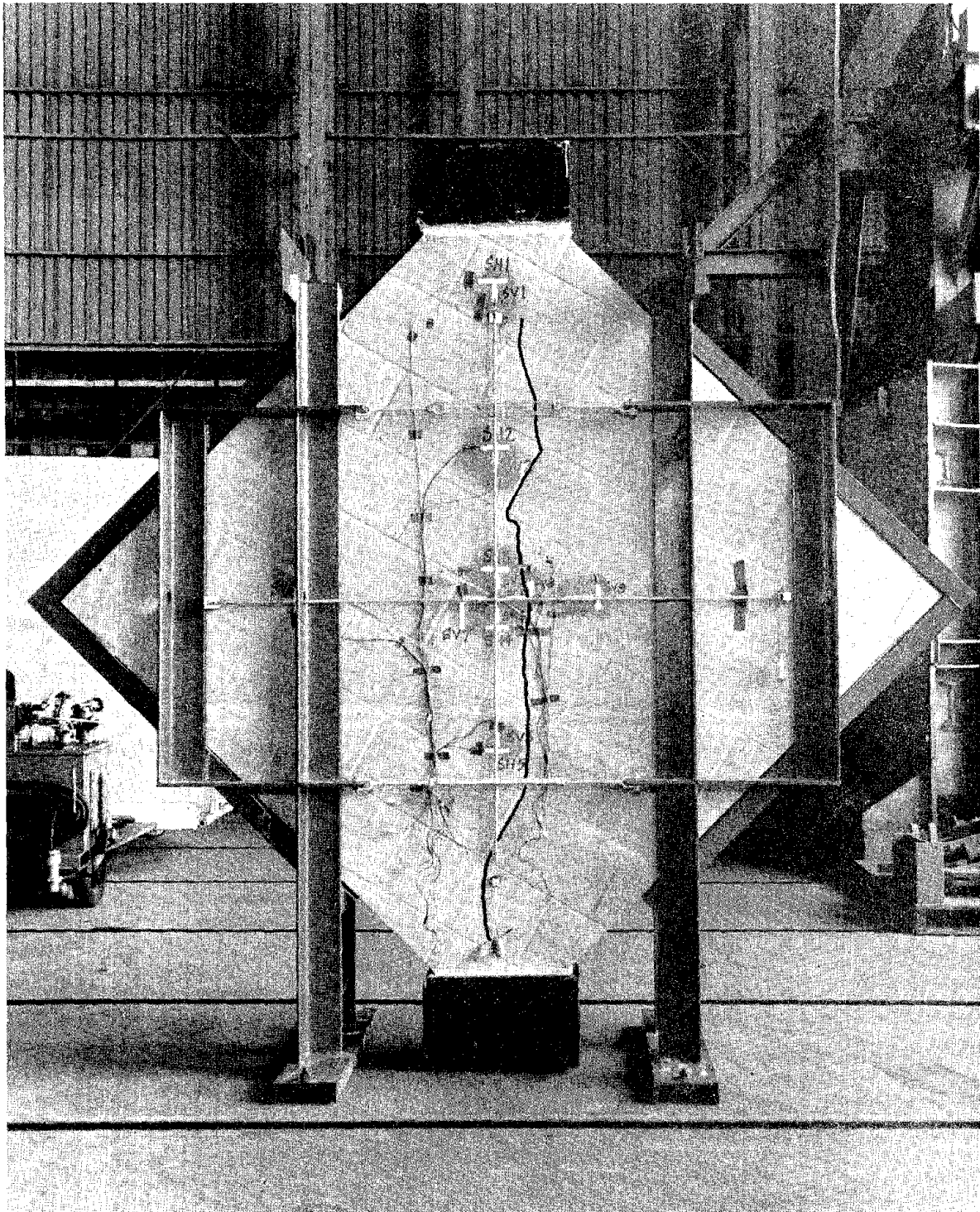


Fig 31 Typical Diagonal Compression Failure

where  $a$ ,  $t$ ,  $P_d$  denote panel edge length, panel thickness and applied diagonal load, respectively. Corrections to this stress field for the actual test boundary conditions were determined via a finite element analysis; it was found that

$$\sigma_1 = 633 \bar{\tau} \quad , \quad \sigma_2 = - 2186 \bar{\tau} \quad (6)$$

at the panel center.

In order to predict, from homogeneous biaxial tests, the load  $P_d$  at which fracture occurs in the diagonal compression test, one needs the results of a test for which the principal stresses are in the same ratio as those of equation (6), namely -3.45. Since homogeneous data was available for a ratio of -3.00 and a layup angle of 30 deg. relative to the principal stresses, a layup angle of 30 deg. was selected for the diagonal compression tests; the specimen(s) were of the same "batch" as the homogeneous tests. The load  $P_d$  was predicted by correcting the principal stress ratio by application of the model discussed previously, in which there is a linear decrease in tensile strength ( $\sigma_1$ ) with an increase in compressive stress ( $\sigma_2$ ) (see Fig. 13).

Three diagonal compression tests were conducted. The last two specimens were from a different batch than the first specimen, and for this batch strengths were generally lower, and some data scatter was observed. For each batch two homogeneous biaxial tests with a ratio of -3.00 were conducted. The predicted values and results of the tests are given in Table 8. The agreement is good, and it indicates that the biaxial data may be applicable even for cases in which the characteristic length associated with a nonhomogeneous stress field is of the same order as the block dimensions.

Table 8. Diagonal Compression Test Peak Loads (kips)

Values Predicted from Biaxial Tests	105.9	78.2
Results of Diagonal Tests	107.3	83.4 89.7

Table 9. Shear Wall Prism Data

	Reinforced Monotonic	Unreinforced Monotonic	Reinforced Cyclic
Compressive Strength (psi)	2414	2414	1833
Young's Modulus (psi)	$.8 \times 10^6$	$.8 \times 10^6$	$.8 \times 10^6$
Poisson's Ratio	.18	.18	.18

Table 10. Shear Wall Component Data (psi)

	Reinforced Monotonic	Unreinforced Monotonic	Reinforced Cyclic
Grout Compr. Strength	4225	4225	4020
Mortar Compr. Strength	3840	3840	2965
Block Compr. Strength	1800	1800	1800
Block Tensile Strength	293	293	293

## 9.2 Simple Shear Deformations

The purpose of the experimental vs. theoretical comparisons presented below is twofold: 1) to illustrate the ability of our micromodeling procedure to simulate the basic features of a highly complex process associated with shear wall deformations in the nonlinear regime of material response and 2) to note the ability of an elementary macromodel to predict the initiation of macrocracking in shear walls.

Data for the experimental portion of the comparisons was obtained from the U. C. Berkeley shear wall/pier test program. The specimens selected for study were 48 inches wide and 56 inches high, with top and bottom bond beams (72 inches high including bond beams). A schematic of the test setup is given in Fig. 9 (b). Initial vertical preload is applied to the specimen by springs; horizontal loads or displacements are applied by dual actuators which, in turn, are part of a MTS closed loop hydraulic servo system. The top and bottom surfaces of the bond beams are "rigidly" attached to steel beams by means of connectors embedded in the bond beams. The (passive) vertical columns serve to prevent relative rotation of the top surface with respect to the floor-plane.

Three test-types were selected for discussion. They include: 1) monotonic loading of an unreinforced specimen; 2) monotonic loading of a reinforced specimen; and 3) cyclic loading of a reinforced specimen. The reinforced shear wall had two No. 5 bars (grade 60) placed vertically in the end grout cores. Both unreinforced and reinforced specimens were fully grouted; mortar bedding was face shell only. Prism and component data for the test walls are given in Tables 9, 10.

### 9.2.1 Micromodel

Considerable progress has been made to date under this research program with respect to the development of a finite element micromodel of concrete masonry. In particular, a method<sup>(9)</sup> for incorporating the pre- and post-fracture behavior of joints (in a concrete masonry assemblage) in a finite element analysis has been developed, and a nonlinear material model<sup>(10)</sup> has been constructed which accounts for masonry cracking and the effects of reinforcing steel; both of the above have been implemented into an out-of-core version of the finite element program NONSAP.

The joint model utilizes a normal stress vs. shear stress (on the joint plane) failure envelope to define initial joint fracture; a Mohr-Coulomb type law governs post-fracture relative joint slip. A double nodding scheme is used in conjunction with the finite element analysis to describe joint slip, separation and recontact. Details concerning the joint model and the associated numerical algorithm can be found in Reference 9.

The material model assumes different forms for unreinforced and reinforced regions or elements. In an unreinforced element, the model is based upon the maximum tensile stress theory for cracking due to tension, and the von Mises yield surface in conjunction with a strain softening, unconstrained flow for failure in compression. Central to the model is the yield-fracture envelope shown in Fig. 13, which is a closed, convex curve in the principal stress space  $\sigma_1, \sigma_2$ ; this curve corresponds to the initial macrocracking envelope discussed previously, and quadrants 1, 2, 4 are determined accordingly; quadrant 3 is determined by intersecting the von Mises yield surface in the  $\sigma_1, \sigma_2, \sigma_3$  space with the plane  $\sigma_3 = 0$ . For stress paths originating and remaining interior to this

envelope, the masonry is linearly elastic; for any stress path intersecting the boundary in quadrants 1, 2, 4, cracking of the masonry occurs (assumed continuously distributed), the direction of which is normal to the maximum principal stress.<sup>†</sup> Upon subsequent straining the cracked masonry is considered continuous but orthotropic; the normal stress on planes parallel to cracks, and the associated tangent stiffness, are constrained to vanish; the tangent stiffness associated with the direction parallel to the crack remains unchanged; and the tangent shear modulus decreases with increasing crack opening in a manner reflecting aggregate interlock. If the strain history leads to crack closure, the material is allowed to partially or totally "heal". For a strain history leading to a stress point on the boundary in quadrant 3, crushing of the masonry commences; a flow law relating the octahedral shear strain to the octahedral shear stress is assumed for the case of additional straining; this is reflected by subsequent loading surfaces (concentric ellipses, Fig. 13) which shrink to the origin from 3<sup>rd</sup> quadrant.

Reinforcing steel is assumed to be elastic - perfectly plastic in both compression and tension. In the finite element procedure the reinforcement in each direction is replaced by an equivalent layer of steel which is uniformly distributed across the element containing the reinforcement; this layer has stiffness only in the directions of the reinforcement (i. e. , it possesses no shear stiffness).

In a reinforced masonry element, compatibility of displacements is assumed between steel and concrete. The stresses and constitutive relations of a reinforced element are derived by superposition of the masonry element and the steel layer element. The effect of bond degrada-

---

<sup>†</sup> A cracked element or region may, in general, have two sets of cracks. The second set of cracks can form while the first set is either open or closed.

tion between steel and cracked masonry is included in a "transition stage".

Complete details of the material model and related numerical algorithms can be found in Reference 10.

For simulation purpose, the shear wall assembly of Fig. 9(b) was discretized into a system of plane stress elements for the masonry and the loading beam, truss elements for the columns, and vertical interfaces for the head joints (Fig. 32). Grouted units and adjacent mortar were represented by a single material whose properties were obtained by a mixture or weighting procedure<sup>(9)</sup>. In all, the discretized system had 376 degrees of freedom and a bandwidth of 30. The finite element model was subjected to a constant vertical prestress of 50 psi to simulate test conditions, and a quasi-static horizontal displacement history at the center of the top load beam. The finite element analysis was performed using the tangent stiffness method; details of the latter can be found in Reference 10.

The results of the monotonic loading tests are presented in Figs. 33, 34. Excellent correlation between experiment and analysis is observed with respect to initial stiffness, stiffness degradation, and ultimate strength. The analysis indicates that stiffness degradation is caused by an accumulation of head joint failures and microcracking; the initiation of the major load-drop is due to the formation of a zone of macrocracks, a typical example of which is shown in Fig. 35.

The results of the cyclic loading tests are presented in Figs. 37, 38. Figure 37 reveals good correlation between experiments and theory for a very complex process. Figure 38 shows the envelopes of the load-deflection histories for the first quadrant. Once again, one observes stiffness degradation due to accumulated head joint failures and microcracking, and large load - drops in the load displacement history due to the formation of single and X-macrocracking zones; Figure 36 is typical of the latter.

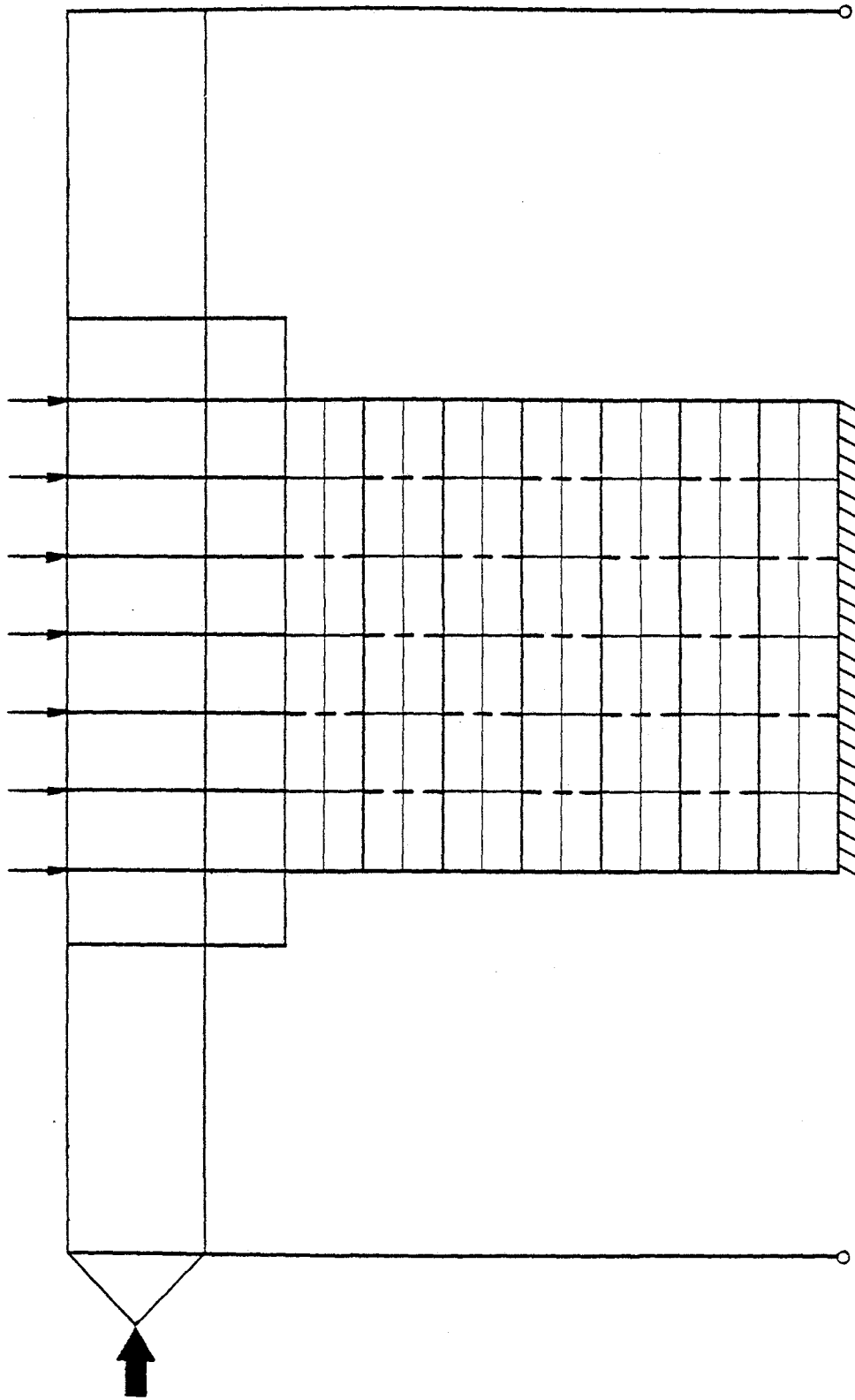


Fig. 32 Shear Wall Finite Element Discretization

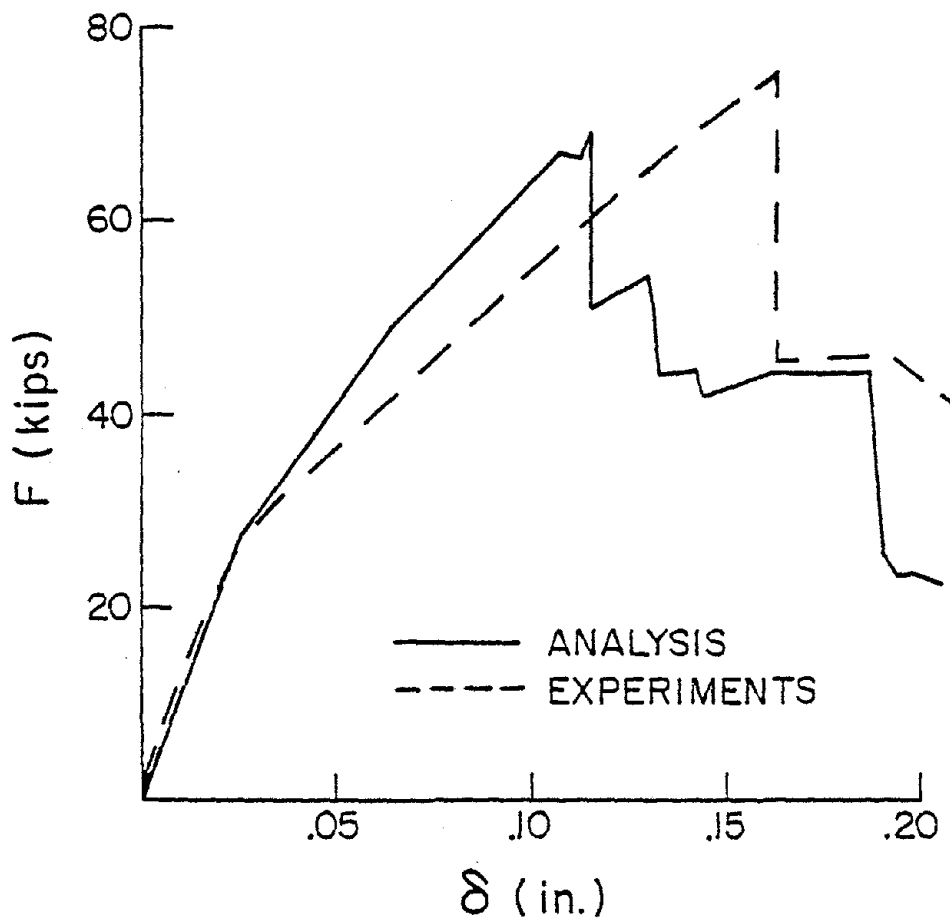


Fig. 33 Reinforced Shear Wall under Monotonic Loading

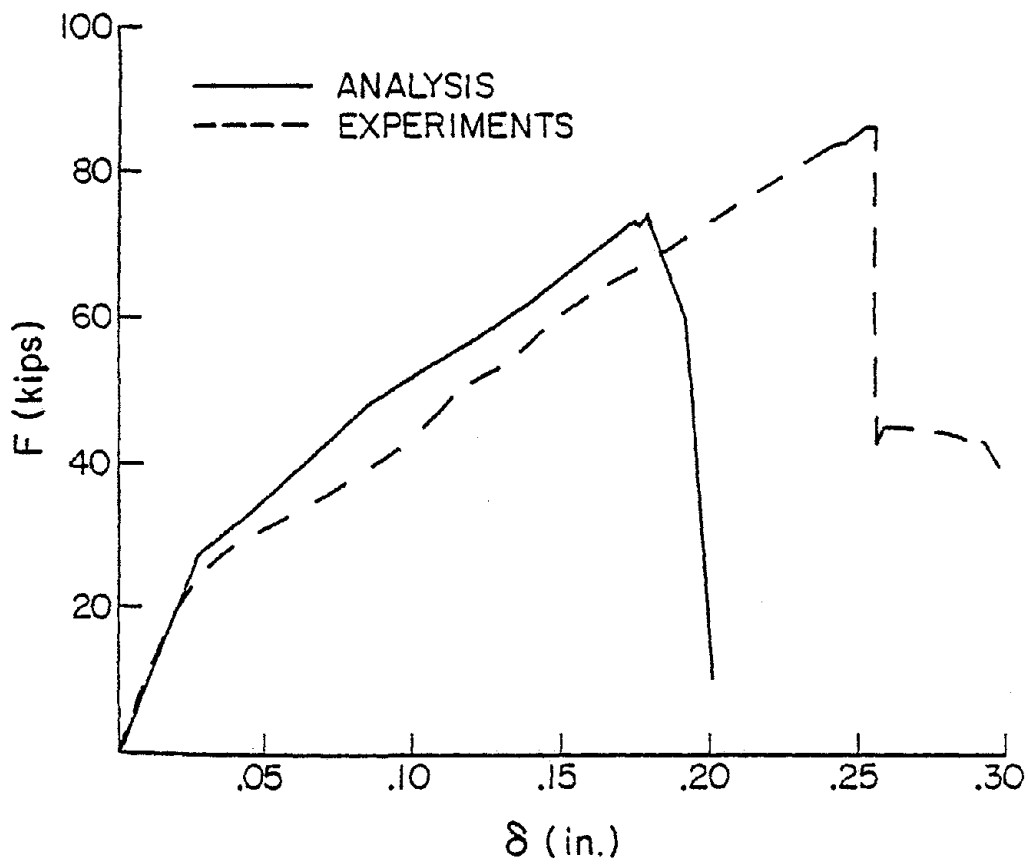


Fig. 34 Unreinforced Shear Wall under Monotonic Loading

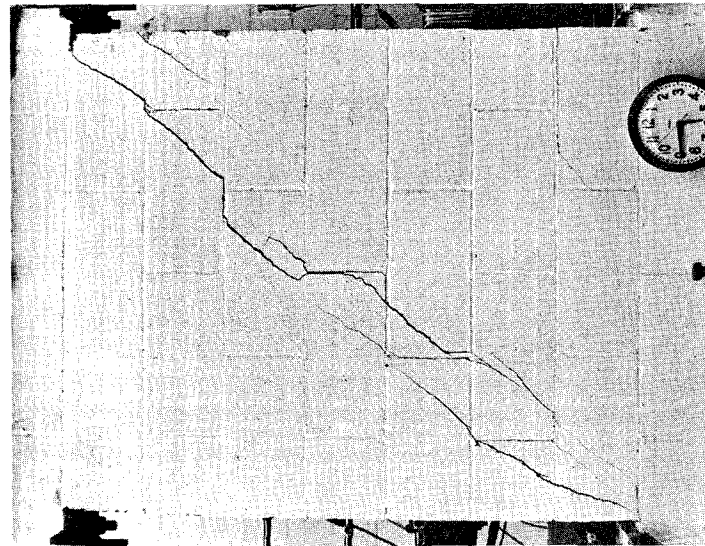


Fig. 35 Macrocracks in Reinforced  
Shear Wall under Monotonic  
Loading

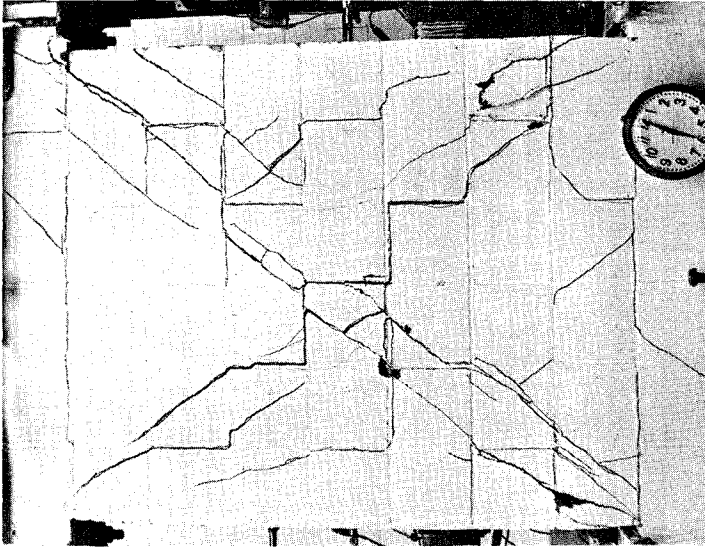


Fig. 36 X-Macrocracks in Reinforced  
Shear Wall under Cyclic  
Loading

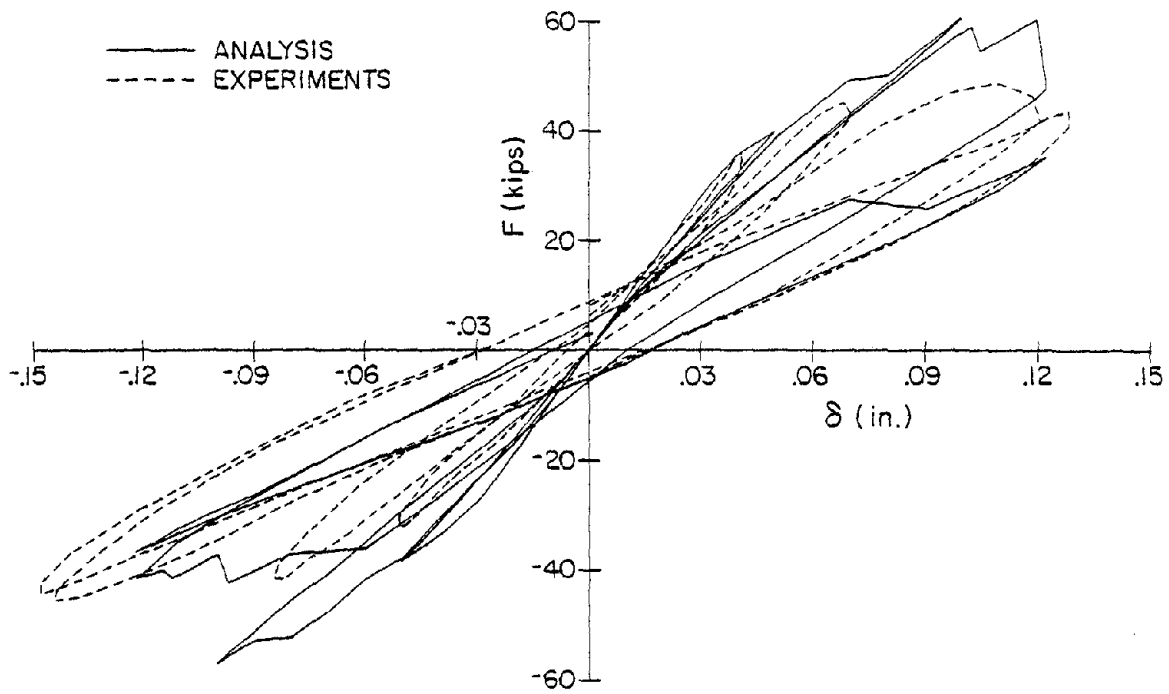


Fig. 37 Reinforced Shear Wall under Cyclic Loading

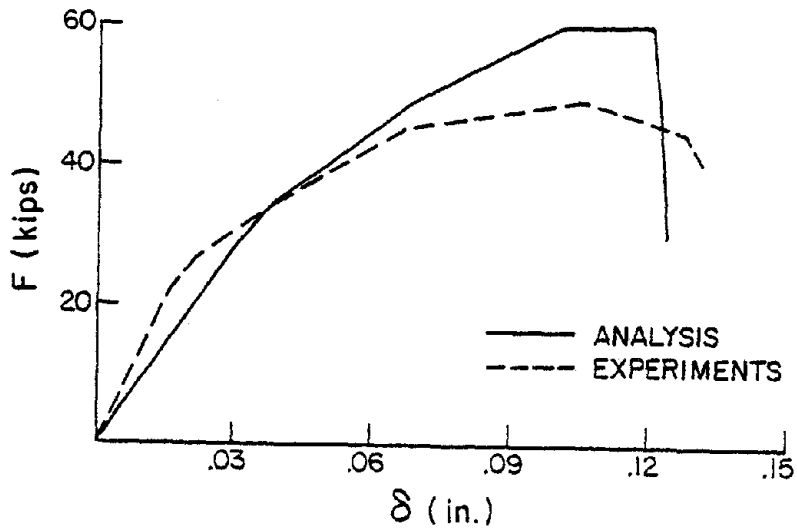


Fig. 38 Failure Envelopes for Reinforced Shear Wall under Cyclic Loading

### 9.2.2 Macromodel

Based upon 1) a linear finite element analysis, 2) the initial macrocracking envelope (obtained from homogeneous tests or component properties) and 3) the premise that macrocracking initiates in the central element, one can predict the ultimate load of Figs. 33, 34 within ten to fifteen percent accuracy. Such a simple approach does not, of course, reveal damage accumulation, the resulting stiffness degradation, and the proper hysteretic behavior. A macromodel capable of reflecting these items is under development.

## 10. SELECTED RESULTS - SMALL SCALE TESTS

Once again, a complete description of the small scale tests is beyond the scope of this presentation. Below several representative tests and sample results are provided in order to give the interested reader a proper perspective of the program.

### 10.1 Prism Tests

An important objective of these tests<sup>(11)</sup> is to identify current masonry industry testing procedures and potential problems, and to determine the influence on strength of prism geometry, capping method, bond configuration, mortar strength, mortar thickness, mortar bedding, and bearing plate thickness. One such subject - prism geometry - is discussed below.

Present working stress design methods are based primarily upon a knowledge of the masonry compressive strength,  $f'_m$ , which is usually determined by prism tests. Current masonry codes and design recommendations<sup>(1)</sup> either explicitly or implicitly recommend that  $f'_m$  be computed on the basis of 2-course prisms laid in stack bond, and capped according to ASTM C140 wherein a sulfur fly-ash compound or a high strength gypsum plaster is used. Test procedures correspond to ASTM E447. Code correction factors purport to enable conversion of the strength of a particular geometry to that of a standard prism. A UBC correction factor of unity is presently applied to the 2-course prism ( $h/t = 2.0$ ). This evidently implies that a strong correlation with  $h/t = 2.0$  and full-scale masonry exists. Our research clearly indicates that this premise is false and nonconservative. In particular, test data indicates that prism strength is significantly influenced by load-platen

restraint and, in the absence of a soft capping material, is a strong function of the number of courses - up to 4 to 5 courses. In addition, strength is a function of bond geometry.

A typical example is illustrated in Fig. 39. The data, which is normalized on the mean of 2-course prism results, was obtained from full block, fully grouted specimens; precision cutting to the desired h/t ratio was utilized in place of a high-strength capping material (cutting allows independent variation of the h/t ratio and the number of bed joints; no difference in results between cut and capped surfaces was found for high strength capping materials). The bearing platens at each end consisted of 8 by 8 by 16-inch aluminum blocks. For stack bond prisms, platen restraint resulted in a shear-mode failure in 2-course prisms, and combined shear-tensile splitting in 3-course prisms. Proper tensile splitting was observed (in courses not adjacent to the platens) in 4 and 5-course prisms. Strength was observed to decrease up to 4 courses, and remained constant between 4 and 5 courses. Also, the data indicates that prism strength is largely a function of the number of (bed) joints in the specimen - not the h/t ratio. Similar trends were observed for running bond specimens (vertical joints were not placed adjacent to load platens). It is emphasized, however, that the strength of running bond prisms was considerably less than stack bond prisms (see Fig. 39). The component properties for the specimens discussed above are given in Table 11.

Finally, an extensive literature review (see Reference 1) revealed an amazing fact: Virtually all code correction factors for prism geometry are based upon a common source - the preliminary and exploratory investigation by Krefeld in 1938 (see Reference 1 - on brick). This is patently unjustified. A correlation of Krefeld's work with a number of codes is shown in Table 12 (each code is based upon a different "standard" prism

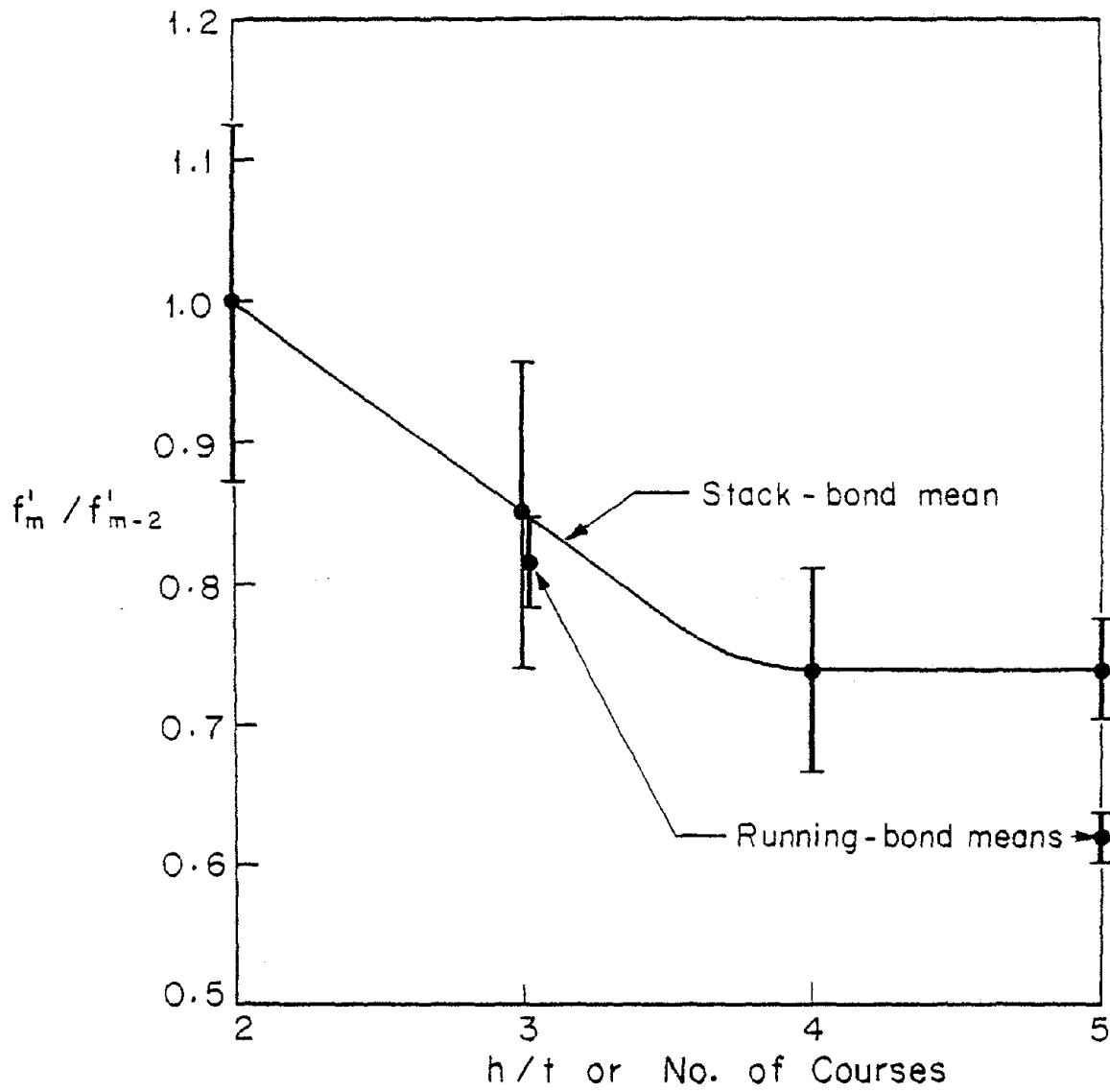


Fig. 39 Correlation of Prism Strength and Geometry

Table 11. Component Properties for Full-Block Prism Tests

	Block*	Mortar	Grout
	3705	1974	2828
	4000	1639	3429
Compressive	3990	1958	2039
Failure Stress	3148	1592	2299
(psi)		1639	
		1241	
		1868	
		2212	
		1353	
mean	3711	1720	2649
std. dev.	399	312	615

\*Tests conducted on saw-cut coupons.

Table 12. Comparison of Correction Factors for Prism Shape after "Code Factor" Modification

Source	"Code factor"	h/d=*						
		1.5	2.0	2.5	3.0	4.0	5.0	6.0
Krefeld	—	0.59	0.67	0.75	0.80	0.89	0.96	1.00
New Zealand Standard	1.50	0.58	0.67	0.74	0.80	0.89	0.95	1.00
Australian Standard	1.25	—	0.68	0.74	0.80	0.88	0.93	0.93
Canadian Code (concrete)	1.50	0.57	0.67	0.74	0.80	—	—	—
Canadian Code (brick)	0.93	—	0.68	0.74	0.80	0.89	0.93	—
Uniform Building Code	1.50	0.57	0.67	0.74	0.80	—	—	—
National Bureau Standards	1.50	0.57	0.67	0.74	0.80	—	—	—
Structural Clay Prod. Inst.	0.93	—	0.68	0.74	0.80	0.89	0.93	—

\* h/d is referred as h/t in the text.

geometry-hence the normalization factor may be different). In view of the above discussion, one would expect poor correlation between 2-course prism and wall data; this is demonstrated by tests by Read and Clements on ungrouted walls, Fig. 40 (see Reference 1).

## 10.2 Joint Behavior

Data on joint fracture and post-fracture behavior is prerequisite to a basic understanding of failure processes, and is necessary for modeling on the micro-scale. A typical test-setup for monotonic loading of full-blocks is illustrated schematically in Fig. 41 (a). The dynamic test fixture is shown in Fig. 41 (b). A typical test setup for the dynamic tests is illustrated in Figs. 41 (c, d). In each test a constant normal stress was maintained across joint-planes, and the shear-stress distribution on these planes was varied by driving the center block in displacement control. Figures 42 and 43 exemplify typical static and dynamic behavior for grouted and ungrouted bed joints. The following basic characteristics are noted: 1) joint fracture strength increases monotonically with pre-compression up to a block-failure transition (the maximum shear stress vs. normal stress for both grouted and ungrouted specimens is shown in Fig. 45); 2) under precompression exceeding or equal to 100 psi, fracture load decreases with displacement<sup>(12)</sup> (Fig. 42) in a relatively smooth manner to a limiting value which, in turn, depends upon the level of precompression; 3) no discernible rate-dependence is evident in the range .01 to .50 in/sec. under monotonic loading (Fig. 43) and in the range .05 to .50 Hz under cyclic loading; 4) cyclic experiments (Fig. 44) indicate that, following the first load reversal, load-displacement history is a function only of total displacement-path length and is not direction-sensitive; 5) ultimate strengths of head joints, and ungrouted bed joints are considerably less than associated grouted bed joints; 6) in the absence of

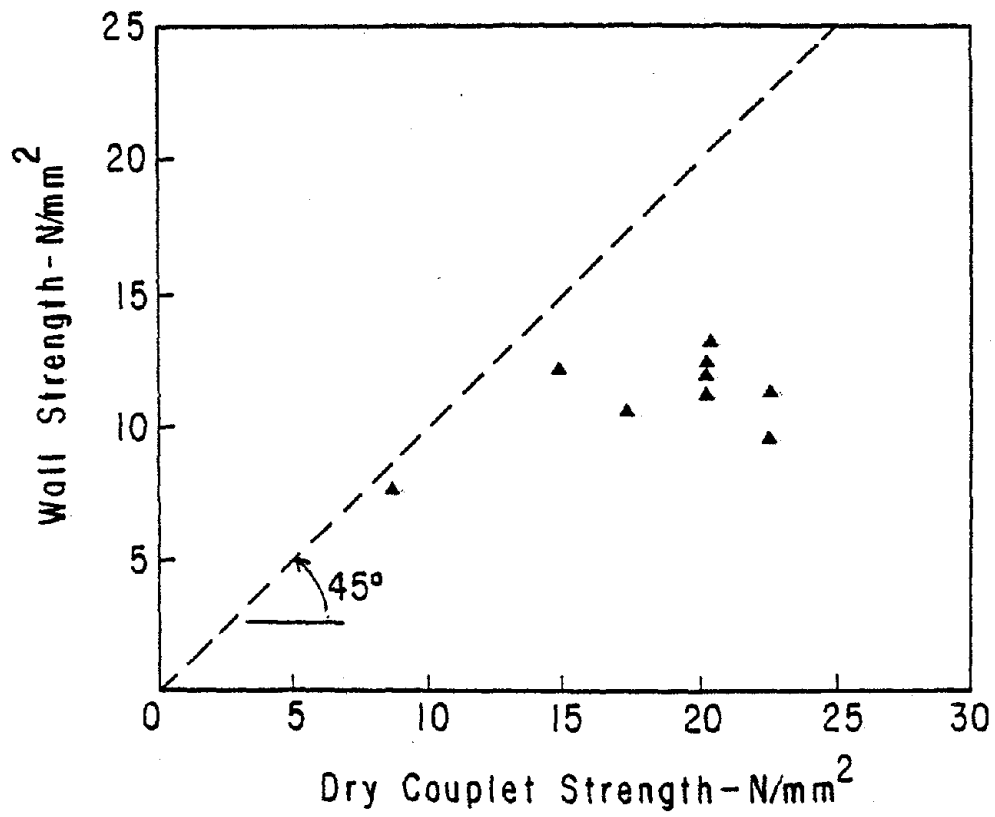


Fig. 40 Comparison of UngROUTed Wall and Couplet Strengths

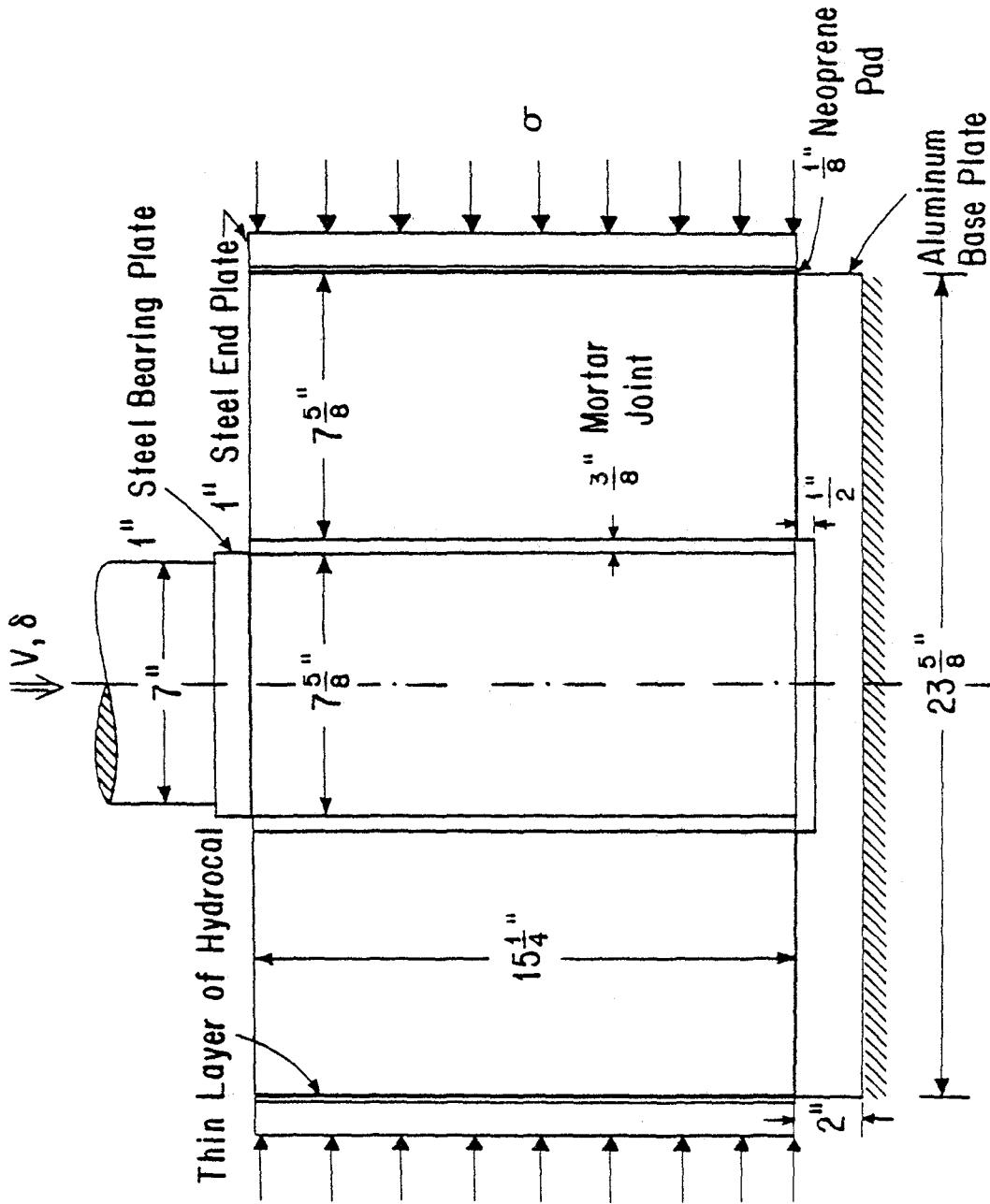


Fig. 41 (a) Joint-Test Specimen

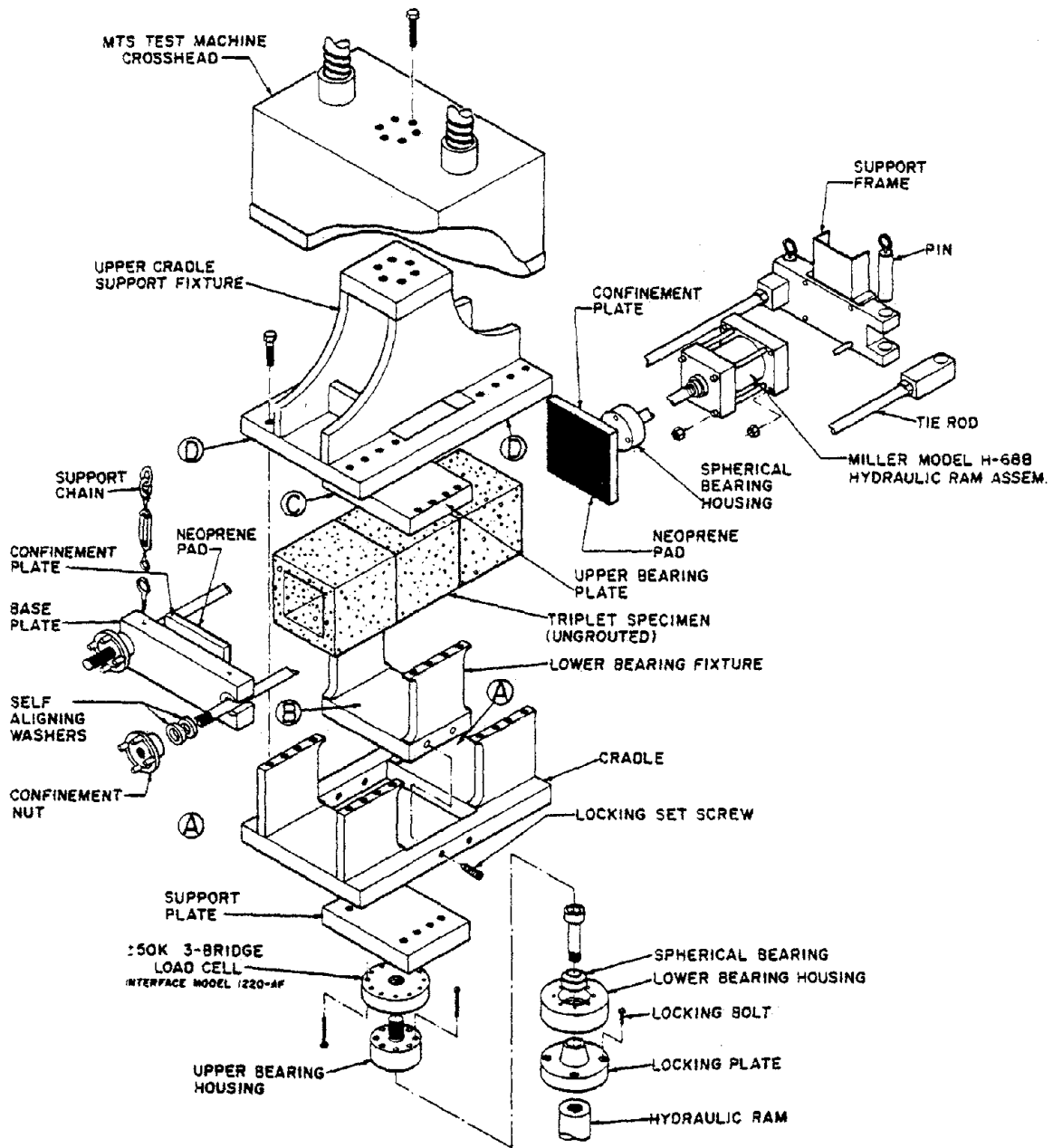


Fig. 41 (b) UCSD Cyclic Joint-Test Fixture

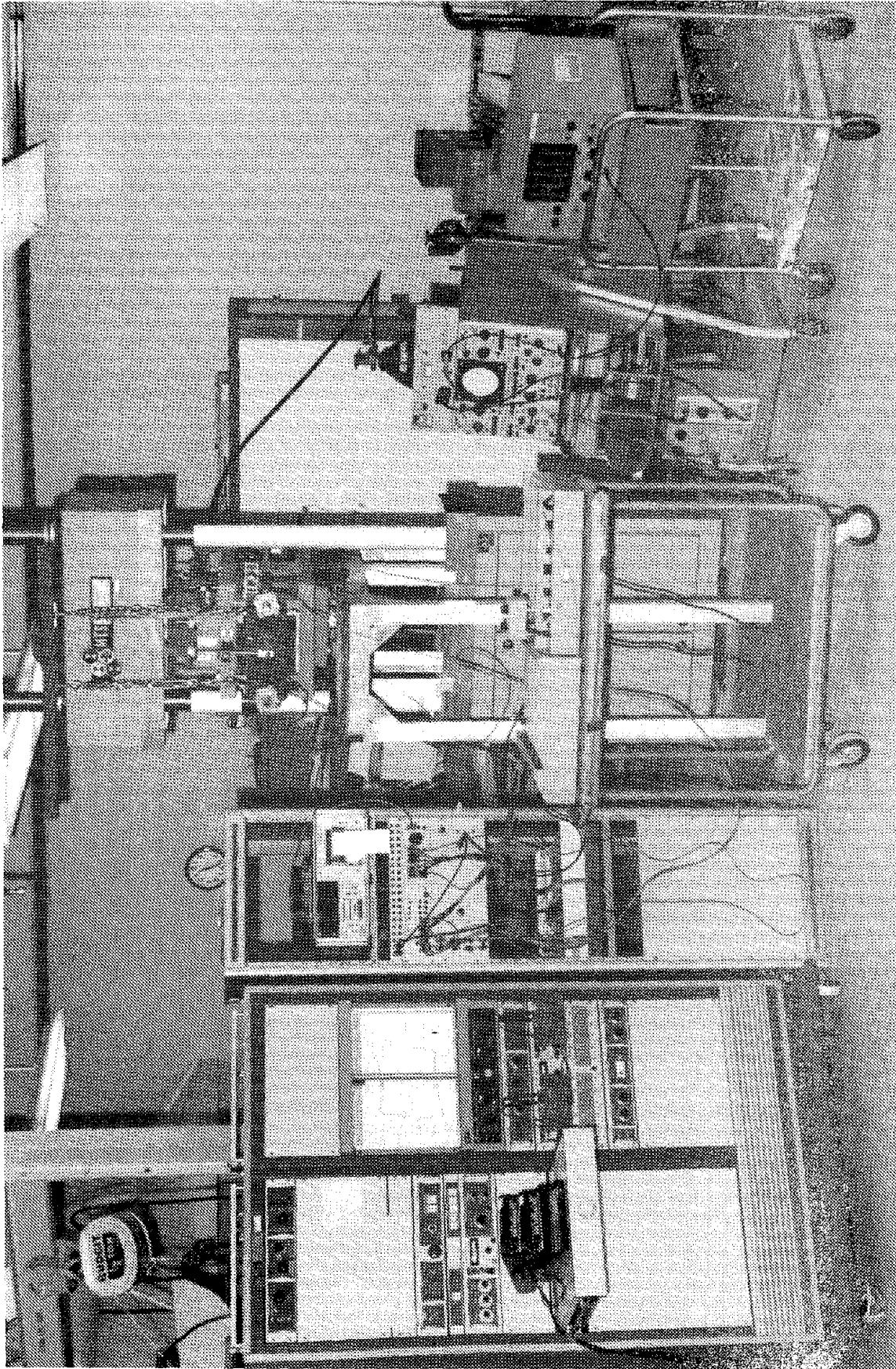


Fig. 41 (c) UCSD Joint-Test Setup

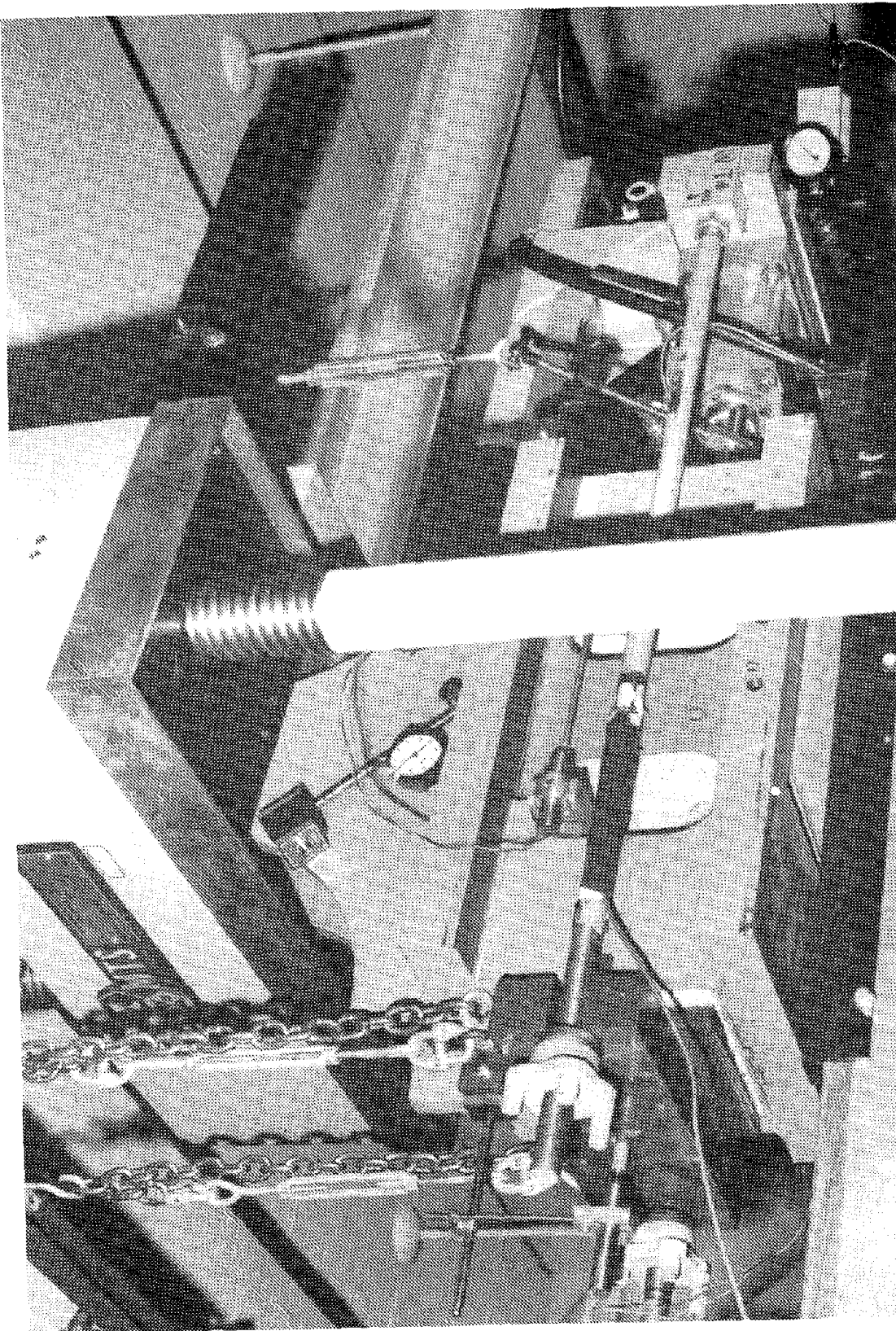


Fig. 41 (d) UCSD Cyclic Joint-Test Fixture and Specimen

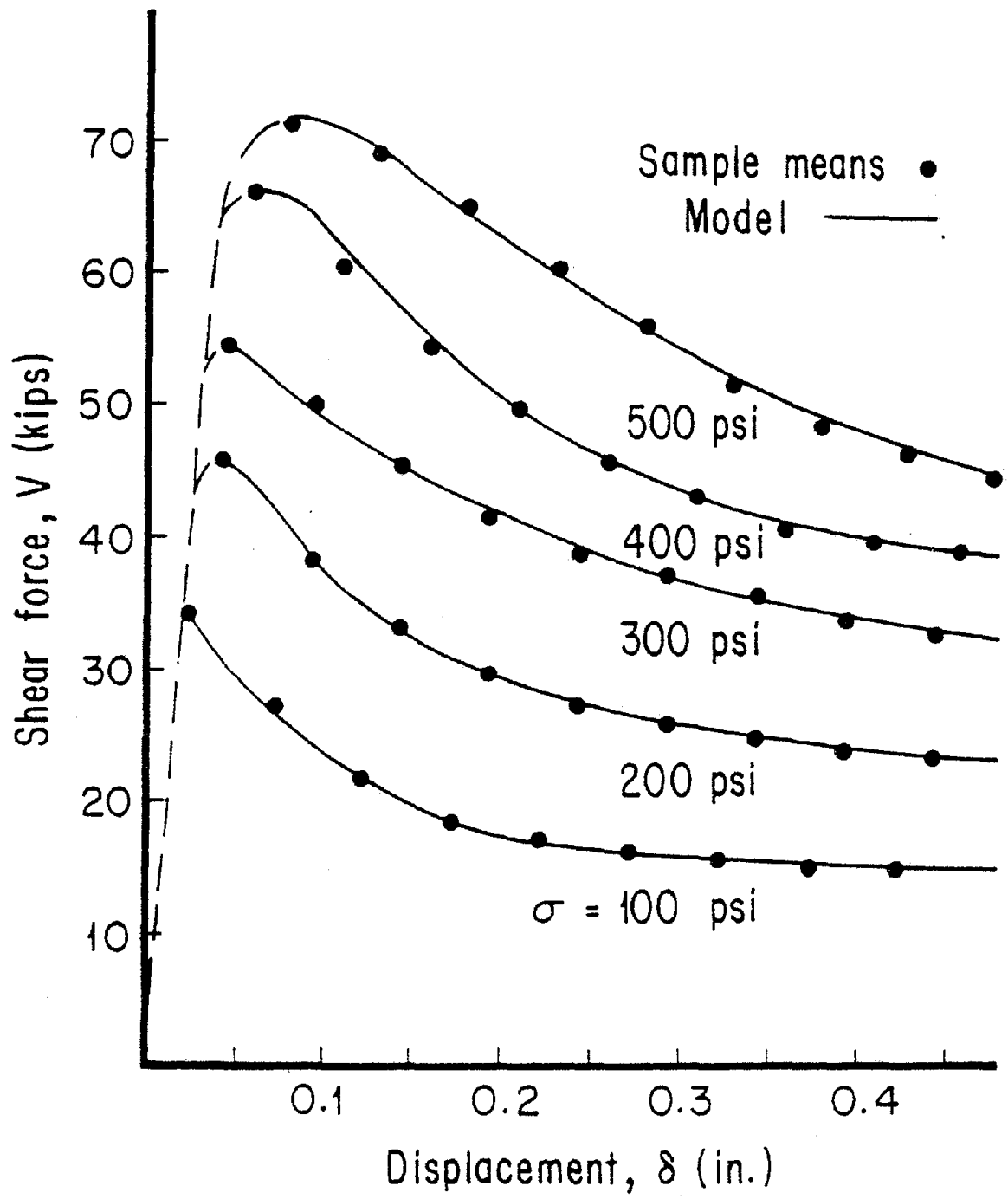


Fig. 42 Behavior of Bed Joints under Precompression

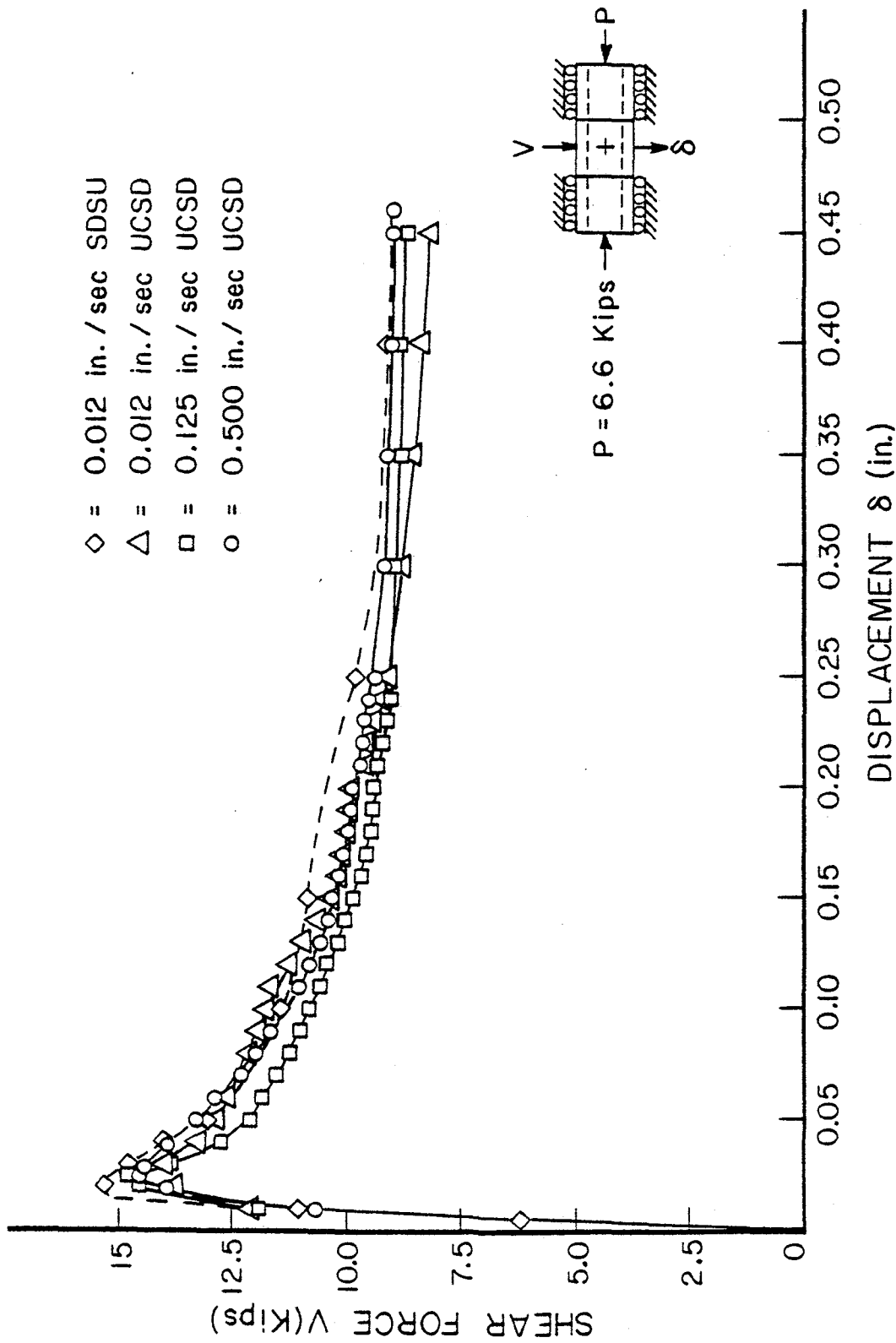


Fig. 43 Strain-Rate Dependence

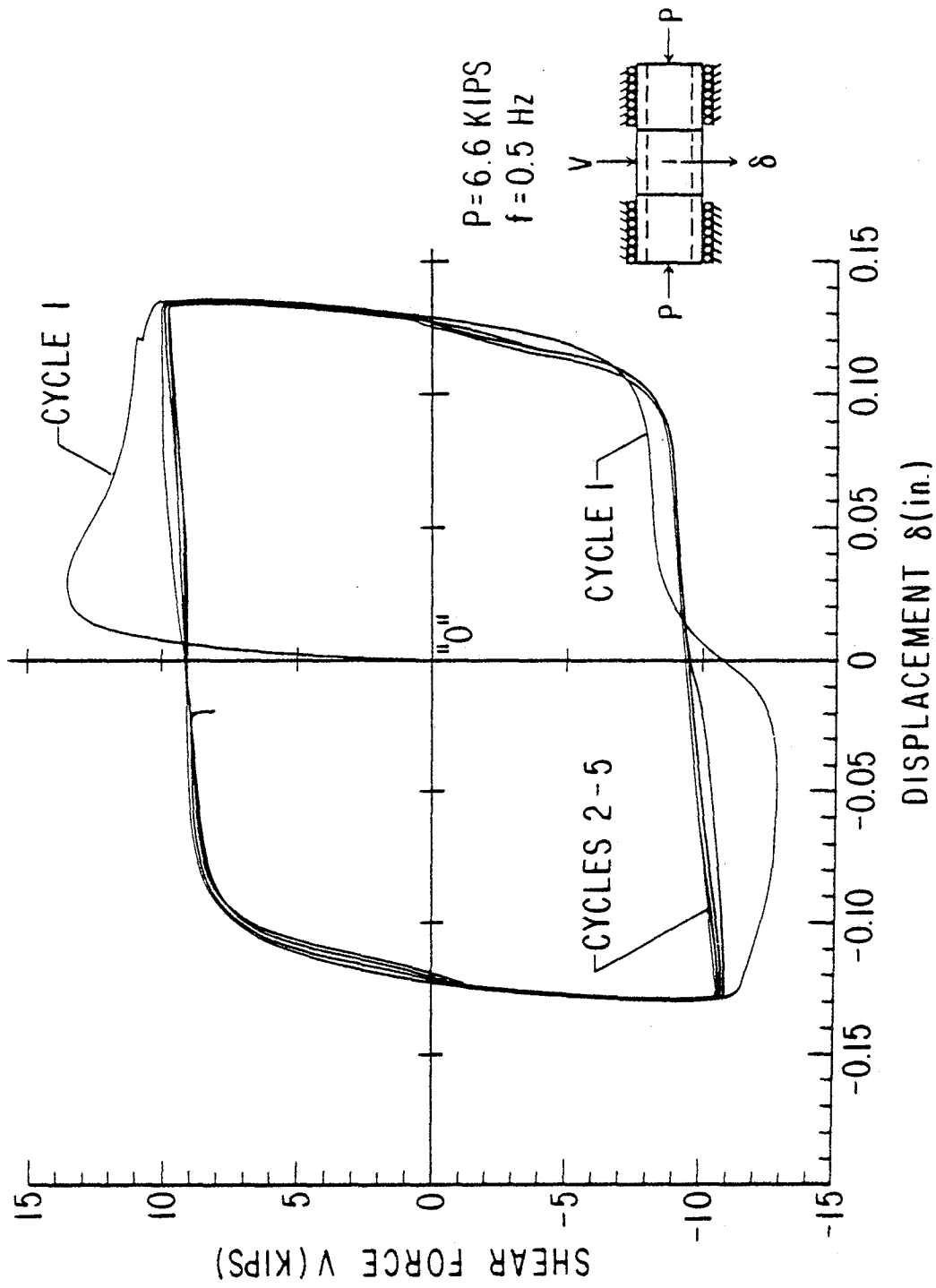


Fig. 44 Joint under Cyclic Loading

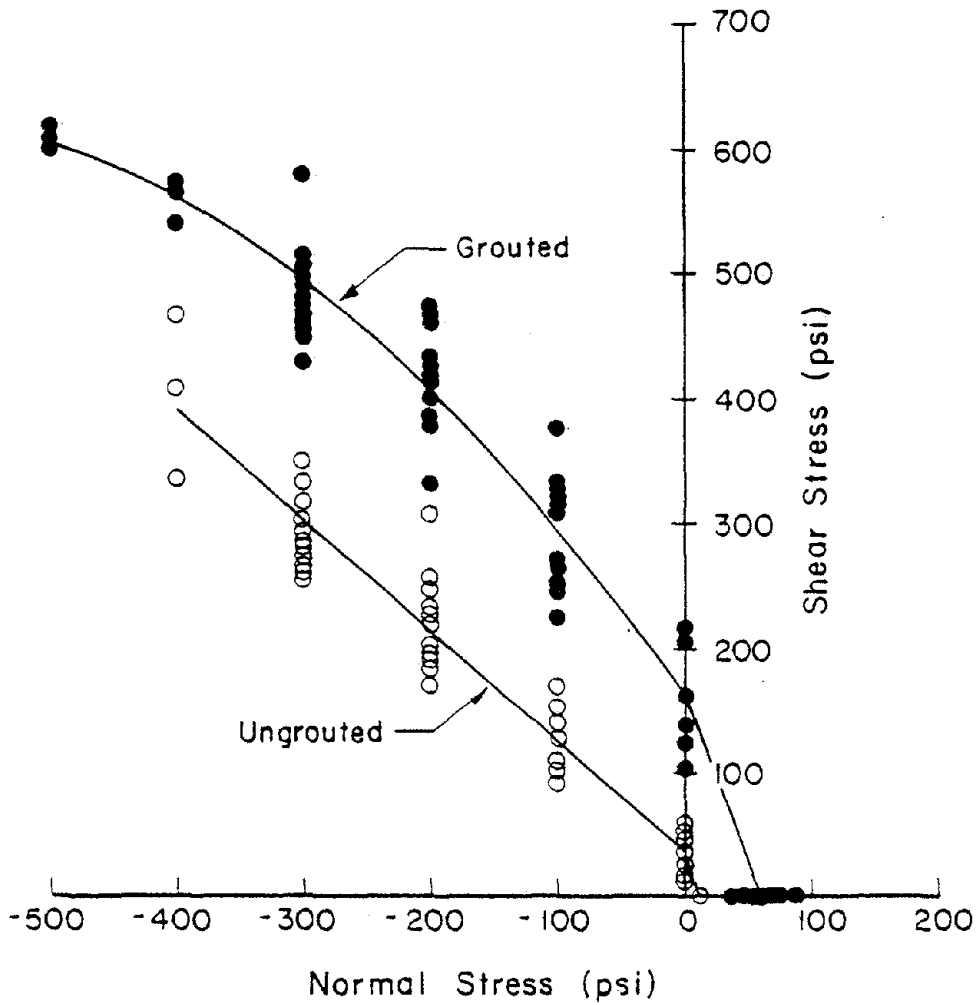


Fig. 45 Dependence of Joint Maximum Shear Stress on Normal Stress

precompression, joint behavior is brittle - ungrouted bed and head joints exhibit extremely low (3-30 psi) shear and tensile strengths as well as large data-scatter.

Finite element simulation<sup>(9)</sup> of the joint tests was performed as a first step in the micro-modeling process. Local properties were established which enabled the analysis to match the experimental  $V$  vs.  $\delta$  data and which are reasonable when judged against independent measurements of interface strength. A typical correlation for ungrouted bed joints is shown in Fig. 46. Agreement is seen to be good. Subsequent to "tuning" the simulation of joint data, the above finite element model was utilized to predict biaxial panel behavior without further "tuning".

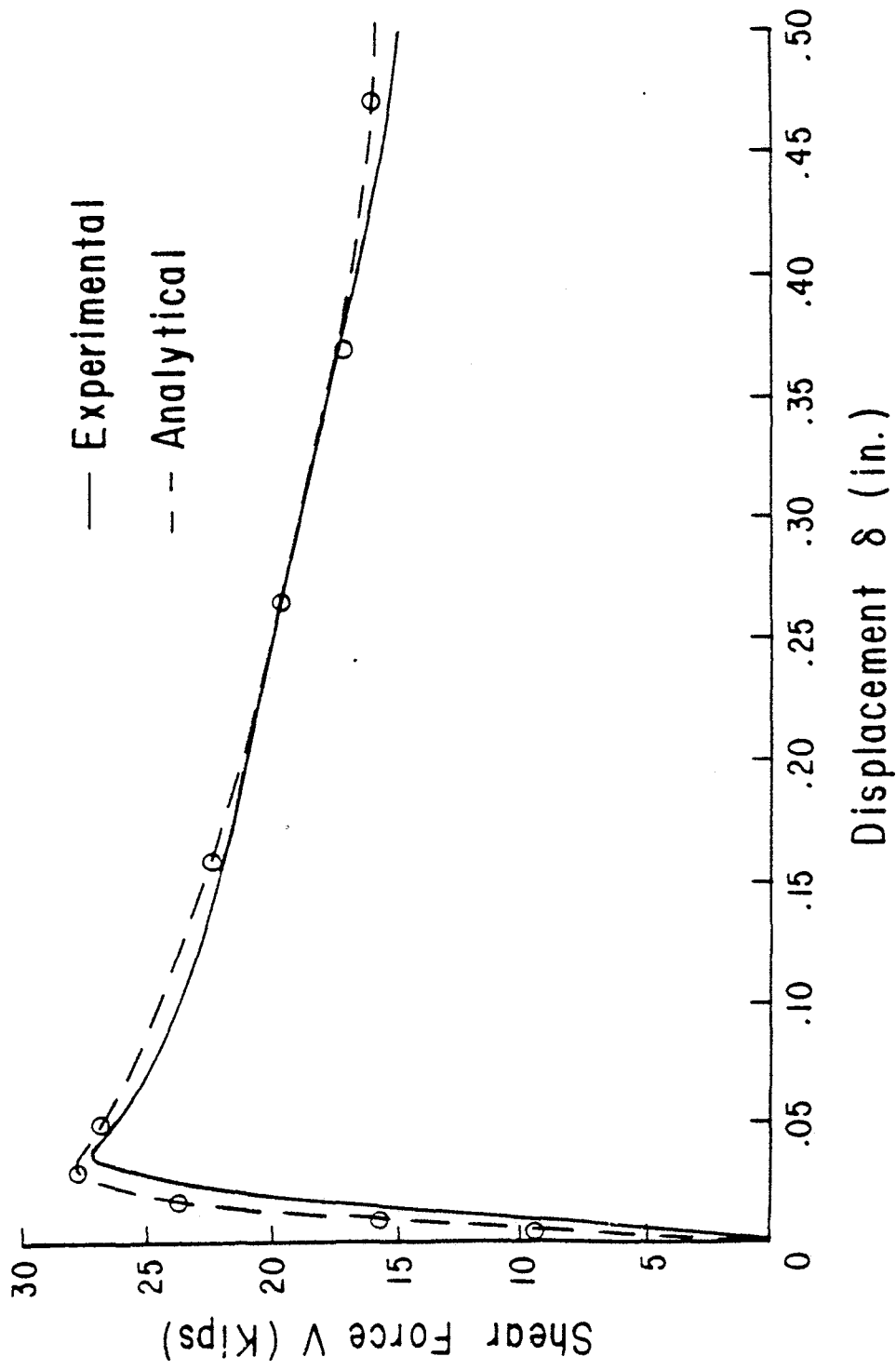


Fig. 46 Finite Element Simulation of Joint Behavior

## 11. REMARKS ON ADDITIONAL STUDIES

In addition to the research discussed briefly in the previous sections, a number of tests and concurrent modeling are in the development stage. Among these are included combined planar and nonplanar loading of both fully grouted and partially grouted reinforced concrete masonry, and the behavior of connections. The latter is particularly noteworthy.

Connections between floors and walls, and between walls, are major components of masonry structures. The basic functions of such connections are depicted in Fig. 47 for a typical multistory concrete masonry building. Of singular importance is the in-plane load transfer capability of a connection. Such data, however, is not available in the literature. Consequently, as a supplement to the material studies, connection studies have been initiated, beginning with the in-plane motion of typical floor-to-wall designs.

Three different connection types have been selected for initial study on the basis of discussions with the Advisory Panel for the present project; this Panel contains a number of structural engineers who are experienced in the seismic design of masonry structures. These connection types were also presented to structural engineers outside the Advisory Panel, and to members of a recent workshop<sup>(3)</sup> on masonry. Although there is disagreement among practicing engineers as to what details are most commonly used, there is a consensus that the types of connections illustrated below are common. Other types and details may be considered later.

The first major type of connection involves precast, reinforced concrete slabs supported by an interior wall. Two construction details for this type are shown in Figs. 48 and 49. In the detail of Fig. 48, bars embedded in the slab are bent up at 36 inch spacing and embedded in the

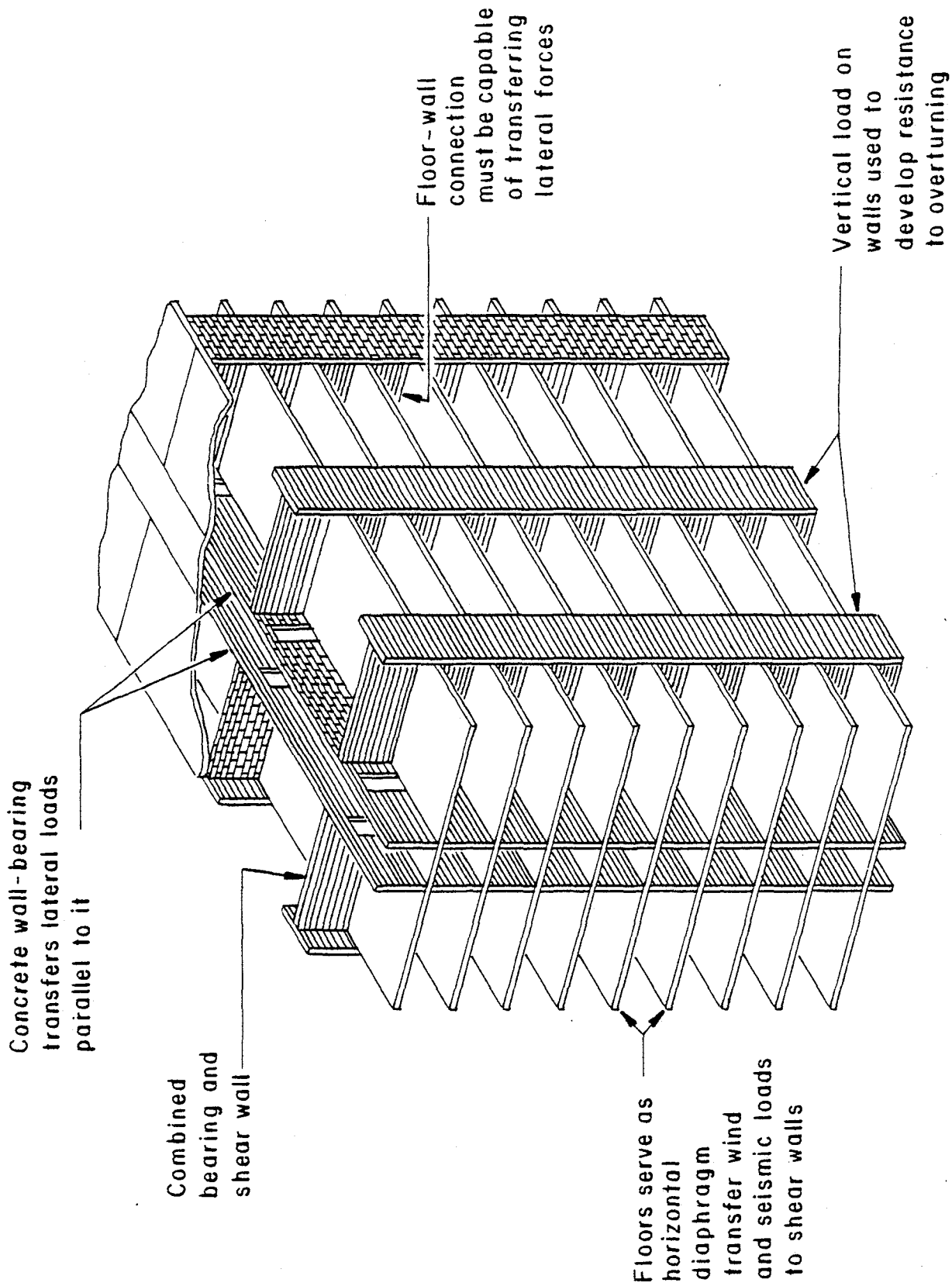


Fig. 47 Function of Connections in Shear Wall Structure

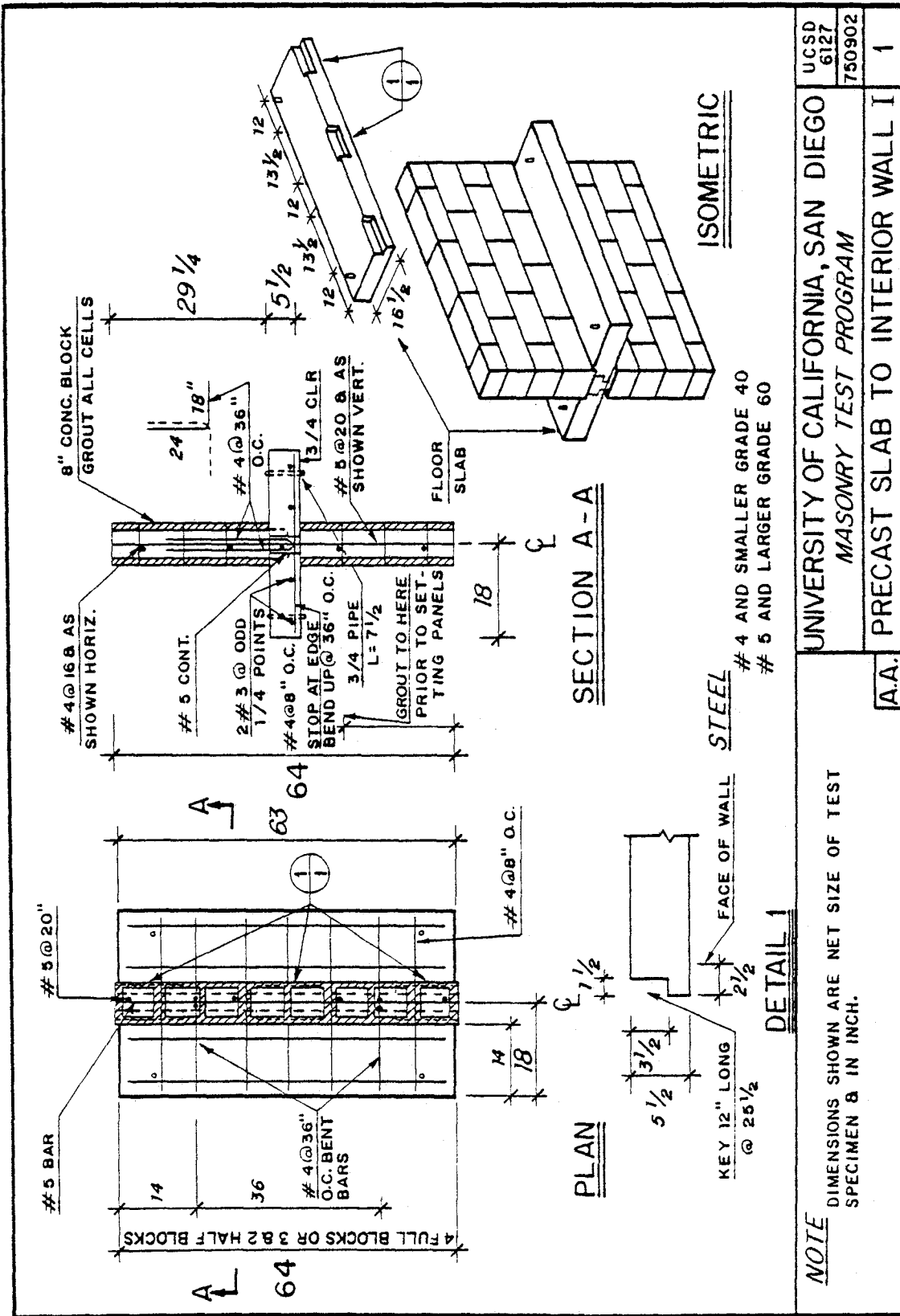
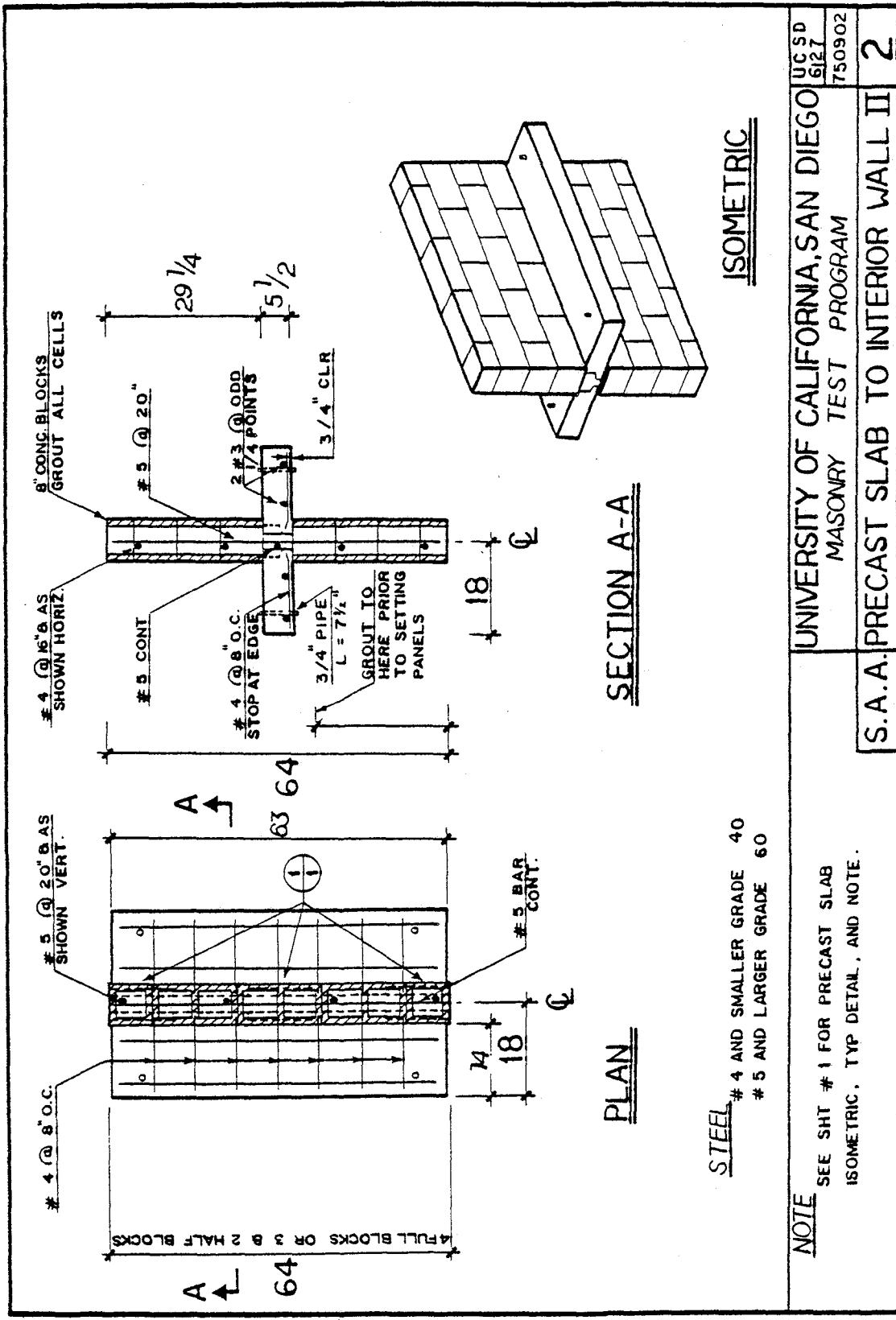


Fig. 48 Connection Detail of Precast Floor Slab and Interior Wall, Detail I



<p><b>NOTE</b></p> <p>SEE SHT # 1 FOR PRECAST SLAB ISOMETRIC. TYP DETAIL, AND NOTE.</p>	<p>UNIVERSITY OF CALIFORNIA, SAN DIEGO</p> <p>MASONRY TEST PROGRAM</p>	<p>UCSD 6127</p> <p>750902</p>
	<p>S.A.A. PRECAST SLAB TO INTERIOR WALL II</p>	<p>2</p>

Fig. 49 Connection Detail of Precast Floor Slab and Interior Wall, Detail 2

grout core, with one continuous No. 5 chord. All cells of the wall are grouted. A more elementary detail is shown in Fig. 49, in which there is only one No. 5 chord and shear transfer is provided by the floor-wall bond and the shear keys.

A second major connection type involves a cast-in-place slab supported by an interior wall, Fig. 50. Bars embedded in the top and bottom of the slab are continuous through the grout core. A continuous No. 5 chord is also set in the plane of the connection. All cells of the wall are grouted.

The third major connection type shown in Fig. 51 involves hollow-core, prestressed concrete planks supported by an interior masonry wall. In this detail, in addition to the common No. 5 chord in the grout, there are continuous bars in the concrete topping which is poured on the slabs. As in the other details, all cells of the wall are grouted.

Tests on the foregoing connections will be conducted in the biaxial test system described in Section 2, with modifications as illustrated in Fig. 52. The philosophy of the test is to prevent rigid body translation and rotation of the wall panel while applying horizontal motion to the floor. Initially a constant force will be applied in the vertical direction to simulate the weight of stories above the test floor. Eventually an oscillatory vertical force will be superposed on this constant to simulate the effects of overturning on the test wall-floor connection. The objective is to obtain reasonably uniform shear stresses and vertical normal stresses on the plane of the connection. The ultimate strength and the horizontal force-deflection relation, including a falling or softening branch, if any, are the main quantities of interest.

The initial in-plane test matrix is shown in Table 13. Studies will begin with quasi-static monotonic displacement and progress to cyclic displacement in the 1 Hz range.

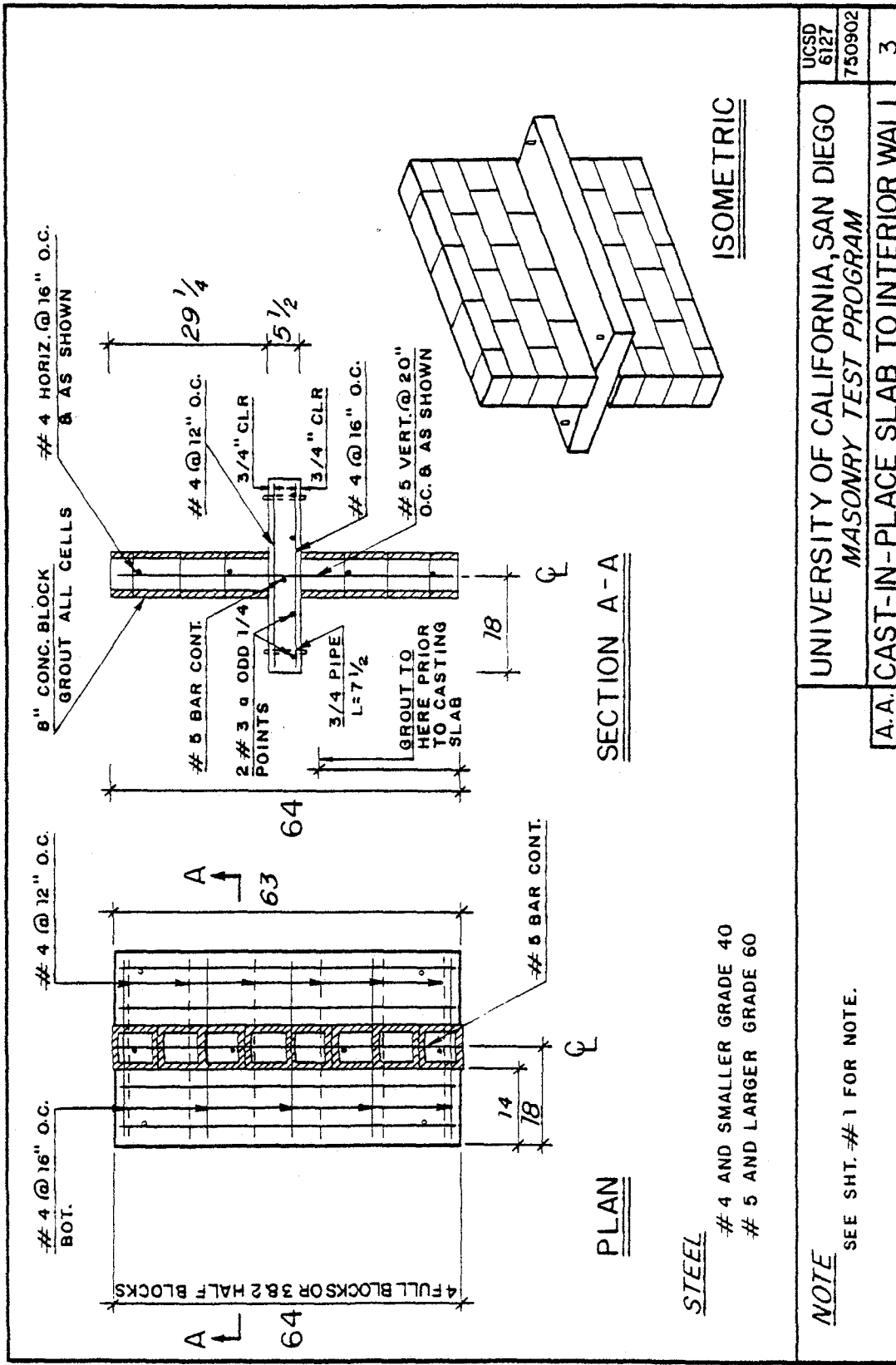


Fig. 50 Connection Detail of Cast-in-Place Floor Slab and Interior Wall, Detail 3

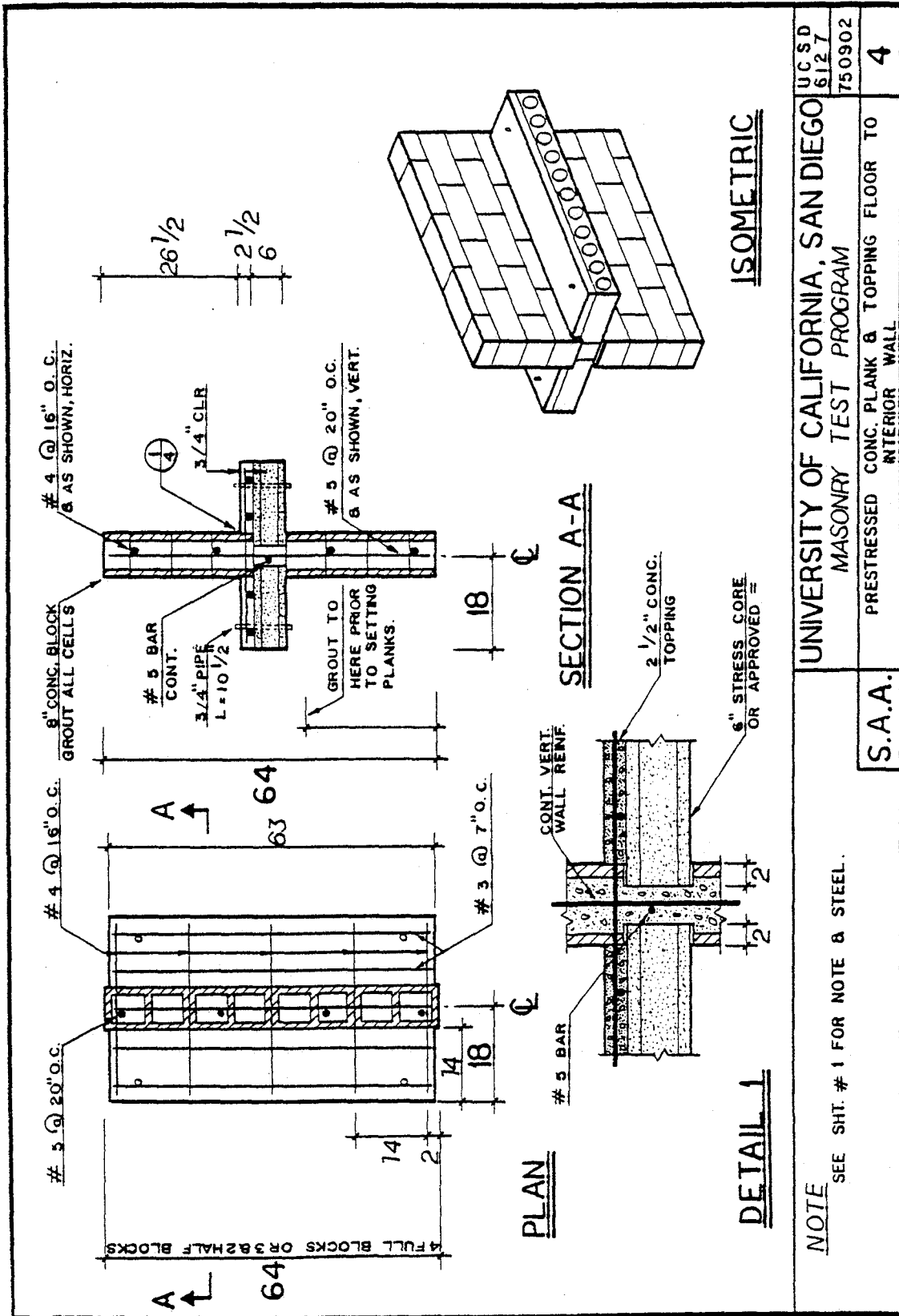
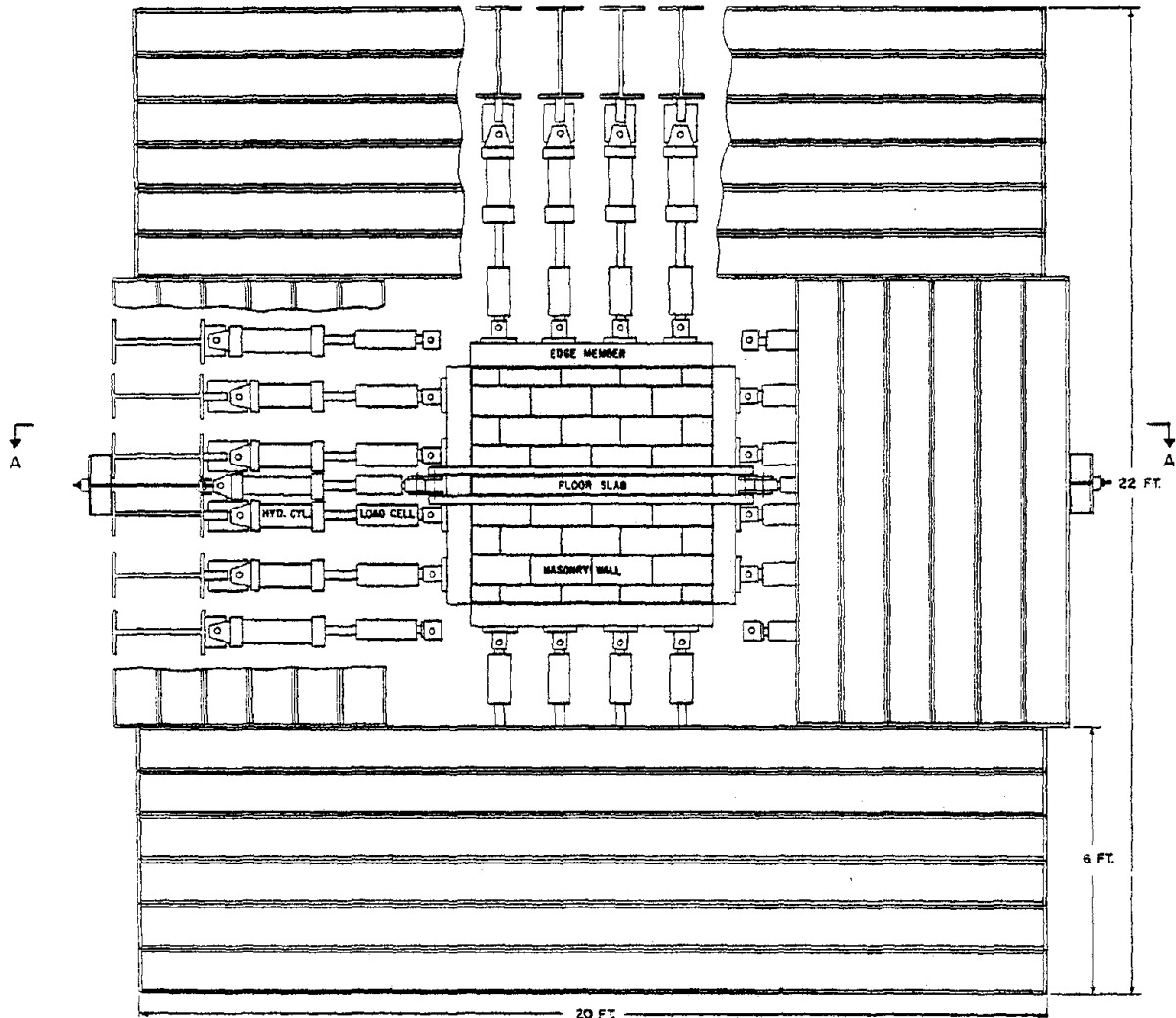
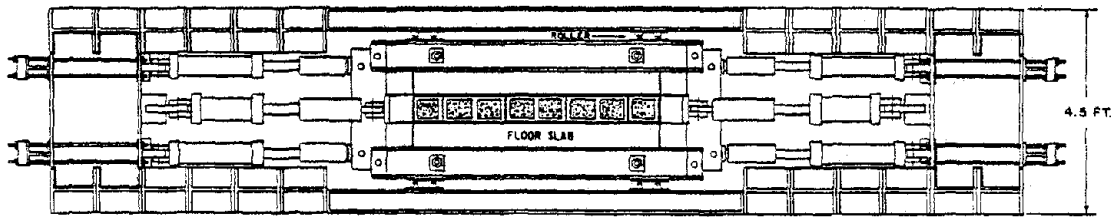


Fig. 51 Connection Detail of Prestressed Concrete Planks and Interior Wall, Detail 4



FRONT VIEW



SECTION A-A

Fig. 52 Connection Test Setup

Table 13. Connection Test Matrix

	VERTICAL DEAD LOAD ONLY		VERTICAL DEAD LOAD WITH OVERTURNING MOMENT
	<u>Mild Rise</u>	<u>High Rise</u>	
Precast slab to interior wall			<u>High Rise Only</u>
Detail #1	100-200 psi	200-500 psi	400 ± 200 psi
Detail #2	100-200 psi	200-500 psi	400 ± 200 psi
Cast-in-place slab to interior wall			
Detail #3	100-200 psi	200-500 psi	400 ± 200 pxi
Prestressed conc. plank & topping floor to interior wall			
Detail #4	100-200 psi	200-500 psi	400 ± 200 psi

Under seismic excitation, out-of-plane forces and/or moments are generated. Thus, one must eventually view the in-plane load transfer capability in the presence of out-of-plane forces and moments.

## 12. CLOSURE

The program described, in part, herein represents the first fundamental and comprehensive effort to describe the material properties of concrete masonry, and to synthesize the behavior of complex structural elements from basic component data.

The experimental apparatus necessary to generate data of integrity is, of necessity, complex and sophisticated. A time span of over two years has been necessary to bring all systems to a production basis. An avalanche of important information is now taking place. A similar statement applies to the analytical/numerical segment of the program.

One of the most significant results obtained to date has been the excellent correlation between experimental results and finite element simulations or modeling on the microscale. In particular, it appears that the complex macrobehavior of concrete masonry structural elements such as shear walls and piers under both monotonic and cyclic loading in the nonlinear regime of material response can be rationally predicted from masonry constituent properties and/or small scale tests. Likewise, when less detailed information is sufficient, the excellent correlation between experimental results and the macromodeling process indicates that information of importance to both the analyst and the designer can be obtained from component properties and/or small scale tests; an example here is an elementary theory to predict the initiation of major cracking.

The program has revealed flaws in standard masonry construction, the influence of such flaws on strength, and fabrication methods leading to a superior material via the reduction of flaws.

The program has demonstrated the need for a number of building code modifications related to testing techniques and interpretation of test data.

Finally, masonry is some 20 years or more behind concrete with respect to knowledge of material properties. Such a gap cannot be closed overnight. It is imperative that programs of the type discussed in this paper be sustained for a time period sufficiently long to allow the effort to come to fruition.

It is also imperative that the masonry industry organize on a national basis - much as the concrete industry has - if progress in this area is to be made within a reasonable time period. The absence of comprehensive knowledge concerning fundamental material properties - if allowed to continue - can only invite potentially enormous safety and economic problems.

## ACKNOWLEDGEMENT

Publication of this report was facilitated by a contribution from the Unit  
Masonry Association of San Diego, Inc.

## REFERENCES

1. Hegemier, G. A., "Mechanics of Reinforced Concrete Masonry: A Literature Survey," Report No. AMES-NSF TR-75-5, University of California, San Diego, 1975
2. Mayes, R. L., and R. W. Clough, "A Literature Survey - Compressive, Tensile, Bond and Shear Strength of Masonry," Report No. EERC 75-15, University of California, Berkeley, 1975.
3. Isenberg, J., G. A. Hegemier, and A. Anvar, "An Experimental Study of Connections in Reinforced Concrete Masonry Structures under Seismic Loading," Proceedings of Workshop on Earthquake Resistant Masonry Construction, National Bureau of Standards, September 13-17, 1976.
4. Hegemier, G. A., G. Krishnamoorthy, and R. O. Nunn, "An Experimental Study of Concrete Masonry under Seismic-Type Loading," Proceedings of Workshop on Earthquake Resistant Masonry Construction, National Bureau of Standards, September 13-17, 1976.
5. Hegemier, G. A., R. O. Nunn, M. E. Miller, S. K. Arya, and G. Krishnamoorthy, "On the Behavior of Concrete Masonry under Static and Dynamic Biaxial Stress-States," Report No. AMES-NSF TR-77-3, University of California, San Diego, 1977.
6. Hegemier, G. A., M. E. Miller, and R. O. Nunn, "On the Influence of Flaws, Vibration Compaction, and Admixtures on the Strength and Elastic Moduli of Concrete Masonry," Report No. AMES-NSF TR-77-4, University of California, San Diego, 1977
7. An Evaluation of Response Spectrum Approach to Seismic Design of Buildings, A Study Report for Center for Building Technology, Institute of Applied Technology, National Bureau of Standards, Washington, D. C. 20234, by Applied Technology Council (ATC-2), San Francisco, California, September 1974.
8. Dickey, W. L. and R. W. Harrington, "The Shear Truth about Brick Walls," Report for Western States Clay Products Assoc., Inc., San Francisco, California, 1970.

9. Arya, S. K., "A Method for Incorporating Interface Discontinuities in Finite Element Analyses with Application to Concrete Masonry Rheology," Weidlinger Associates Report No. R-7522, prepared for the University of California, San Diego, 1975.
10. Arya, S. K. and G. A. Hegemier, "A Nonlinear Material Model for Reinforced Concrete Masonry with Application to Shear Walls," Report No. AMES-NSF TR-77-5, University of California, San Diego, 1977.
11. Hegemier, G. A., G. Krishnamoorthy, R. O. Nunn, and T. V. Moorthy, "Prism Tests for the Compressive Strength of Concrete Masonry," Report No. AMES-NSF TR-77-1, University of California, San Diego, 1977.
12. Nachbar, W. and R. Furgerson, "Friction Law for Grouted Concrete Blocks Following Interface Shear Failure," Report No. AMES-NSF-TR-75-4, University of California, San Diego, 1975.